University of New Hampshire
University of New Hampshire Scholars' Repository

Doctoral Dissertations | Student Scholarship

Winter 2008

Investigation and characterization of size effects in microforming processes

Sunal Ahmet Parasiz
University of New Hampshire, Durham

Follow this and additional works at: https://scholars.unh.edu/dissertation

Recommended Citation
Parasiz, Sunal Ahmet, "Investigation and characterization of size effects in microforming processes" (2008). *Doctoral Dissertations*. 460.
https://scholars.unh.edu/dissertation/460

This Dissertation is brought to you for free and open access by the Student Scholarship at University of New Hampshire Scholars' Repository. It has been accepted for inclusion in Doctoral Dissertations by an authorized administrator of University of New Hampshire Scholars' Repository. For more information, please contact nicole.hentz@unh.edu.

NOTE TO USERS

Page(s) not included in the original manuscript and are unavailable from the author or university. The manuscript was scanned as received.

107

This reproduction is the best copy available.

UMI®

INVESTIGATION AND CHARACTERIZATION OF SIZE EFFECTS IN MICROFORMING PROCESSES

BY

SUNAL AHMET PARASIZ

B.Sc., Istanbul Technical University, 1998

M.Sc., Istanbul Technical University, 2002

DISSERTATION

Submitted to the University of New Hampshire

In Partial Fulfillment of

The Requirements for the Degree of

Doctor of Philosophy

In

Mechanical Engineering

December 2008

UMI Number: 3348316

INFORMATION TO USERS

The quality of this reproduction is dependent upon the quality of the copy submitted. Broken or indistinct print, colored or poor quality illustrations and photographs, print bleed-through, substandard margins, and improper alignment can adversely affect reproduction.

In the unlikely event that the author did not send a complete manuscript and there are missing pages, these will be noted. Also, if unauthorized copyright material had to be removed, a note will indicate the deletion.

UMI®

UMI Microform 3348316
Copyright 2009 by ProQuest LLC.
All rights reserved. This microform edition is protected against unauthorized copying under Title 17, United States Code.

ProQuest LLC
789 E. Eisenhower Parkway
PO Box 1346
Ann Arbor, MI 48106-1346

This dissertation has been examined and approved.

Dissertation Director, Brad L. Kinsey, Associate Professor of Mechanical Engineering

Todd Gross, Professor of Mechanical Engineering

James Krzanowski, Professor of Mechanical Engineering

Igor Tsukrov, Associate Professor of Mechanical Engineering

Jian Cao, Associate Professor of Northwestern University

11/24/2008

Date

DEDICATION

This dissertation is dedicated to my parents, M. İlker Parasız and Süheyla Parasız who have always dedicated their lives to me and to my sister H. Tolga Parasız. Also, this dissertation is dedicated to my wife Canan Gamze Güleryüz who always supports me.

ACKNOWLEDGEMENT

I would like to thank Prof. Brad Kinsey for sharing his knowledge with me and for his tireless guidance, careful and attentive supervision and continuous support as my advisor. I had a lot of fun working in his project. I would also like to thank to our collaborators at Nortwestern University; Prof. Jian Cao and her graduate students, Neil Krishnan and Numpon Mahayotsanun who have provided the mixroextruded specimens that were used in Chapter I.

Prof. Todd Gross, Prof. James Krzanowski and Prof. Igor Tskurov are gratefully acknowledged. Through my Ph.D. studies they extended the borders of my knowledge in mechanical engineering and materials science. The knowledge I gained here at the University of New Hampshire not only helped me a lot in my current research but also I am sure will help my future studies. Also, Prof. Barbaros Celikkol who encouraged me to apply University of New Hampshire for Ph.D. is gratefully acknowledged.

Next I would like to thank to my colleagues in the Manufacturing Lab. I would like to thank Reid VanBensthysen for his diligent and accurate work. Without his help I would not have finished the research in chapter 2 in a short period of time. Also, Mike Siopis, Danielle Grau are greatly appreciated for their help. Finally, the support from Graduate School of University New Hampshire for the 2007-08 academic year Dissertation Fellowship and the support from the National Science Foundation for this research under DMI 0400267 is gratefully acknowledged.

TABLE OF CONTENTS

DEDICATION.....iii

ACKNOWLEDGEMENT.....iv

LIST OF TABLES.....viii

LIST OF FIGURES.....ix

ABSTRACT.....xiii

INTRODUCTION.....1

CHAPTER 1 MICROEXTRUSION.....16

Background.....16

Experimental Setup for Microextrusion.....19

Microextrusion Results.....21

Final Shape and Microstructure Evaluations.....21

Microhardness Evaluations.....27

The Effect of Surface Grains on Deformation Distribution through the Radial Direction.....36

X-Ray Pole Figure Texture Analyses.....38

Conclusion of This Chapter.....50

CHAPTER 2 MICROBENDING.....52

Background.....52

Experimental Procedure.....55

Results.....58

Discussion.....70

Conclusion of This Chapter.....74

CHAPTER 3 MICROTENSILE TESTS.....76

Background.....76

Results.....76

Conclusion of This Chapter.....79

CHAPTER 4 INVESTIGATION OF STRAIN GRADIENT HARDENING.....80

Background.....80

Analytical Model.....83

Strain Distribution Through the Diameter of an Extruded Workpiece.....83

Calculation of Density of GNDs During Microextrusion.....89

Strain Gradient Hardening During Microextrusion.....91

Conclusion of This Chapter.....97

CHAPTER 5 CONCLUSIONS.....99

CHAPTER 6 FUTURE WORK.....103

LIST OF REFERENCES.....105

APPENDICES.....110

APPENDIX A 111

X-Ray Pole Figure Analyses: 111

APPENDIX B.....113

MatLab code for the Microbending hardness contour plots:.....113

MatLab Code for the Microbending average hardness increase curves:.....120

MatLab Code for the Microbending average hardness increase curves for same grain size, Figure 2.9.....125

MatLab Code for the Normalized peak bending force versus specimen size curves for 20 μm, 190 μm and 280 μm grained sheets, Figure 2.11.....142

LIST OF TABLES

Table 1.1 Summary of two studies on texture gradients in rolling and extrusion of Al 1100.....41

Table 2.1 Heat treatment temperatures and the obtained grain sizes.....56

Table 2.2 The initial hardness of the sheets prior to micobending.....57

Table 4.1 The increase in strength and hardness at the axis of symmetry due to SGH for the pins from previous study.....95

LIST OF FIGURES

Figure 1 Examples of microformed metal parts [1].....1

Figure 2 Shape irregularity after a microscale backwards can extrusion [3].....2

Figure 3 As dimensions decrease, the surface to volume ratio increases.....3

Figure 4 Tensile tests of aluminum sheets which have constant grain size and various sheet thicknesses [9].....4

Figure 5 Strain gradient hardening in microtorsion of thin copper wires [15].....6

Figure 6 Plastic bending of a crystal of length l and thickness t to a radius of curvature r [25]. Shown are a) the dimensions before plastic bending and b) the dimensions after plastic bending. This plastic bending geometry can be achieved by introducing N number of edge dislocations (GNDs) which have Burgers vectors parallel to neutral axis as shown in c) [25].....7

Figure 7 The GNDs that are assumed to be stored to accommodate the plastic bending geometry.....8

Figure 8 When a single active slip plane intersects a non-deformable particle a), the array of shear loops b), and prismatic dislocation loops c), d), that produce the desired displacement are shown.. Note that interstitial and vacancy prismatic loops are indicated with (I) and (V) respectfully [26].....11

Figure 9 a) Schematic of tensile plastic deformation of a polycrystal which have an average grain size of d. b) If the deformation of the grains are not constrained by the neighboring grains, voids and overlaps between the grains occur. c,d) The voids and overlaps can be corrected by GNDs.....12

Figure 1.1 Experimentally observed flow pattern of macroscale extruded lead [29].....17

Figure 1.2 Schematic representation of deformation modes during extrusion on a half longitudinal cross-section: a) Pure elongation is more pronounced in the center since the shear deformation is less and b) the additional shear deformation increases gradually from central region to the outer edge.....17

Figure 1.3 Microextrusion set-up (a) segmented dies (b) forming assembly (c) loading stage and (d) force-displacement response.....19

Figure 1.4 The smallest size microextrusion die fabricated using micro-EDM.....20

Figure 1.5 Microstructure of brass samples after heat treatment (a) 550°C for 1 hour (32 μm grain size) (b) 700°C for 1 hour (211 μm grain size).....21

Figure 1.6 Samples of pins extruded using the Ø0.76:0.57 mm die and workpieces having a grain size of 32 μm or 211 μm.....22

Figure 1.7 Microstructure photos of a smallest size, Ø0.76/.57 mm, coarse grained curved pin.....23

Figure 1.8 Microstructure photos of additional smallest size, Ø0.76/.57 mm, coarse grained curved pins.....24

Figure 1.9 Microstructure of Ø0.76/.57 mm 32 μm grained pins at a) reduction and b) straight portion of the pin after reduction.....26

Figure 1.10 Microstructure of Ø0.76/.57 mm, 211 μm grain size pins at a) reduction and b) straight portion of the pin after reduction.....26

Figure 1.11 Correlation between the hardness of cold rolled CuZn30 and the strain (data obtained from [39]).....27

Figure 1.12 A photograph of a fine grained Ø1.5/1.0 mm pin after the microhardness evaluation.....28

Figure 1.13 Schematic of indentation geometry for a Knoop indenter.....29

Figure 1.14 Hardness values in the reduction area for a 32 μm grain size pin. Zero radial location corresponds to axis of symmetry of the pin.....30

Figure 1.15 Average hardness distribution in the undeformed fine and coarse grained billet material.....31

Figure 1.16 The average hardness profile of the fine and the coarse grained pins which have a) Ø2.0/1.33mm, b) Ø1.5/1.0mm and c) Ø0.76/0.57mm dimensions. Radial distances are from the axis of symmetry (from zero) to the outer surface.....32

Figure 1.17 The average hardness versus normalized radial distance for all microextrusion sizes for the a) coarse grained structure and b) fine grained structure.....36

Figure 1.18 Schematic of the X-Ray texture analyses.....38

Figure 1.19 a) Perfect [30] and b) imperfect [100] fiber texture for a (111) pole figure and c) two possible mirror planes for deformation in extrusion.....39

Figure 1.20 Pole figures for a fine grained a) undeformed billet Ø0.76 mm and b) a pin after extrusion, Ø0.76/0.57 mm. (S.A.: symmetry axis; E.D.: extrusion direction).....43

Figure 1.21 Pole figures of a coarse grained a) undeformed billet, Ø0.76 mm and b) straight section of a curved pin, Ø0.76/0.57 mm.....44

Figure 1.22 Pole figures of a largest size, Ø2.0/.1.33 mm, coarse grained pin which is obtained on a longitudinal cross-section just after the reduction.....45

Figure 1.23 Schematic of the orientation of a single crystal slip plane a) prior to deformation, b) after deformation without grip constraint, and c) after deformation with grip constraint (note that $\chi_i < \chi_o$) [49].....46

Figure 1.24 Schematic of the a) rotation of two grains during uniaxial deformation and b) corresponding <100> pole figure for these grains.....47

Figure 1.25 Pole figures obtained from the curved region of a coarse grained pin.....49

Figure 1.26 Pole figures obtained on the longitudinal cross-section of the coarse grained straight pin (not curved) a) from an area just after the reduction section b) from another area.....50

Figure 2.1 Variations of peak bending force and force at yield point for bending experiments (specimen thickness 1 mm).....53

Figure 2.2 Schematic of microbending tooling.....55

Figure 2.3 Microhardness measurements through the thickness on one arm of a 205 μm coarse grained 0.5 mm specimen.....58

Figure 2.4 Average contour plots of increase in the hardness after microbending operations on one arm of the 0.5 mm thick a) 20 μm fine grained b) 130 μm coarse grained c) 190 μm coarse grained sheets. 60

Figure 2.5 Average contour plots of increase in the hardness after microbending operations on one arm of the 0.5 mm thick a) 22.5 μm fine grained b) 205 μm coarse grained c) 285 μm coarse grained sheets.....61

Figure 2.6 Average hardness contour plots on one arm of the 1.5 mm thick a) 19 μm fine grained b) 175 μm coarse grained c) 280 μm coarse grained d) 660 μm coarse grained sheets.....62

Figure 2.7 Microstructure of a 0.5 mm thick, 285 μm coarse grained microbent specimen.....63

Figure 2.8 Average hardness profile at the bend area through the thickness of a) 1.625 mm b) 0.5 mm c) 0.25 mm sheets. Note: initial hardness values were subtracted from measured hardness values after bending.....65

Figure 2.9 The average hardness distribution at the bend area through the thickness of a) 20 μm b) 190 μm c) 280 μm grained sheets. Note: initial hardness values were subtracted from measured hardness values after bending.....68

Figure 2.10 Normalized bending force versus displacement curves for a) 20 μm and b) 190 μm c) 280 μm grain sized sheets.....73

Figure 2.11 Normalized peak bending force versus specimen size curves for 20 μm, 190 μm and 280 μm grained sheets.....74

Figure 3.1 Hardness distribution along the gage length of the tensile specimens.....77

Figure 3.2 Tensile test curves of 32 μm and 211 μm grain size specimens.....78

Figure 3.3 Half cross section of tensile specimen pieces a) 211 μm grain size b)32 μm grain size.....79

Figure 4.1 Dependence of strength on specimen size in microbending of thin Nickel films [23].....81

Figure 4.2 Flow chart of the calculation of predicted GND density that is stored during microextrusion.....82

Figure 4.3 Assumed material flow during extrusion.....83

Figure 4.4 Predicted strain distribution through the normalized diameter of the larger size Ø1.5/1.0 mm and Ø2.0/1.33 mm pins which have an extrusion ratio R=2.25 and submillimeter size Ø0.76/0.57 mm pins which have R=1.77.....86

Figure 4.5 Correlation between the hardness of cold rolled CuZn30 and strain (data taken from [39])....87

Figure 4.6 Measured average hardness values versus normalized radial distance for extrusion ratios of 2.25 and 1.177....88

Figure 4.7 a) Geometrically Necessary Dislocations, GNDs, which are stored during deformation at the reduction section b) a GND loop at the reduction section....90

Figure 4.8 Correlation between yield strength of rolled CuZn30 and square root of dislocation density [31]....92

Figure 4.9 Variation of ρ_{SSD} from experimental data for single crystals (inferred from stress-strain curves for polycrystals) and ρ_{GND} (calculated) with respect to shear strain [21]....92

Figure 4.10 The densities of SSDs and GNDs versus initial radius of the workpieces (for a die angle of 30° and reduction ratios of a) R=1.77 (strain of 57 %) and b) R=2.25 (strain of 81%). Note that the SSD densities correspond to the deformation amount at the axis of symmetry. The range of SSDs densities of polycrystals, which are obtained from Fig. 4.9, are presented as a shaded band....93

Figure 4.11 Percentage increase in the strength of the workpiece near the axis of symmetry due to SGH with respect to the specimen thickness for CuZn30 and $\alpha = 30°$....94

Figure 4.12 Flowchart of the strain gradient hardening calculations....95

Figure 4.13 Correlation between the hardness of cold rolled CuZn30 and the yield strength at strains levels above ε=0.35 (data obtained from [14])....97

Figure A1 Determination of preferred orientation from a pole figure....112

ABSTRACT

INVESTIGATION AND CHARACTERIZATION OF SIZE EFFECTS IN MICROFORMING PROCESSES

by

Sunal Ahmet Parasız

University of New Hampshire, December 2008

The products of miniaturization, such as mobile phones, personal digital assistants, computers and other electronic devices have become an indispensable part of our daily lives. Nowadays, more and more industrial products including some medical and electro-mechanical products contain micro scale metal parts such as connector pins, resistor caps, screws, contact springs and chip lead frames. Miniaturization brings the challenge of realizing the production of these microscale metals parts. Microforming, due to its well known advantages of high production rates, excellent material utilization, and low costs, is a promising manufacturing method compared to the alternative processes in this field. However, well-established conventional, macroscale metal forming processes can not simply be miniaturized without considering possible size effects.

The goal of this research was to determine if deformation size effects occur with miniaturization. Both deformation size effects with respect to specimen size and grain size were considered through the investigation of two processes, microextrusion and microbending. In both of these forming processes, deformation gradients are generated through the cross-sections of the specimens. To analyze these deformation size effects,

the distribution of the deformation was characterized by micohardness evaluations. In addition for microextrusion, X-Ray pole figure analyses and microstructure analyses were also performed.

For both processes, the deformation distribution through the cross sections of the fine grained specimens is not affected significantly by the specimen size (i.e. deformation distribution is independent from the specimen size) since the hardness profiles for the all specimen sizes are similar. However, as the specimen size is miniaturized, the deformation distribution of the coarse grained specimens deviates from the fine grained ones, and from the larger size specimens. In addition, as the specimen size decreases the coarse grained specimens have higher hardness increase values at the central region compared to fine grained specimens. This occurs due to the penetration of deformation from highly strained outer regions to the less strained inner regions (or expansion of the highly deformed regions).

INTRODUCTION

The current trend towards miniaturization of systems and devices brings the challenge of fabricating microscale parts in a reliable, cost effective, and environmentally friendly manner at high production rates. From this perspective, microforming, which is metal forming at the microscale, is a promising method due to its well known advantages, such as high throughput, near net shape capabilities, and excellent material utilization. In Fig. 1, examples of microformed parts are given [1].

However, well-established conventional, macroscale metal forming processes can not simply be miniaturized without considering possible size effects [1,2]. The term size effect refers to changes in material properties, frictional effects, etc. that occur with miniaturization and are associated with the material, process, tooling and/or machines used [3]. In this thesis, deformation size effects during microextrusion and microbending with respect to grain and specimen size are investigated.

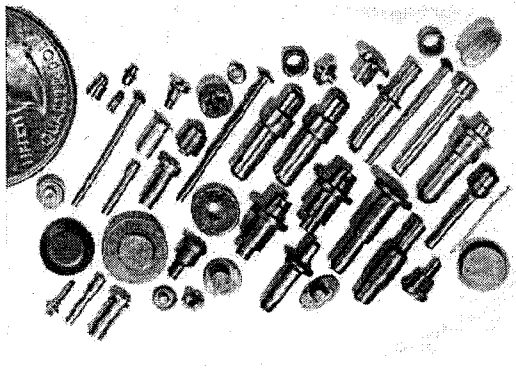

Figure 1 Examples of microformed metal parts [1].

With miniaturization, the product and process dimensions are scaled down; however, the dimensions related to the microstructure of the material such as grain size remain constant. In a macroscale specimen, numerous grains exist through the cross-section. Although the individual grains have anisotropic mechanical properties, the polycrystalline material behaves as a homogeneous continuum. However, at the microscale, when the specimen feature size approaches the grain size, the properties of individual grains cause inhomogeneous elastic and plastic deformations to occur. In microforming, the result is inconsistency and scattering in the process parameters, such as process force [4-8] and irregularities in the final shape of the products [3,8]. In Fig. 2, a shape irregularity after a microscale backwards can extrusion is shown [3]. The wall thickness of the workpiece is only 8 μm and the grains are relatively coarse, approximately 200 μm. As a result, the shape irregularity occurs.

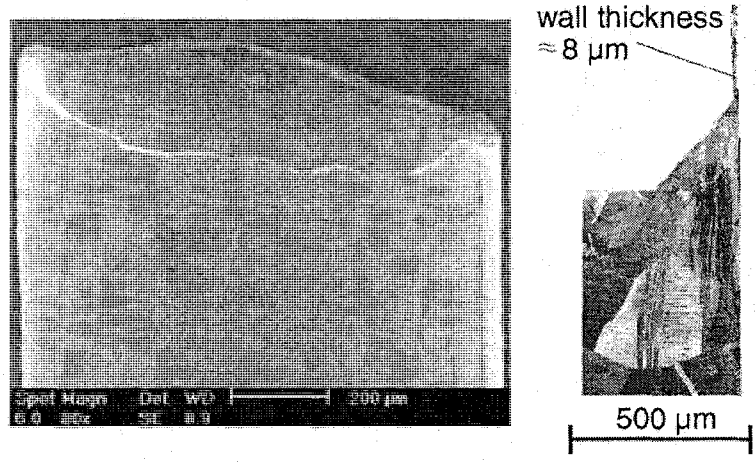

Figure 2 Shape irregularity after a microscale backwards can extrusion [3].

Another aspect of miniaturization is the increased importance of the surface region. At the microscale, as the dimensions decrease, the surface to volume ratio increases significantly. Thus, surface related phenomenon such as the effect of surface

grains on strength of material and friction become more important. See Fig. 3 for a schematic of increased importance of surface with miniaturization.

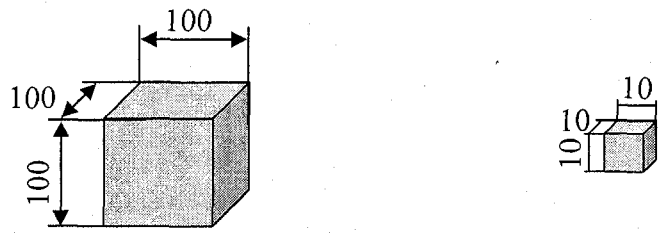

$$\frac{6\text{x}100\text{x}100}{100\text{x}100\text{x}100} = \frac{6}{100}\ \text{mm}^{-1} \qquad \frac{6\text{x}10\text{x}10}{10\text{x}10\text{x}10} = \frac{6}{10}\ \text{mm}^{-1}$$

Figure 3 As dimensions decrease, the surface to volume ratio increases.

As specimen dimensions are scaled down the share of the surface grains in the total volume increases. Less constrained surface grains deform more easily than interior grains. Thus, in general a decrease in the specimen size, results in a decrease in the overall strength of the material [1-4, 6]. In Fig. 4, the effect of sheet thickness on the strength of the sheet material is given [9]. The grain size is constant and as the sheet thickness decreases the share of surface grains in the total volume of the material increases. As a result, the strength of the sheet material decreases. In addition, as the sheet thickness decreases an increase in the scattering of the strength is observed due to the sometimes favorable, sometimes unfavorable orientation of individual grains with respect to the deformation. The decrease in the strength of the material with miniaturization due to the effect of surface grains leads to lower process forces relative to the process dimensions (when the deformed area has free surfaces like in the air bending process) [2, 4, 6-8,10]. Another general size effect that occurs with miniaturization is the decrease of uniform and necking elongation in tensile tests [2, 3].

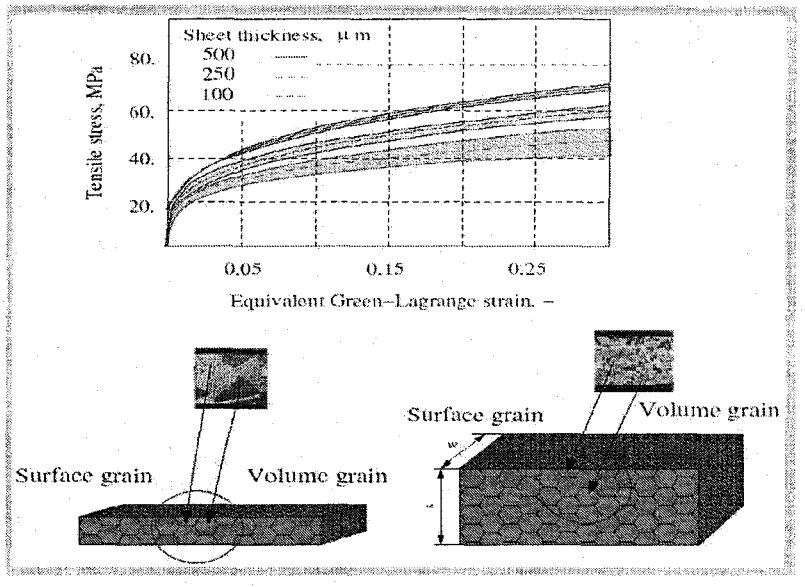

Figure 4 Tensile tests of aluminum sheets which have constant grain size and various sheet thicknesses [9].

The effect of miniaturization on friction has also been investigated. It has been shown that friction increases significantly with miniaturization in the case of lubrication with oil [2, 3, 11-14]. This frictional behavior was explained by the model of open and close, i.e. dynamic and static lubricant pockets. During forming, the lubricants become trapped between the deformed asperities (closed lubricant pockets). However, with miniaturization, the ratio of open to closed lubricant pockets increases, which allows more lubricant to escape and produces to a flatter surface and higher friction [2, 3, 11-14]. The same research group found that friction is size-independent when no lubrication is used [11].

Krishnan et al. [15] investigated the effect of miniaturization using forward microextrusion process for a no lubrication condition. Their results indicate that the friction coefficient for geometrically similar pins is constant until the extruded diameter is less than 1 mm, after which the friction coefficient decreases.

Another size effect which has been investigated is process model size effects, i.e., variations required to process models to accurately capture manufacturing parameters such as force. Onyancha et al. [16] investigated variations in the force during microextrusion. In order to more accurately predict the force values, an increased shear deformation term was incorporated into a well established macroscale process model. Similarly, for microbending [17-19], process model assumptions were modified in order to accurately predict the bending force in the process.

As mentioned previously, with miniaturization the number of grains in the forming volume decreases significantly. This results in more inhomogeneous deformation which decreases the formability and accuracy of the final geometry of the parts. To solve this problem warm forming of microparts has been investigated [5, 20]. It was shown that warm microforming improves material flow, produces a more homogenized hardness distribution, and reduces scatter in process parameters.

Additionally, in some deformation processes at the microscale, such as bending and torsion, a significant miniaturization causes steep strain gradients to exist and the generation of additional geometrically necessary dislocations, GNDs. As a result, the workpieces experience strain gradient hardening and the deformation forces increase significantly [22,23]. Strain gradient hardening of wires subjected to torsional loading and microbent thin sheets, which have diameters and thicknesses less than 100 μm, has been reported [21,23,24]. Fig. 5 shows that the shear strength in microtorsion of thin copper wires increases by a factor of 3 as the wire diameter decreases from 170 μm to 12 μm [21].

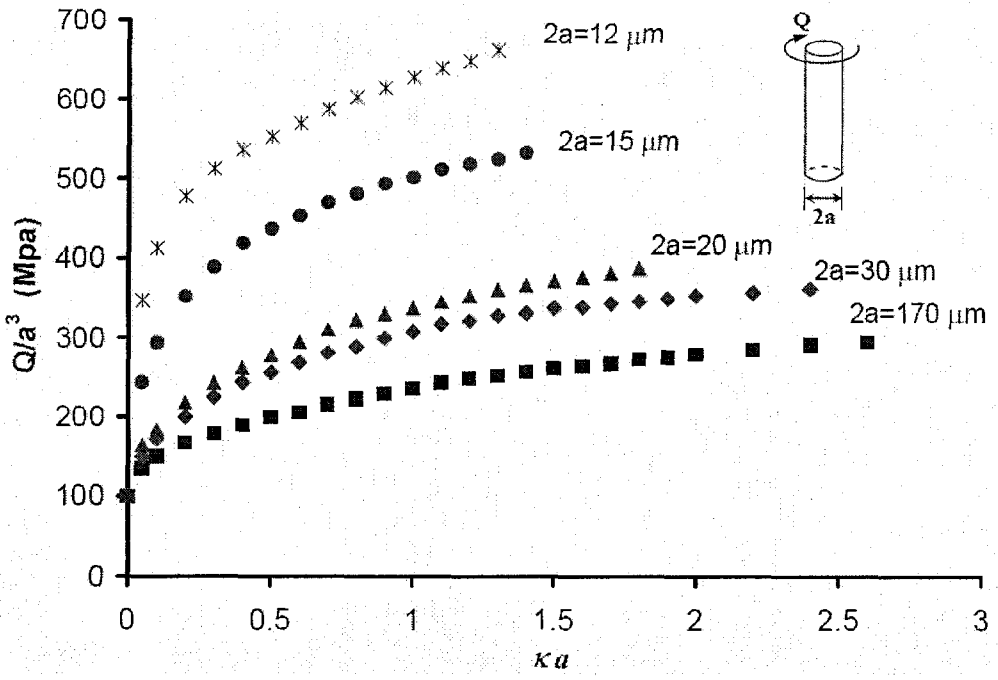

Figure 5 Strain gradient hardening in microtorsion of thin copper wires [15].

When a crystal is deformed so that steep plastic strain gradients are present within it, the material work hardens more than if such gradients were not present [25]. In his pioneering paper in 1970 on inhomogeneous deformation, Ashby introduced the distinction between statistically stored dislocations, SSDs, and geometrically necessary dislocations, GNDs [26]. The density of SSDs is associated with the amount of plastic strain whereas the density of GNDs is directly proportional to the gradients of plastic strain. During deformation, crystals work harden because dislocation motion is impeded and thus dislocations are stored during straining. The dislocations that are stored by impeding one another in a random fashion during deformation are called SSDs. In addition, for certain deformation geometries, plastic strain gradients are generated within the crystals. In such cases, some dislocations are required to be stored within the crystals to ensure the compatibility of deformation of various parts of the crystals. These

dislocations are called GNDs. Void formation or material transport by means of diffusion are not allowed. It is also assumed that long range stresses in the crystal do not exist or are smaller than the local yield strength [27]. Under such conditions, the number or density of GNDs required for a compatible deformation can be obtained by means of simple geometric reasoning. An example is a plastic bending of a crystal. As shown in Fig. 6 for bending a crystal to a radius of curvature r, the upper portion of the crystal experiences tensile deformation, i.e., its length is increased from l ($r\theta$) to $l+\delta l$ ($(r+t/2)\theta$) where θ is the bend angle, l is the initial length of the crystal, δl is the extension at the upper surface and t is the thickness of the crystal. Conversely, the inner surface experiences compression with a negative length change of $t\theta/2$.

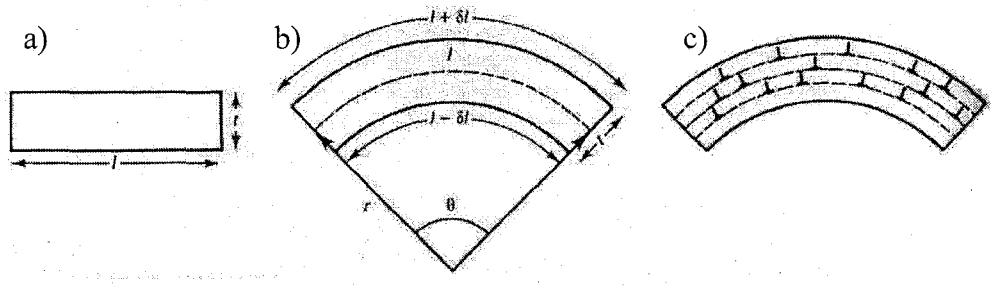

Figure 6 Plastic bending of a crystal of length l and thickness t to a radius of curvature r [25]. Shown are a) the dimensions before plastic bending and b) the dimensions after plastic bending. This plastic bending geometry can be achieved by introducing N number of edge dislocations (GNDs) which have Burgers vectors parallel to neutral axis as shown in c) [25].

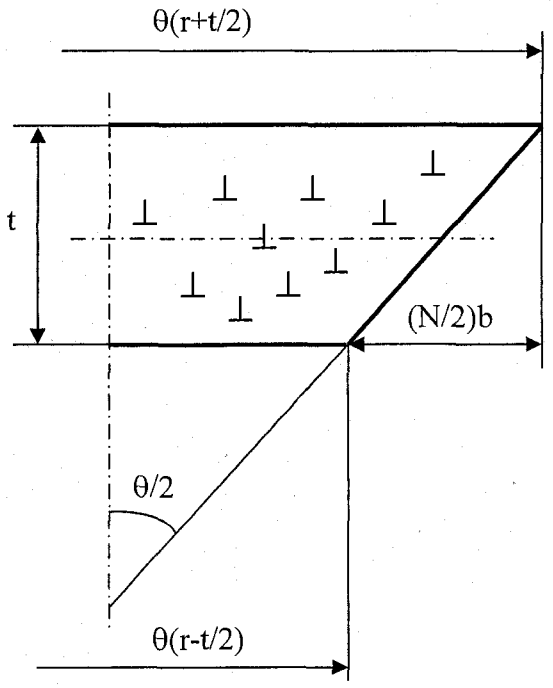

Figure 7 The GNDs that are assumed to be stored to accommodate the plastic bending geometry

In order to accommodate the bent geometry and plastic strain gradients through the thickness, N number of GNDs should be stored in the crystal. The GNDs are assumed to be edge dislocations which have Burgers vectors parallel to the neutral axis as shown schematically in Fig. 6c and Fig. 7. The number of GNDs is:

$$N = \frac{\theta t}{b} \tag{1}$$

Since;

$$Nb = (l + \delta l) - (l - \delta l) = \theta(r + \frac{t}{2}) - \theta(r - \frac{t}{2}) \tag{2}$$

The density of GNDs that are stored during bending can be calculated by dividing the GND number, N by the area:

$$\rho_{GND} = \frac{N}{Area} \tag{3}$$

The area of the crystal is:

$$Area = \theta rt \tag{4}$$

Thus, the density of GNDs that is stored during plastic bending of a crystal is:

$$\rho_{GND} = \frac{1}{rb} \tag{5}$$

which is basically the curvature of the bend divided by the Burgers vector of the GNDs.

The density of GND, ρ_{GND}, is directly related to the plastic shear strain gradients, $\chi = d\gamma_{pl}/dy$. In the simplest one dimensional case for single slip with a Burgers vector b in the y-direction [57]:

$$\rho_{GND} = \frac{1}{b}\left(\frac{d\gamma_{pl}}{dy}\right) = \frac{\chi}{b} \tag{6}$$

Thus, the density of the GNDs that are generated during plastic bending of the crystal can be calculated according to strain gradients that exist through the thickness. As mentioned previously for bending a crystal to a radius of curvature r (see Fig. 6), the upper surface of the crystal stretches and its length is increased from l (=rθ) to l+δl (=(r+t/2)θ) and the inner surface experiences compression with a negative length change of tθ/2. Thus, a strain gradient accompanies the plastic bending and the magnitude of the strain gradient is the strain difference between the two surfaces (2δl/l) divided by the thickness (t) over which the gradient exists [25], i.e.:

$$\chi = 2\frac{\delta l}{lt} = \frac{\theta}{l} = \frac{1}{r} \tag{7}$$

where χ is the strain gradient. Then according to Eq. (6) the density of the GNDs that is

stored during plastic bending of a crystal is;

$$\rho_{GND} = \frac{\chi}{b} = \frac{1}{rb} \tag{8}$$

which is the same result as Eq. (5).

It should be noted that plastic bending introduces both SSDs and GNDs in a crystal. The density of GNDs will rarely dominate the total dislocation density unless the radius of the curvature is very small to generate steep strain gradients (on the order of tens of micron). For crystals containing small non-deformable particles and inclusions, during deformation severe strain gradients are generated within the vicinity of the particles. As a result, a significant number of GNDs are stored during deformation at the vicinity of the particles, and the crystal experiences strain gradient hardening.

For crystals containing non-deformable particles, deformation becomes inhomogeneous even if the crystal deforms in a uniform fashion, such as simple tension. No plastic deformation (slip) occurs within the particles or within the adjacent layer of the matrix, provided this layer is strongly bonded to the particle. However, far from the particle, the plastic deformation (slip) can be as large as the imposed deformation. Thus, even the total crystal is forced to deform in a uniform fashion, plastic strain gradients are generated within the vicinity of the particles. To ensure the compatibility of deformation, i.e., to accommodate the strain gradients, GND arrays are stored at the vicinity of the particles. This accommodation can be provided by arrays of prismatic loops (as interstitial and vacancy prismatic loops, see Fig. 8b) as well as by shear loops (see Fig. 8c). These GND arrays are shown schematically in Fig. 8. In actuality, during deformation as a result of cross slip, the GND arrays associated with dislocation bowing changes from shear to prismatic loops with increasing strain. This transition occurs at

shear strains on the order of 1%. At higher strains, prismatic dislocation arrays are promoted. Ashby [26] has shown that the density of GNDs that is stored during deformation of a crystal which contains equiaxed particles is:

$$\rho_{GND} = \frac{8f\gamma}{bd} \tag{9}$$

where f is the volume fraction of the particles, γ is the shear strain, b is the Burgers vector and d is the dimension of the particles.

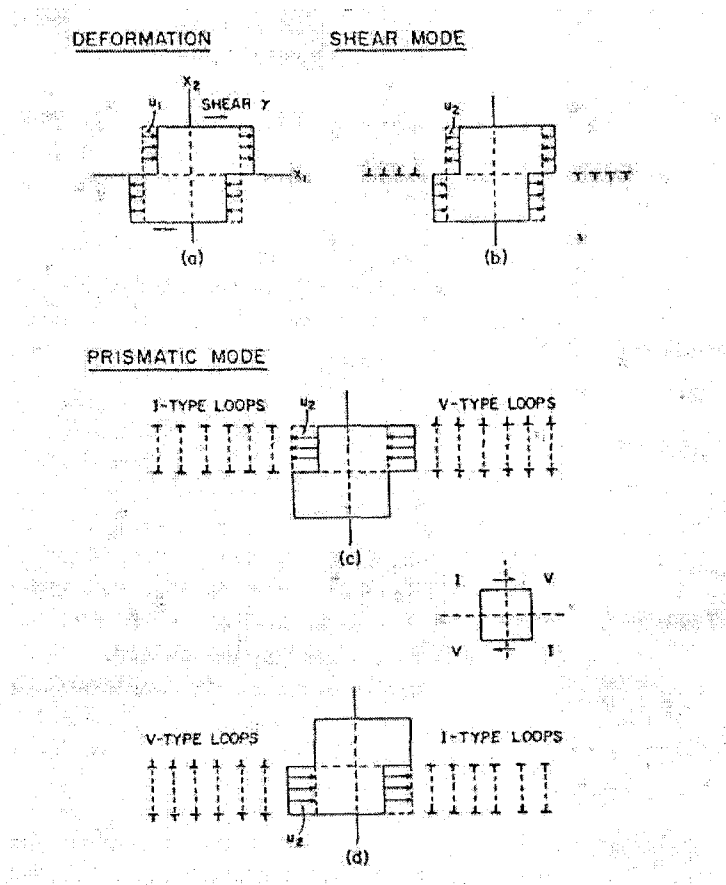

Figure 8 When a single active slip plane intersects a non-deformable particle a), the array of shear loops b), and prismatic dislocation loops c), d), that produce the desired displacement are shown.. Note that interstitial and vacancy prismatic loops are indicated with (I) and (V) respectfully [26].

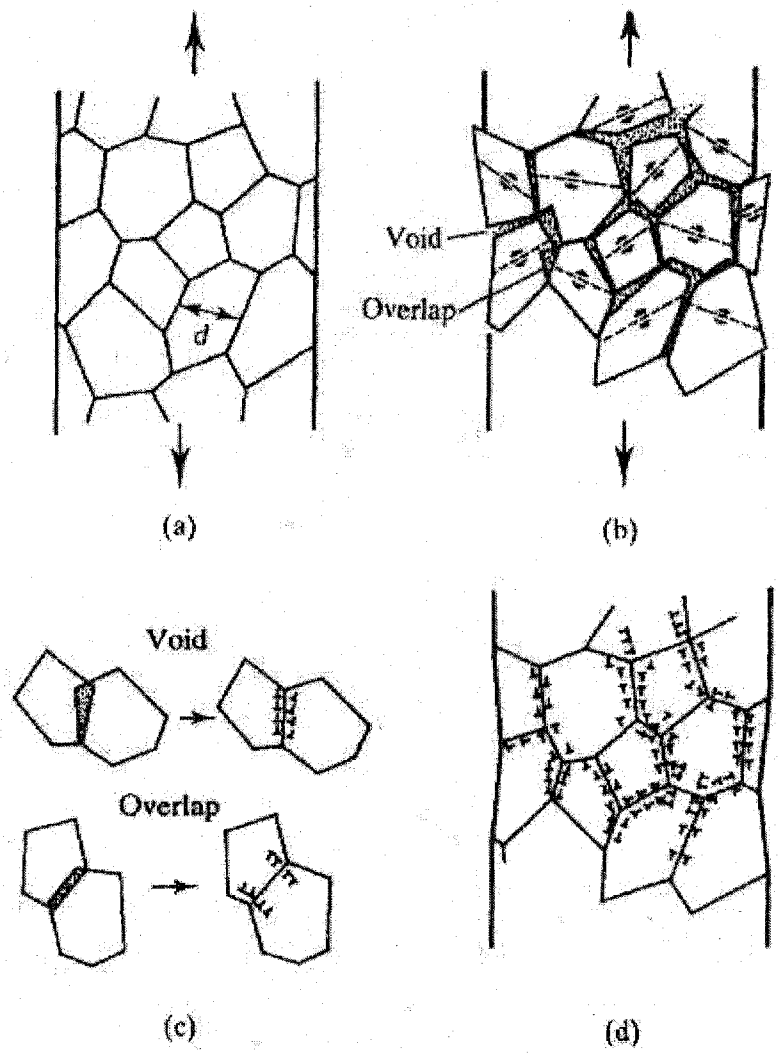

Figure 9 a) Schematic of tensile plastic deformation of a polycrystal which have an average grain size of d. b) If the deformation of the grains are not constrained by the neighboring grains, voids and overlaps between the grains occur. c,d) The voids and overlaps can be corrected by GNDs [26]

In addition, deformation of, polycrystals is inhomogeneous as well. During deformation, strain gradients are produced especially at the vicinity of the grain boundaries. Each grain in a polycrystal tends to deform differently depending on its orientation and constraints imposed by the neighboring grains. To ensure compatibility

i.e., to avoid voids and overlaps between the neighboring grains, arrays of GNDs are stored at the vicinity of the grain boundaries as shown in Fig. 9. Although the GND arrangements are different across each boundary, the GND density can be estimated by considering the average grain size. The amount of overlap (or void displacement) between the adjacent grains is proportional to εd, where ε is the average strain and d is the average grain diameter. Dividing this product by the Burgers vector provides the number of GNDs and further division by grain area ($\sim d^2$) gives the density of GNDs.

$$\rho_{GND} \approx \frac{\varepsilon}{bd} = \frac{\varepsilon}{4bd} \tag{10}$$

where the factor 4 arises from geometrical considerations.

GNDs contribute to the strain hardening of materials, and according to Ashby, a Taylor-type relation can be used to estimate their contribution on strain hardening:

$$\tau = cGb\sqrt{\rho_{SSD} + \rho_{GND}} \tag{11}$$

where G is the shear modulus and c is a numerical factor, typically on the order of $c \approx$ 0.2-0.4 and ρ_{SSD} is the density of statistically stored dislocations.

So far in the introduction section the size effects that occur with miniaturization are summarized. The goal of this research is to determine the effect of miniaturization with respect to both specimen size and grain size on the deformation in microforming processes. The processes of interest include ones where deformation gradients exist through the cross-section of the workpiece (i.e., microextrusion and microbending) and one where no deformation gradients exist (i.e., a simple tensile test). It was expected that the deformation mode would have an effect on such size effects. These deformation size effects would be with respect to the consistency in the deformation area as well as

measure of the deformation (e.g., hardness). Potential causes for these deformation changes (e.g., penetration of deformation or strain gradient hardening) were of interest as well.

In Chapter 1 of this thesis, the deformation size effects during microextrusion are investigated via microstructure and microhardness evaluations. It is found that the deformation distribution through the diameter of the microextruded pins was affected by the specimen and the grain size. The smaller size coarse grained extruded pins have higher hardness at the central region compared to the fine grained ones which seemingly contradicts the Hall-Petch relationship. Through X-Ray pole figure analyses, it is found that penetration of shear is the cause of this behavior. Also, less consistent deformation is produced through the cross-section when few grains are present.

In Chapter 2 in a similar fashion, the effect of grain size and specimen size on the deformation distribution through the thickness in microbending is investigated via microhardness evaluations. It is found that when the grain size is fine the deformation distribution is independent of specimen size. Also, the deformation distribution is found to be independent of grain size for the largest size, 1.625 mm thick specimens. However, with miniaturization the deformation distribution through the thickness of the coarse grained specimens deviate from the fine grained specimens and 1.625 mm thick specimens. The coarse grained pins have higher hardness increase values at the central region due to penetration of deformation. Also, inconsistent deformation pattern exist with miniaturization.

In Chapter 3, deformation of microtensile tested specimens are investigated via microhardness measurements. In microextrusion and microbending, deformation

gradients are present through the cross-section of the workpiece. These deformation gradients become steeper with miniaturization and as a result the coarse grained structures have higher hardness at the central regions for the two microforming processes. However, in tensile deformation no significant gradients are present and no contradiction to the Hall-Petch effect is found. It is shown that the coarse grained specimens have lower hardness values than the fine grained ones through the cross-sections. However, inconsistent deformation exists still for the specimens with fewer grains through the cross-section.

In Chapter 4, strain gradient hardening during microextrusion is studied. From past research, it is known that strain gradient hardening becomes significant when the specimen feature size is on the order of tens of microns. To determine the amount of strain gradient hardening for the specimen sizes used in this research (which are on the order of 400 μm or more) an analytical model is established to asses strain gradient hardening of metals during axis symmetric forward microextrusion. First, a formulation is generated to estimate the strain distribution through the thickness during axis symmetric forward extrusion. By also using shear components of the formulation, a new model is established to estimate the GND density. Then, using a Taylor type equation as proposed by Ashby, the strain gradient hardening, SGH, during microextrusion is estimated.

Finally, the conclusions along with the possible future work are presented in Chapter 5.

CHAPTER 1

MICROEXTRUSION

Background

Extrusion is a plastic deformation process in which a block of metal (billet) is forced to flow by compression through a die opening with a smaller cross-sectional area than that of the original billet. In extrusion, large strains are produced in the workpiece, but these strains are inhomogeneous through the cross-section. In Fig. 1.1, an experimentally observed flow pattern during macroscale extrusion is shown [29]. Shear deformation gradients exits through the radial direction and as a result deformation increases gradually from central to surface regions. While the material near the axis of symmetry experiences pure elongation due to the compressive forces, the material near the surface undergoes additional extensive shear deformation [30]. In Fig. 1.2., these deformation modes are schematically shown. Due to the extensive shear deformation, the material in the surface regions experiences more strain hardening. The shear deformation occurs due to the redundant deformation which arises from the deformation geometry, i.e., the die geometry, and also due to the friction between the die and workpiece. Thus, the deformation gradients through the cross-section are influenced by the geometry of the process, friction, and the plastic material properties of the deforming workpiece [31].

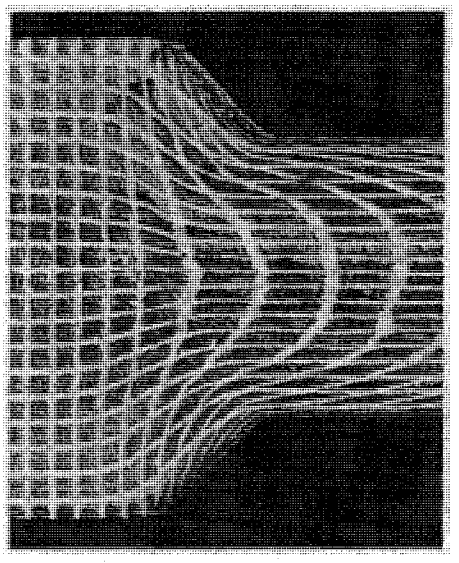

Figure 1.1 Experimentally observed flow pattern of macroscale extruded lead [29].

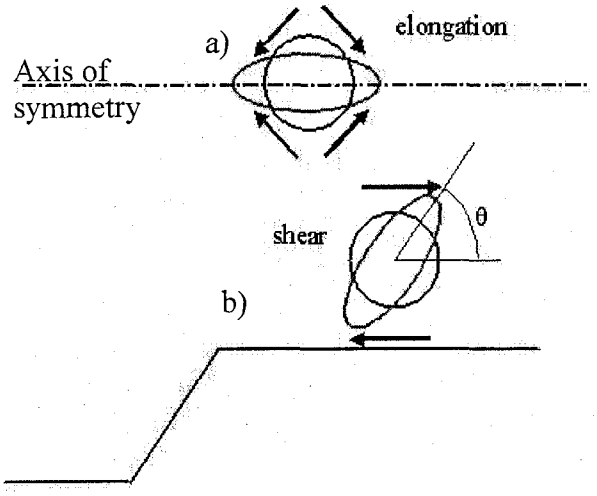

Figure 1.2 Schematic representation of deformation modes during extrusion on a half longitudinal cross-section: a) Pure elongation is more pronounced in the center since the shear deformation is less and b) the additional shear deformation increases gradually from central region to the outer edge.

Recently, microextrusion has emerged as a viable manufacturing process to fabricate metallic micropins having characteristic dimensions on the order of less than 1 mm. At this length scale, the deformation of the workpiece is dominated by so-called 'size effects', e.g., grain size and frictional behavior variations at small length scales. In

this chapter of the thesis, it will be shown that during submillimeter size forward microextrusion, Ø0.76/0.57mm diameters before and after extrusion respectively, inhomogeneous deformation occurs. This effect is caused by the properties of individual grains which dominate the overall deformation of the cross-sections when the grain size becomes comparable to the specimen feature size. As a result, coarse grained pins, which have four grains through their diameter on average, showed a tendency to curve in varying directions and magnitudes during microextrusion. However, this behavior was not observed in fine grained pins which have 24 grains through their diameter on average.

Microstructural analyses were performed on the small, fine and coarse grained pins in order to assess the deformation changes. Additionally, the effect of both specimen size and grain size on the deformation during microextrusion is investigated through microhardness evaluations, which were conducted on pins which have three different sizes and two different grain sizes. Microhardness evaluations revealed that with miniaturization the coarse grained pins begin to have higher hardness than the fine grained ones especially in the inner region of the pins, which is seemingly inconsistent with the Hall-Petch relationship. This indicates that some differences in the deformation of the coarse grained pins occur. This result along with X-ray texture and microstructure analyses demonstrate that during microextrusion, the coarse grained structures experience more shear deformation especially in the central region of the pins [32- 36].

Experimental Setup For Microextrusion

In order to perform microextrusion experiments, a novel forming assembly was fabricated at Northwestern University that consisted of an extrusion ram mounted on a yoke that slides along linear bearings [37]. The ram is guided by the linear bearings into an extrusion die that is mounted and clamped in a die block. The extrusion dies were produced as a segmented block in order to facilitate the removal of the micropins after extrusion. This forming assembly is then placed in a loading stage that is equipped with a load cell (capacity 8909N) and an LVDT to measure the extrusion force and the corresponding ram displacement respectively. The entire microextrusion setup is shown in Fig. 1.3.

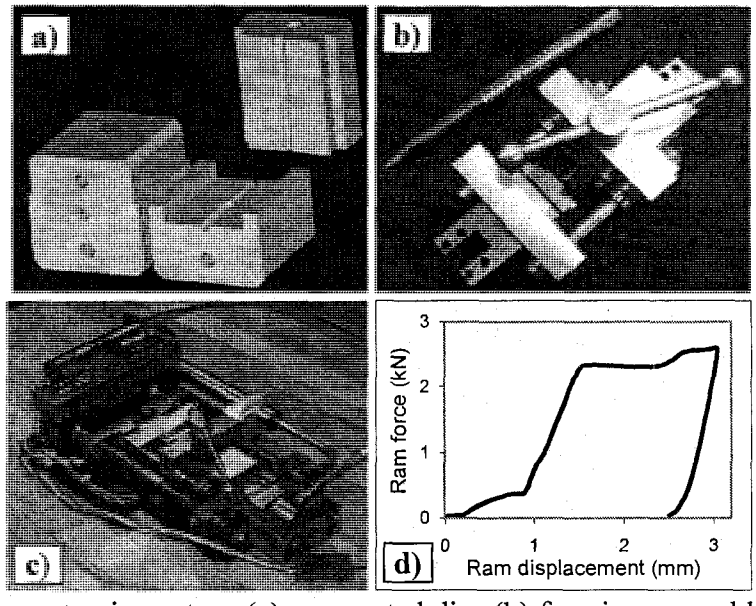

Figure 1.3 Microextrusion set-up (a) segmented dies (b) forming assembly (c) loading stage and (d) force-displacement response.

To investigate the influence of the specimen size on deformation, three different die sets which have diameters of Ø0.76/.57 mm, Ø1.5/1.0 mm and Ø2.0/1.33 mm before and after reduction respectively, were used. The dies were designed to obtain the same extrusion ratio. However, for the smallest die, a 1.77:1.0 extrusion ratio was obtained

while the larger ones have a higher extrusion ratio of 2.25:1.0. The die cavities of submillimeter size were fabricated using micro-EDM while the larger dies were fabricated by conventional drilling. All dies were polished to ensure that they had similar surface roughness values. The surface roughness of each die was measured by a Micro XAM surface-mapping microscope and all dies were found to have an average surface roughness (R_a) in the range of 0.8 to 1.0 μm. The dies were then used for microextrusion of pins. The experiments were conducted without lubrication at room temperature. The geometry of the smallest size microextrusion die can be seen in Fig. 1.4. It has a base diameter of 756 μm, an extruded diameter of 568 μm and a bearing surface length of 201μm. Details of the forming assembly with which the microextrusion experiments were performed can be found in [37].

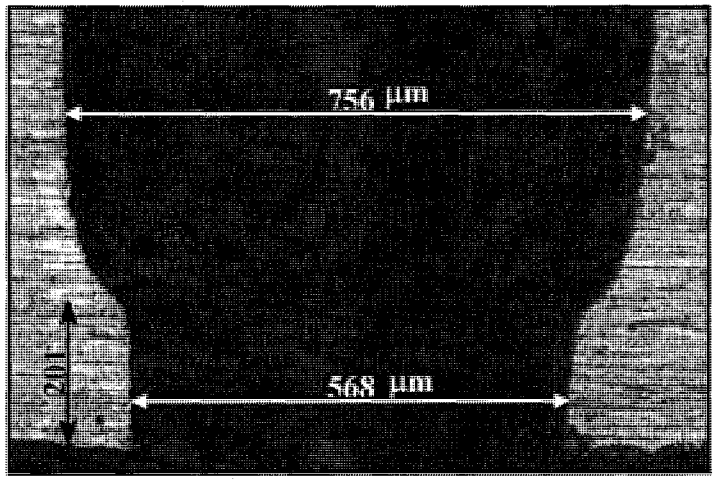

Figure 1.4 The smallest size microextrusion die fabricated using micro-EDM.

The microextruded pins were fabricated from CuZn30 α-brass which has a FCC structure. To investigate if a grain size effect on deformation exists; a fine and a coarse grained structure were used in the experiments. An average grain size of 32 μm with a minimum size of 13 μm, a maximum size of 132 μm and a standard deviation of 34 μm was obtained by heating the brass samples at 550°C for one hour and heating at 700°C

for one hour produced an average grain size of 211 μm with a minimum size of 45 μm, a maximum size of 432 μm and a standard deviation of 67 μm. The microstructures that were obtained after heat treatment were observed under an optical microscope after polishing and chemical etching and are shown in Fig. 1.5. There are approximately 3.6, 7.1 and 9.5 grains through the diameter of the coarse grained pins on average for the three die sizes, Ø0.76/.57 mm, Ø1.5/1.0 mm and Ø2.0/1.33 mm before and after reduction respectively. For the fine grained pins, there are approximately 24, 47 and 63 grains through the diameter respectively.

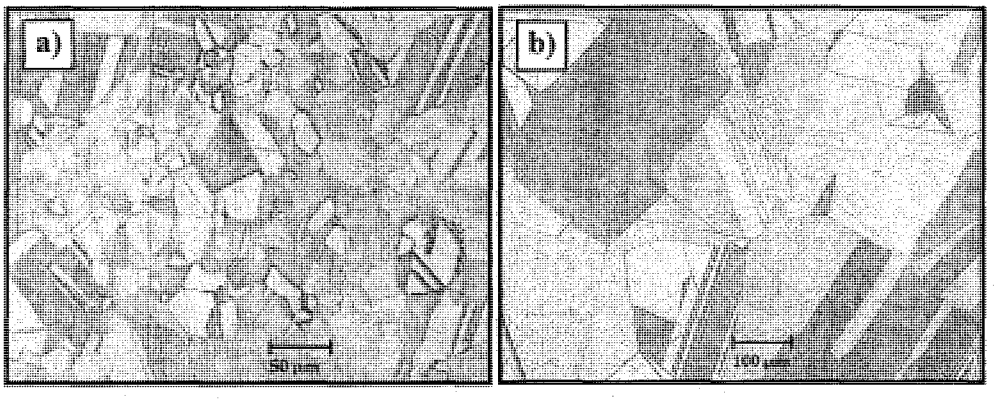

Figure 1.5 Microstructure of brass samples after heat treatment (a) 550°C for 1 hour (32 μm grain size) (b) 700°C for 1 hour (211 μm grain size).

Microextrusion Results

Final Shape and Microstructure Evaluations

Figure 1.6 shows samples of the extruded micropins obtained using workpieces of the two different grain sizes for the smallest submillimeter size microextrusion, Ø0.76/.57 mm. The pins produced using the 211μm, coarse-grained material show a tendency to curve. The trend is fairly repeatable, although the curvature occurs in different directions and in different severities, and was observed in approximately 70-80% of the specimens for this particular material. However, this behavior is not observed in pins made using the

32 μm, fined-grained material and in the larger size pins including the coarse structure ones.

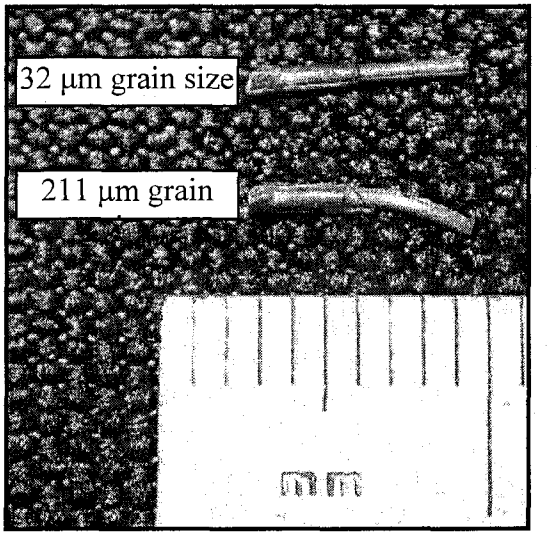

Figure 1.6 Samples of pins extruded using the Ø0.76:0.57 mm die and workpieces having a grain size of 32 μm or 211 μm.

The tendency of the submillimeter size coarse-grained pins to undergo inhomogeneous deformation is related to the relatively large portion of the workpiece occupied by individual grains. On average, less than four grains exist across the diameter of the pin when the 211 μm grain size material is used while the number of grains across the diameter of the workpiece for the 32 μm grain size is approximately 24. In Fig. 1.7, microstructure photos of a smallest size, Ø0.76/.57 mm coarse grained pin are given. By taking into account their shapes, the grains in the straight and the curved regions seem to deform differently. While the grains in the straight portion of the pins seem to be elongated more, the grains in the curved regions have rounded shapes. Also, for most of the curved pins grains at the curvature seem to be much larger. This would imply that the individual size, location and orientation of the 211 μm grains would have a significant impact on the deformation characteristics of the workpiece.

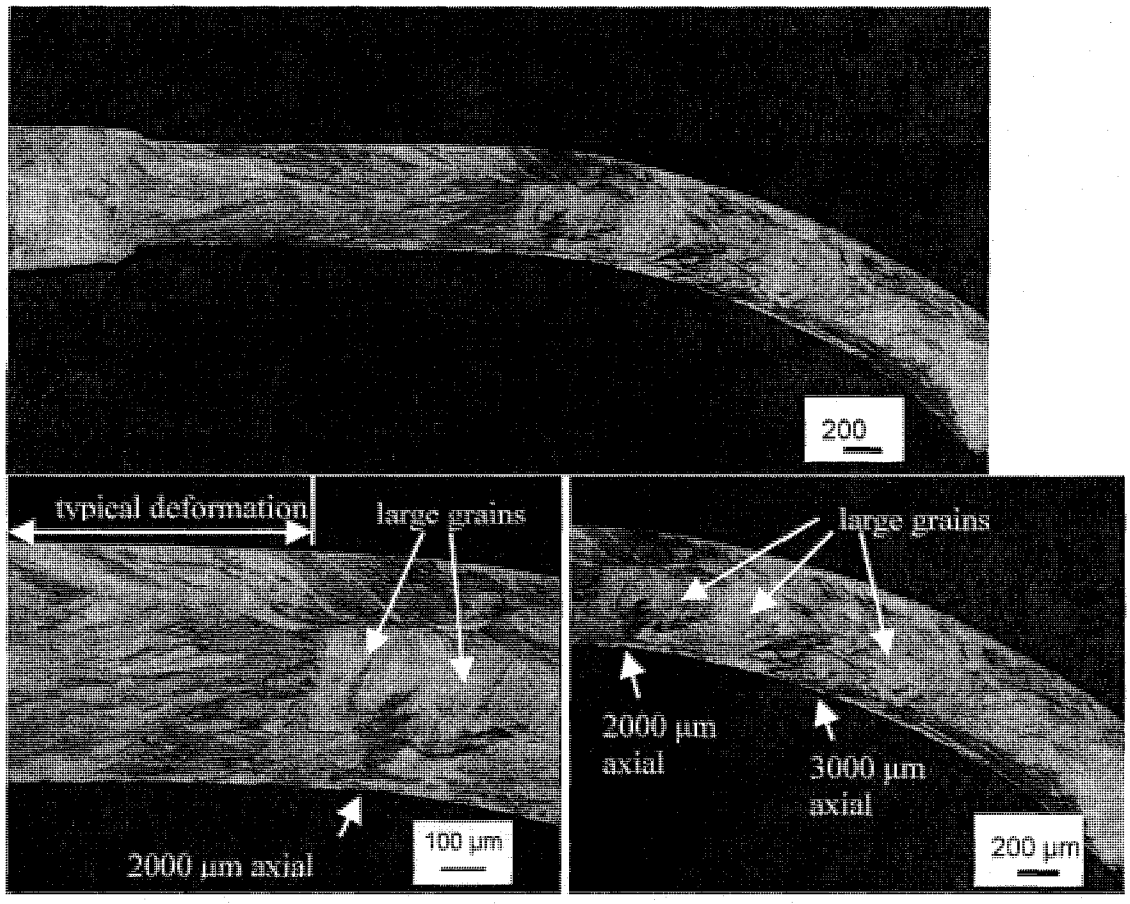

Figure 1.7 Microstructure photos of a smallest size, Ø0.76/.57 mm, coarse grained curved pin.

In all curved pins, the curving starts at the beginning of the extrusion, and once the curvature initiates, the pins continue to curve for a significant distance followed by a straight section. In Fig. 1.8 microstructure photos of additional smallest size, Ø0.76/.57 mm, coarse grained curved pins are given. It seems when a significant asymmetric deformation (both elastic and plastic) with respect to the axis of symmetry occurs at the beginning of the extrusion, asymmetric residual stresses accumulates with in the workpiece. This causes the subsequent material passing through the deformation zone to continue to flow in an asymmetric manner, which produces the curvature. The asymmetric flow in the curved region of the curved pins will be shown by X-Ray texture analyses later in this chapter.

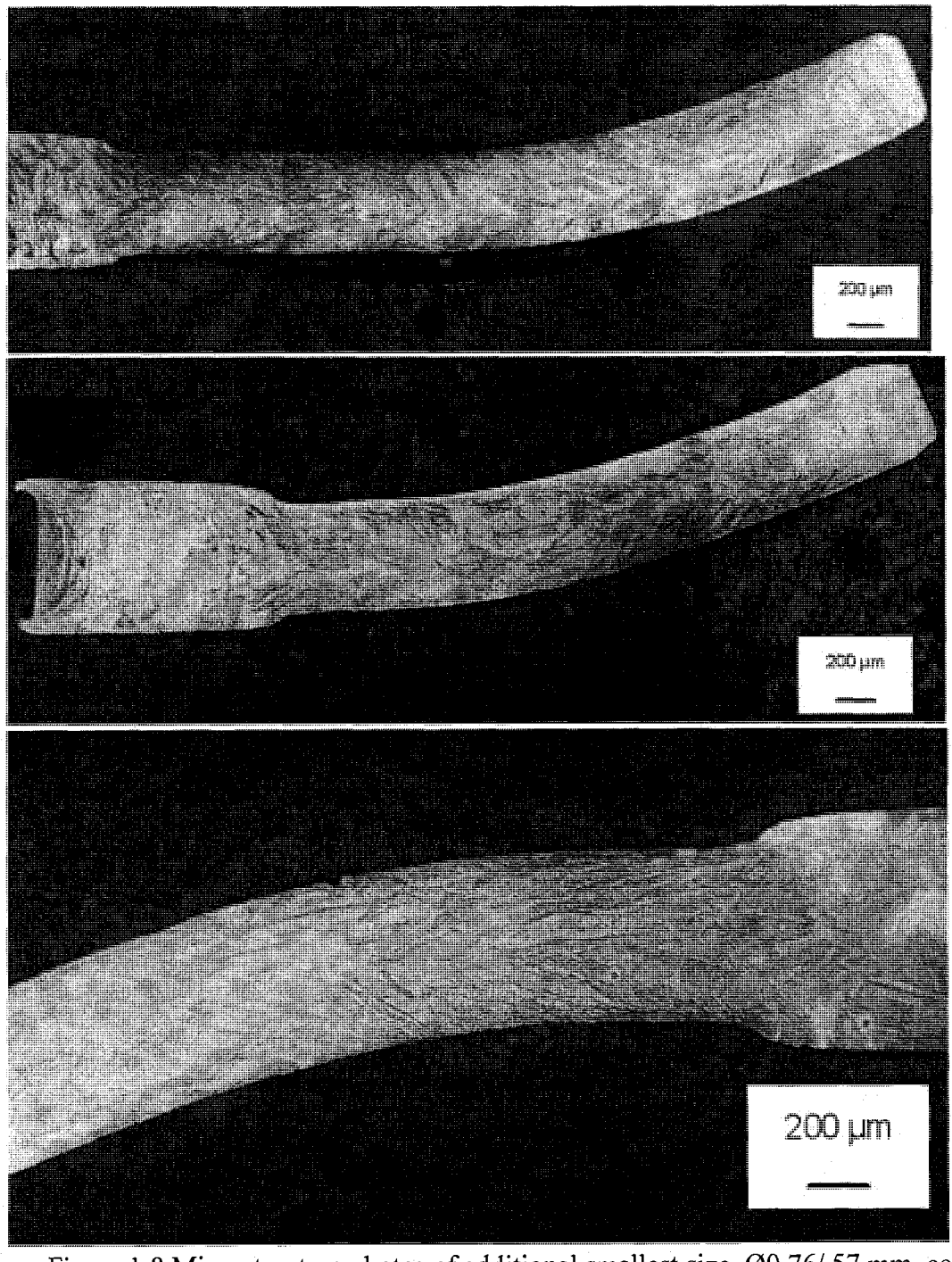

Figure 1.8 Microstructure photos of additional smallest size, Ø0.76/.57 mm, coarse grained curved pins.

The curving tendency occurs in the microextrusion of coarse grained smallest size pins in which only a few grains exit through the diameter, 3.7 grains on average. However, in this study, besides revealing shape irregularities that occur in

microextrusion, the main goal is to show the effect of specimen size and grain size on deformation. Thus, additional microstructure evaluations of the microextruded smallest size pins were performed.

The pins were polished and etched so the grain structure could be evaluated. Figure 1.9a shows the microstructure of the 32μm, fine-grained pin as it was reduced through the tooling and also a representative straight portion of the pin after reduction (see Fig. 1.9b). The microstructure is typical of what is observed in macroscale extrusion, i.e., the deformation pattern is consistent through the length of the pin with more deformation occurring on the outer surface.

The microstructure photos of the reduction area and a representative straight portion of the smallest size 211 μm, coarse-grained pin after reduction are presented in Fig. 1.10 There are 5 to 9 grains with different sizes present through the diameter in the straight portion. These grains seem to have rotated and elongated during the extrusion process.

In general during extrusion, the material undergoes both compression and shear deformation. Compression deformation corresponds to the reduction in the area and shear deformation is related to redundant work due to the material flow through the die geometry. Also, friction is present which arises from the interaction of the material with the tooling surface. Due to more pronounced redundant deformation and friction, the material near the surface undergoes extensive shear deformation. The severity of the shear deformation decreases from the surface of the billet to the center.

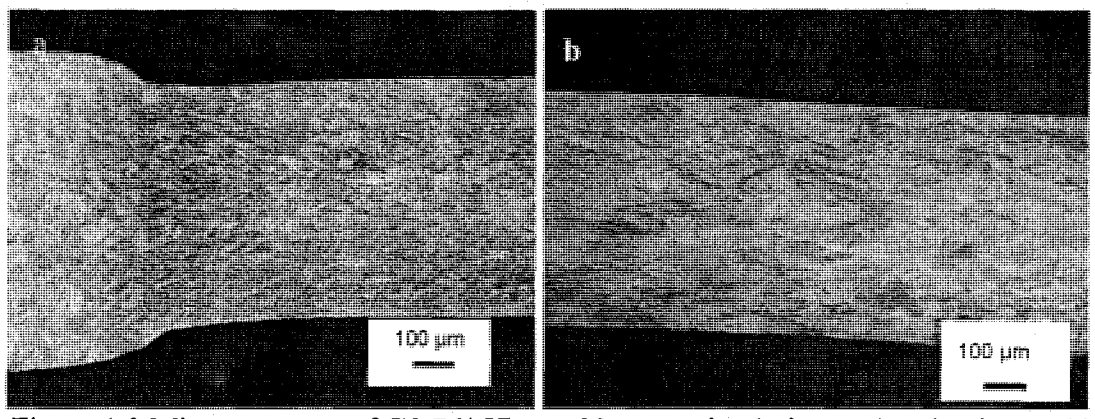

Figure 1.9 Microstructure of Ø0.76/.57 mm 32 µm grained pins at a) reduction and b) straight portion of the pin after reduction.

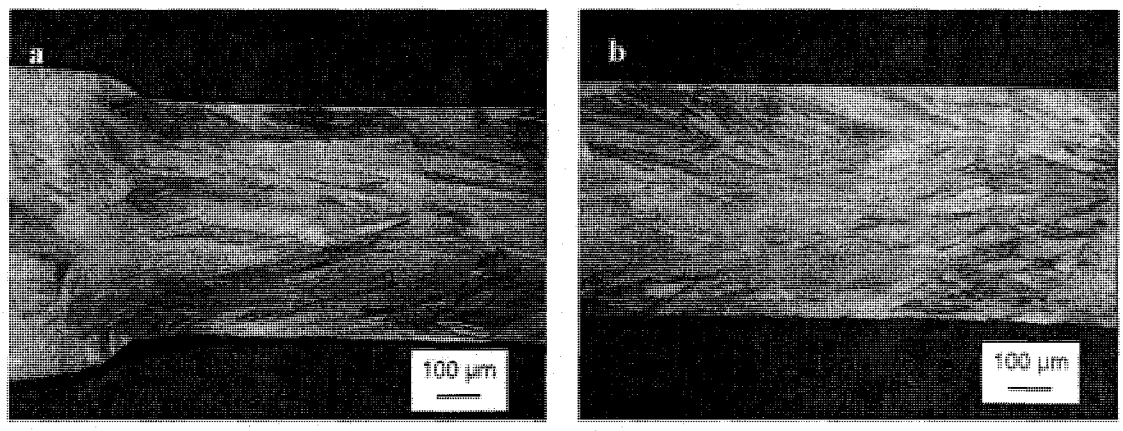

Figure 1.10 Microstructure of Ø0.76/.57 mm, 211 µm grain size pins at a) reduction and b) straight portion of the pin after reduction.

The grains undergo slip and rotation in a complex manner during extrusion that is determined by the above mentioned extrusion forces and by also the deformation of the adjacent grains [38]. For the 32 µm, fine-grained pins, there are approximately 24 grains through the diameter. The grains at the center area of these pins, like the grains in a macroextrusion specimen, are physically away from the highly sheared surface grains and thus undergo essentially pure elongation. The deformation within these fine grains is more homogeneous. However, the grains at the center area of the 211 µm, coarse-grained pins are one to four grains away from the surface. From this point of view, it is possible that the grains at the center region of the Ø0.76/.57 mm size coarse grained pins under go

more shear deformation. To further investigate this behavior microhardness evaluations are performed for all pin sizes and grain structures.

Microhardness Evaluations

During deformation, metals strain harden. As a result, their strength and hardness increase after deformation (i.e., the higher the plastic deformation, the higher the hardness of the material after deformation). In metal forming operations such as microextrusion where plastic strain gradients exist through the diameter of the workpiece, the deformation distribution can be characterized by a hardness evaluation through the cross section of the workpiece. However, it is acknowledged that characterizing the deformation via hardness evaluation is an indirect method and one can not obtain the actual strain amounts. In addition, as the strain increases, the change in hardness saturates. In Fig. 1.11 the correlation between the hardness of cold rolled CuZn30 brass and strain amount is shown (data obtained from [39]).

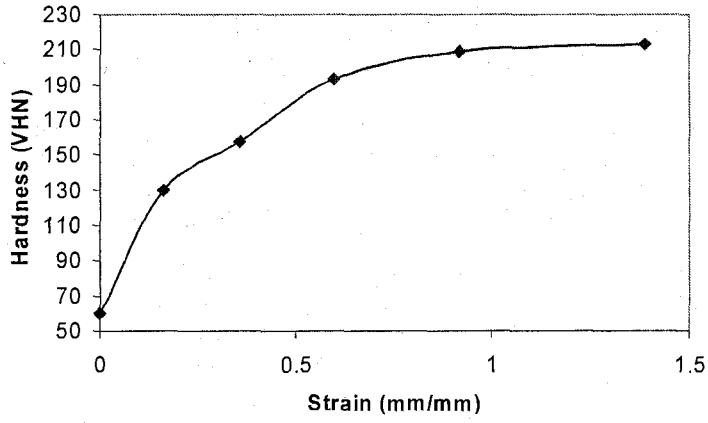

Figure 1.11 Correlation between the hardness of cold rolled CuZn30 and the strain (data obtained from [39])

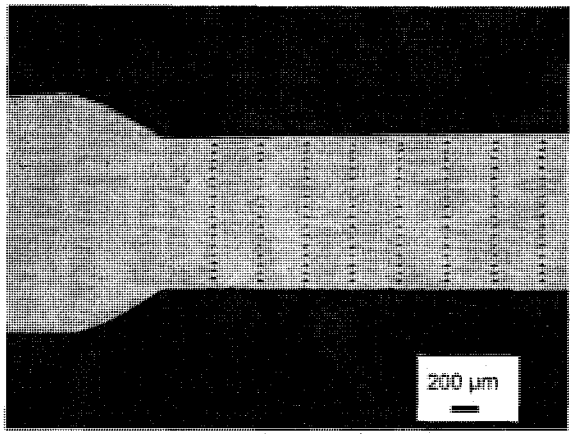

Figure 1.12 A photograph of a fine grained Ø1.5/1.0 mm pin after the microhardness evaluation.

In order to investigate specimen size and grain size effects on deformation during microextrusion, microhardness evaluations were performed on the microextruded pins with the three reductions. First, the pins were molded into epoxy and polished to their half longitudinal cross-sectional plane. Then, the microhardness measurements were obtained along the length of the pins after the reduction section using a Knoop indenter on a Beuhler Microhardness machine. In Fig. 1.12, a picture of a Ø1.5/1.0 mm fine grained pin after a microhardness evaluation is shown. Measurements were obtained with a 50 gram load and are spaced approximately, 50 µm. The Knoop indenter is an elongated pyramid. The hardness is obtained from the surface area of the indentation [27]:

$$HK = \frac{14.228P}{L^2} \tag{1.1}$$

where P is the load in kg and L is the length of the major diagonal in mm. A schematic of the indentation geometry for a Knoop indenter is shown in Fig. 1.13. The ratio between the dimensions of the indentation is:

h/w/L=1:4.29:30.53

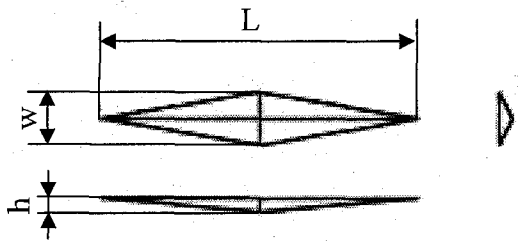

Figure 1.13 Schematic of indentation geometry for a Knoop indenter.

For the submillimeter size ∅0.76/0.57 mm pins, the hardness measurements were performed before and during the reduction section, as well. In Fig. 1.14 hardness profiles before and during the reduction of one of the 32 μm, fine-grained pins are presented. As expected, the hardness increased significantly during the reduction section of the tooling from 0.76 mm to 0.57 mm in diameter (which occurs at axial locations -500 μm to 0 μm). The hardness values in the radial direction are relatively uniform prior to the reduction section of the tooling as can be observed at an axial location of -650 μm in Fig. 1.14 with a consistent value of 140 HK. This value is approximately 50 HK higher than the billet material (see Fig. 1.14). This shift in the hardness is due to the strain hardening which arises from the compressive deformation of the material between the ram and the die. The material in the center of pins (i.e. near the radial location of zero) is the first to enter the reduction section of the tooling as can be observed by the increase in hardness near the zero radial location for axial locations of -500 and -350 μm in Fig. 1.14. This pattern of deformation through the reduction section is consistent with observations for macroscale extrusion [29]. For the 211 μm, coarse-grained pins, while similar behavior is observed at the reduction portion, the hardness values are more scattered through the diameter compared to the fine-grained pins due to the coarser grain size.

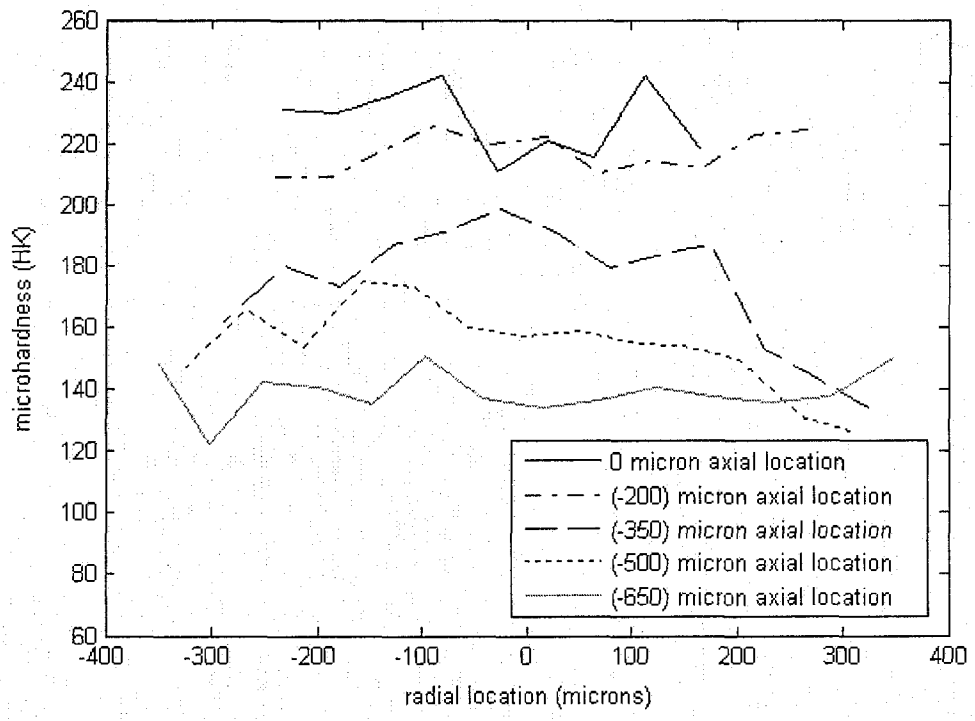

Figure 1.14 Hardness values in the reduction area for a 32 μm grain size pin. Zero radial location corresponds to axis of symmetry of the pin.

Microhardness evaluations of the undeformed (unextruded) billets in the annealed condition were also conducted to determine the initial hardness of the fine and coarse structures before extrusion. Figure 1.15 shows the average hardness distribution through the diameter of the undeformed fine grained and coarse grained billets with a Ø0.76 mm diameter. The fine grained billets have relatively higher hardness than the coarse grained billets. Note that the 211 μm, coarse grained billets have lower hardness in the center of the billets as a result of prior cold working.

In Fig. 1.16a, the average hardness measurements through the radius of the largest size pins which have Ø2.0/1.33 mm diameters are given for the fine and the coarse grained structures. For each microextrusion case, two pins were measured and the hardness values were averaged. Also, to obtain a better averaging effect, the hardness values in the radial direction from the axis of symmetry were also averaged. Each data

point in Fig. 1.16 represents an average of approximately 40 hardness measurements. Consistent with the deformation distribution through the radial direction in conventional macroscale extrusion, both fine and coarse grained pins have higher hardness near the surface due to additional extensive shear deformation and lower hardness in the central region. As is typical in macroscale forming, the fine grained structure has higher hardness than the coarse grained structure after extrusion. For this largest size pin case, 4.7 grains on average exist through the radius of the coarse grained pins and the results seem to be consistent with expected conventional macroscale extrusion.

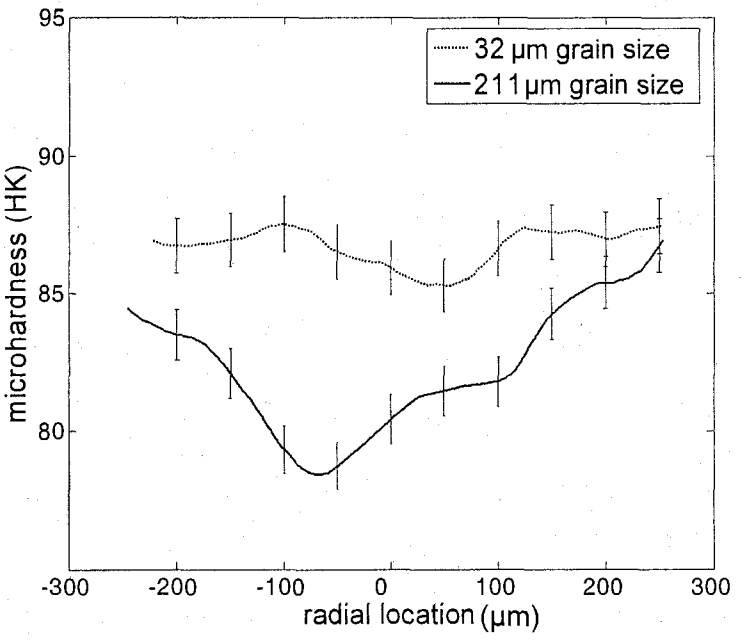

Figure 1.15 Average hardness distribution in the undeformed fine and coarse grained billet material.

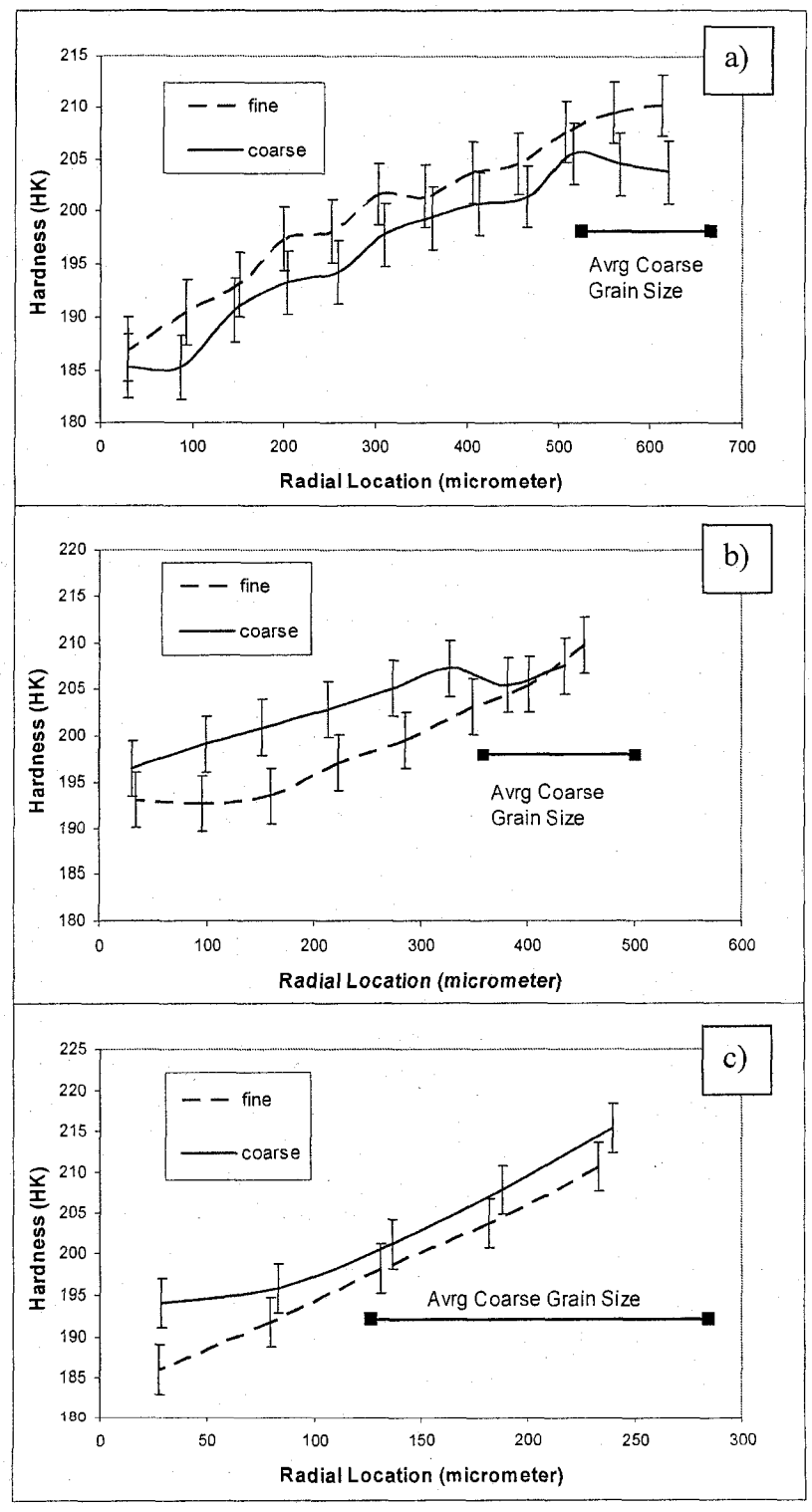

Figure 1.16 The average hardness profile of the fine and the coarse grained pins which have a) Ø2.0/1.33mm, b) Ø1.5/1.0mm and c) Ø0.76/0.57mm dimensions. Radial distances are from the axis of symmetry (from zero) to the outer surface.

The average hardness profile of the middle size pins which have Ø1.5/1.0mm dimensions are given in Fig. 1.16b. Contrary to undeformed billets and the largest size pins, the coarse grained pins, which have 3.5 grains through the radius on average, have higher hardness than the fine grained pins in the middle and central regions. For the middle size pins, these regions are roughly 0 to 150 μm for the central region, 150-325μm for the middle region and 325-450μm for the surface region with respect to the center of the pin.

For the smallest Ø0.76/0.57 mm pins, the coarse grained structure, which have 1.8 grains through the radius on average, again have higher hardness than the fine grained structure especially in the central region. However, contrary to the middle size pins, the smallest pins also have higher hardness near the surface region as well, Fig. 1.16c. The higher hardness of size pins, i.e., for the Ø1.5/1.0mm and Ø0.76/0.57mm pins especially at the central region, indicates some changes in the deformation occur during microextrusion when the grain size becomes comparable to the specimen feature size due to miniaturization. It should be noted that the effects observed in Fig. 1.16 should be considered trends since the error bars overlap. However, since the hardness values saturate at high strain levels (see Fig. 1.11) a small difference in hardness occurs as a result of considerable change in the strain values. Also, as previously mentioned each data point in Fig. 1.16 represents an average of approximately 40 hardness measurements and these trends show the average behavior of coarse and fine grained structures. The error bars in Fig. 1.16 show the range of measurement errors. The error bars are calculated by taking into account the wavelength of the light which is 0.5 μm. For a given indentation, this would be the error in the measured L value for Eq. (1.1). Using 50 g for

the applied load, P, the error range for the measurements is about ±3 HK. Standard deviations of the hardness measurements were also calculated. It is seen that the standard deviations are different for fine and coarse grain sizes and are independent from the specimen size. The average standard deviation is found to be 4.7 HK for the fine grained pins and 8 HK for the coarse grained pins.

In order to investigate the specimen size effect on the deformation for the coarse and fine grained pins separately, the radial location was normalized by dividing the radial distance of the pins by the radius. Then all the hardness profiles for the three different microextrusion sizes were plotted together for a given grain size. The amount of strain, ε, induced merely due to the reduction in the area during extrusion can be calculated from

$$\varepsilon_{RA}=\ln (A_i/A_f) \tag{1.2}$$

where A_i and A_f are the cross-sectional areas before and after deformation respectively. Since CuZn30 is a strain hardening material, strain and hardness measurements are related.

In Fig. 1.17a, the hardness profiles of the coarse grained pins for the three different microextrusion sizes are plotted. The middle size pins, with Ø1.5/1.0 mm dimensions, have similar hardness values with the largest size pins, with Ø2.0/1.33 mm dimensions, near the surface region. However, although these pins underwent the same extrusion ratio of 2.25 and 81% strain is produced due to area of reduction according to Eq. 1.2, the middle size pins have significantly higher hardness in the middle and central regions than the largest pins. This occurs due to the penetration of shear. The smallest pins, the Ø0.76/0.57mm case, have a lower extrusion ratio of 1.77 and a 57.5% strain is produced during extrusion in the workpiece merely due to the reduction in the area which

is calculated according to Eq. 1.2 which is less than the larger sized pins. Although, the smallest pins have a lower extrusion ratio, the hardness in the surface region is highest for this case among all three sizes. Furthermore, the smallest pins have higher hardness than the largest pins, Ø2.0/1.33 mm case, in the middle and central regions, as well. Based on these results, miniaturization in microextrusion increases the total strain experienced by the coarse grained structure due to the penetration of shear which results in pins having higher hardness especially in the central region. The penetration of shear occurs probably due to the steeper strain gradients which increase with miniaturization. The effect of miniaturization on the deformation and hardening of the fine grained structure is not as evident, Fig. 1.17b. It seems the hardness (i.e., the deformation) distribution through the diameter is independent from the specimen size for fine grained structure. Although the smallest size pins experience less area reduction, similar hardness values were obtained for all three sizes, Fig. 1.16b.

One possible explanation for the increased hardness of the coarse grained pins compared to the fine grained ones with miniaturization is that the coarse grained pins have a higher friction coefficient. However, as mentioned previously, friction is a surface effect, and the increased hardness occurs consistently in the central region. Comparison of the hardness profiles of the largest and the middle size pins which have both coarse structures supports these arguments, see Fig. 1.17a. Although, the largest and middle size coarse grained pins have similar hardness values in the surface regions, the middle size pins have higher hardness in the central regions. In addition, the coarse and fine grained pins were extruded with the same dies, and Mori et al. showed that the friction coefficient of CuZn30 is independent of grain size during unlubricated, testing under high pressure

[40]. In Fig. 1.16b, for example, the coarse and fine grained pins have similar hardness values in the surface region, but the coarse grained pins begin to have higher hardness in the inner regions.

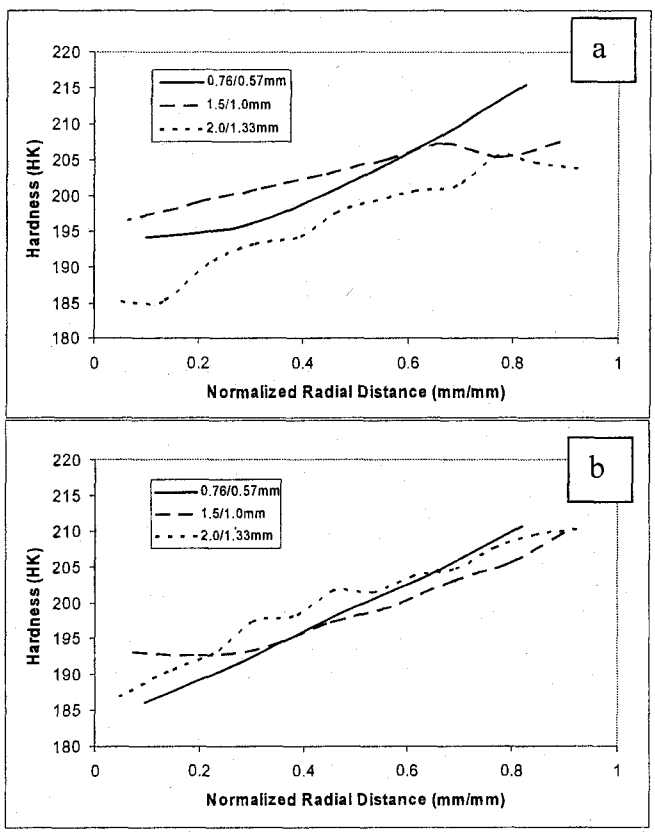

Figure 1.17 The average hardness versus normalized radial distance for all microextrusion sizes for the a) coarse grained structure and b) fine grained structure.

<u>The Effect of Surface Grains on Deformation Distribution through the Radial Direction</u>

The surface grains are the only grains that have direct interaction with die surface and thus, are most affected by friction. Furthermore, the surface grains experience the most shear deformation due to the deformation geometry, as well. For the coarse grained pins, the volume of the surface grains to the total volume of the pin ratio is large. Therefore, the hardness distribution through the radial direction of the coarse grained pins is affected by the surface grains.

The average length that is occupied by the surface grains through the radial direction after the reduction is approximated by multiplying the average pre-deformation grain size with the extrusion ratio. For the coarse grained structure, the average length that the surface grains occupy for each pin size is indicated with a horizontal line in Fig. 1.15. For the largest and middle size coarse grained pins a significant change in the hardness profile occurs at a radial distance where surface grains are present, Fig. 1.16a and b. The hardness values increase gradually through the central and middle regions and in the surface region where surface grains exist a plateau in the hardness profile occurs. For the smallest size pins where the share of the surface grains is very high, Fig. 1.16c, a change in the hardness profile again seems to occur near this material length scale. For this case, the hardness values decrease gradually from the surface to central region and at the radial distance where surface grain zone ends the decreasing trend in the hardness diminishes. Thus in microextrusion, when grain size becomes comparable to specimen feature size, the deformation distribution is affected by the surface grains. This deformation distribution would also be affected by the reduction ratio and friction.

In addition as it was mentioned before the grains undergo slip and rotation in a complex manner during extrusion that is determined by the extrusion forces and by also the deformation of the adjacent grains. For the 32 μm, fine-grained pins, there are many grains through the diameter. The grains at the center area of these pins, like the grains in a macroextrusion specimen, are remote from the highly sheared surface grains and thus undergo essentially pure elongation. However, the grains at the center area of the 211 μm, coarse-grained pins are one to four grains away from the surface. From this point of view, it is possible that the grains at the center region of the Ø0.76/.57 mm and Ø1.5/1.00 mm

size coarse grained pins undergo more shear deformation. To further investigate this behavior X-Ray pole figure analyses are performed for all pin sizes and grain structures.

X-Ray Pole Figure Texture Analyses

To characterize the penetration of shear of coarse grained pins with miniaturization, X-Ray pole figure texture analyses were also conducted on the longitudinal cross-sections of the pins just after the reduction section with a Bruker AXS X-Ray diffraction machine. First, the pins were mounted in epoxy and polished to their half longitudinal cross sections. In order to avoid diffractions from other locations, the rest of the pins were covered with tape. In Fig. 1.18, a schematic representation of the X-Ray texture analysis is shown. The details of the X-Ray pole figure analyses are given in Appendix A.

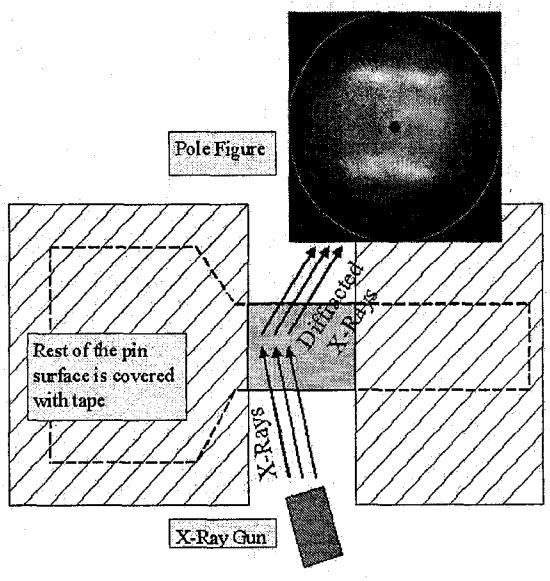

Figure 1.18 Schematic of the X-Ray texture analyses.

The textures of the smallest pins, the Ø0.76/.57 mm case, are of interest because if there is a trend of penetration of shear during microextrusion, this affect would be most

pronounced in the extrusion of the smallest size pins where the imposed strain gradients by the deformation geometry are the steepest. Additional texture analyses were also performed on the largest size coarse grained pins for comparison. Finally, pole figures of unextruded fine and coarse grained billets were also obtained to show how the texture evolved during extrusion.

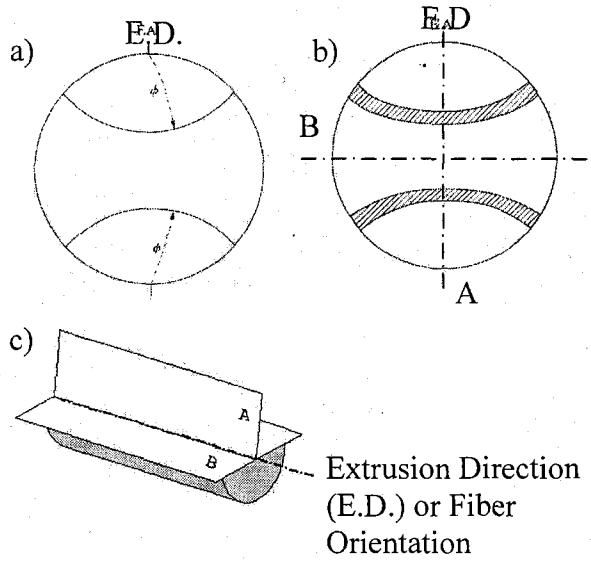

Figure 1.19 a) Perfect [30] and b) imperfect [100] fiber texture for a (111) pole figure and c) two possible mirror planes for deformation in extrusion.

As mentioned previously during extrusion deformation gradients are present through the diameter. Thus, because of these deformation gradients through the radial direction, texture gradients are present through the diameter of the workpiece after extrusion. However, in the central region, as a result of axisymmetric deformation, the grains of the polycrystalline metals slip and rotate until they reach a stable orientation and develop rotationally symmetric, fiber texture. FCC metals generally develop a <111> or <100> or a mixture of both orientations, parallel to the extrusion direction [41]. In Fig. 1.17a, a schematic of a pole figure which shows a perfect fiber texture is given. The angle between the extrusion direction (E.D.), i.e. fiber axis, and the diffractions is constant

which shows rotational symmetry of deformation and texture in extrusion [38]. Moreover, the pole figures of forming processes such as rolling and extrusion typically exhibit symmetry due to the inherent symmetric deformation in the process [42]. For example, the pole figures that are obtained from longitudinal cross-sections of extruded samples reflect symmetry according to the two mirror planes of the deformation indicated in Figs. 1.19b and c. The real textures obtained after extrusion are generally imperfect, due to variations in the final orientation of material.

At the very outer surface due to the frictional interactions, the texture of the surface exhibits a shear characteristic. However, this frictional effect is limited to a thin surface layer [43, 44]. In rolling, Asbeck and Mecking have shown depending on the geometry of deformation, penetration of shear occurs and the intermediate layers can also undergo some shear deformation [45]. This is one of the reasons that the textures obtained after extrusion or wire drawing are imperfect, Fig. 1.17b.

Truszkowski et al. [46] reported shear texture which is close to a {001}<110> orientation at the surface of cold rolled commercially pure aluminum with an area reduction ratio of 87.5% .The texture obtained from the intermediate layer , i.e. at s=0.5 (where s is a normalized distance such that s=0 indicates the central plane of the workpiece and s=1 is the surface), seems to have 7° rotational relationship with the texture of the central region (s=0) about the transverse direction.

Choi et al.[47] and Lee et al. [48] have studied texture gradients and penetration of shear in rolling and extrusion and these works are summarized in Table 1.1 In order to perform texture analyses separately on different areas during the rolled sheet study, layers of material were cut from surface, central and middle regions of rolled sheets, and texture

analyses were conducted on these layers. For extrusion, a complex cutting procedure was applied because the workpiece was cylindrical. In Table 1.1, in addition to the orientation parallel to the rolling/extrusion direction, the indices of the rolling plane are also given in brace.

Table 1.1 Summary of two studies on texture gradients in rolling and extrusion of Al 1100

Process (material)	Area of Reduction	Texture of Central Region	Texture of Middle Region	RRB* center and middle	Texture of Surface Region	RRB* Center and Surface	Ref.
Rolling (Al)	55%	major {112}<111> minor {110}<100>	{113}<322> {331}<611>	10° 13°	{118}<441> {332}<311>	25° 25°	Choi et al. [47]
Extrusion (Al)	93.6%	strong <111> weak <100>	<111> <100>	0° 0°	<335>	14.5°	Lee et al. [48]

*RRB: Rotational Relationahip Between

Choi et. al. [47] who performed texture analyses on cold rolled aluminum sheets which underwent a 55% reduction found that the texture of the central layer consisted of approximately a major {112}<111> and a minor {110}<100> orientations while the texture of the intermediate layer (s=0.5) consists of approximately {331}<116> and {113}<332> orientations. The orientation components of {331}<116> and {113}<332> have rotational relationships with {110}<100> and {112}<111> orientations about the transverse direction of 13° and 10° respectively. The surface texture consisted of {332}<113> and {118}<441>, which are very close to the well known shear orientations of {111}<112> and {001}<110> respectively. Both measured surface textures of {332}<113> and {118}<441> have a 25° rotational relationship with {110}<100> and {112}<111>. Furthermore, the textures of intermediate and surface layers do not show texture symmetry.

Lee et al. [48] investigated texture gradients through the radial direction of extruded 2014 aluminum alloy with a 93.6% reduction in the area. They reported <111> and weak <100> fiber textures from central and intermediate layers and approximately {110}<335> from the outer layer, where {110} corresponds to the plane normal to the radial direction and <335> corresponds to the direction parallel to the extrusion axis.

Therefore, with regard to knowledge mentioned above, the texture that is evolved during extrusion can be summarized as follows: During extrusion, FCC metals usually develop axially symmetric <111> and <100> fiber textures parallel to the extrusion direction. However, the textures that are obtained from extruded workpieces are not perfect textures since the deformation is not homogeneous through the cross-section and deformation gradients are present. While the material in the surface region experiences excessive shear deformation, the material near the axis of symmetry experiences pure elongation and deformation changes gradually from the surface to the central region. Because of this, texture gradients are also present through the diameter of extruded workpieces. The, well known axially symmetric <111> and <100> fiber orientations [41] are developed in the central region. In contrast, textures in the middle region have some rotational relation with these axially symmetric orientations due to the penetration of shear. The material in the surface region has more shear related textures.

In Fig. 1.20a, the <100> and <111> pole figures obtained from an unextruded fine grained billet are shown. The billet material is in an annealed condition, has a diameter of Ø0.76mm, and 24 grains exits through the diameter on average. No significantly strong texture is present in the material before extrusion. However, after extrusion with an extrusion ratio of 1.77 for the Ø0.76/Ø0.57 mm case, the fine grains slip and rotate

according to the deformation geometry and develop an axially symmetric <111> fiber texture, see Fig. 1.20b. The diffractions are diffuse and thus have an imperfect characteristic which occurs due to the deformation gradients through the radial direction of the pin. Also, the diffractions reflect the symmetry of deformation in extrusion and show rotational consistency with respect to the axis of symmetry. The pole figures obtained from other fine grained smallest size pins also have similar <111> textures with diffuse diffractions. Thus, the pole figures of the microextruded fine grained structures resemble the texture obtained from conventional macroscale extruded workpieces. Note that the pole figures obtained are incomplete because no diffractions are obtained in the surface regions of the pole figures. Diffractions up to 65° from the surface normal were obtained.

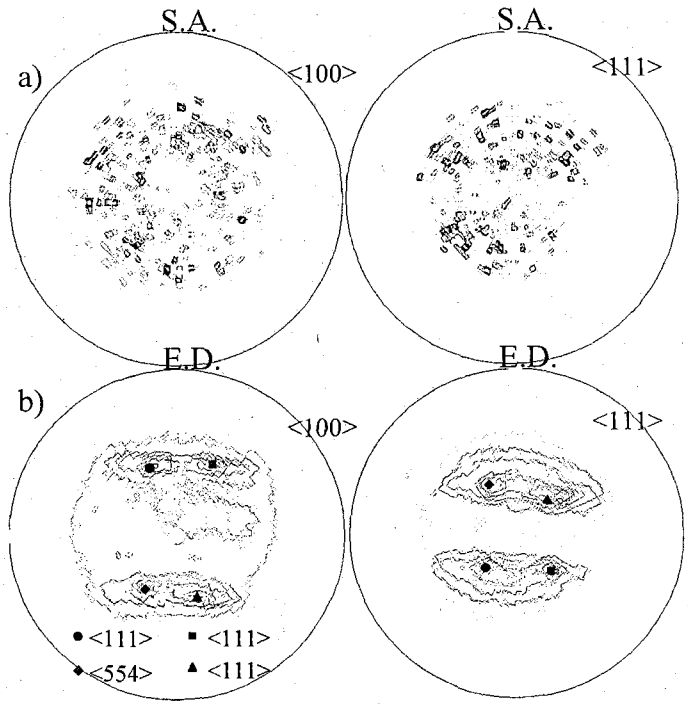

Figure 1.20 Pole figures for a fine grained a) undeformed billet Ø0.76 mm and b) a pin after extrusion, Ø0.76/0.57 mm. (S.A.: symmetry axis; E.D.: extrusion direction)

In Fig. 1.21a, the pole figures obtained from an unextruded coarse grained billet in an annealed condition which has a Ø0.76mm diameter are shown. On average, 4 grains are present through the diameter. Similar to the fine grained billets (Fig. 1.20a), the pole figures do not show a significantly strong texture. However, less diffraction are present due to the limited number of grains in the cross section. In Fig. 1.21b, the pole figures obtained from a smallest size coarse grained pin after extrusion to Ø0.57 mm are given. The pole figure is obtained from the straight region of the coarse grained pin just after the reduction section. Note that curving occurs during microextrusion in most of the smallest size coarse grained pins (approximately 80%).

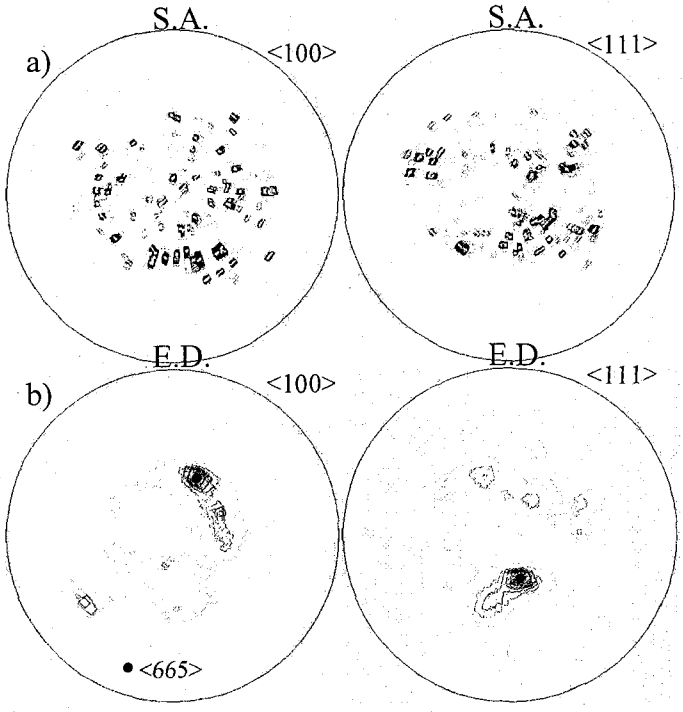

Figure 1.21 Pole figures of a coarse grained a) undeformed billet, Ø0.76 mm and b) straight section of a curved pin, Ø0.76/0.57 mm.

In general, the diffracted poles of the coarse grained pins, Fig. 1.21b, are significantly strong and do not exhibit a diffuse characteristic as the ones presented in Fig. 1.20b for the fine grained pins. In addition, the pole figures obtained from the

smallest size coarse grained pins do not have axially symmetric fiber orientations parallel to the extrusion direction. In fact the orientations that are developed have some rotational relationship with the axially symmetric <111> orientation. For the pole figures that are presented in Fig. 1.19b, a <665> orientation parallel to the extrusion direction exists which has a 4.8° rotational relation with the <111> orientation. The two other smallest size coarse grained pins that were used in the X-Ray texture analyses have similar <665> and <433> orientations parallel to the extrusion direction which have 4.8° and 8° rotational relationships with the axially symmetric <111> orientation respectively. The obtained orientations for the smallest coarse grained pins show that there is a trend of penetration of shear deformation in microextrusion of the coarse grained structure with miniaturization.

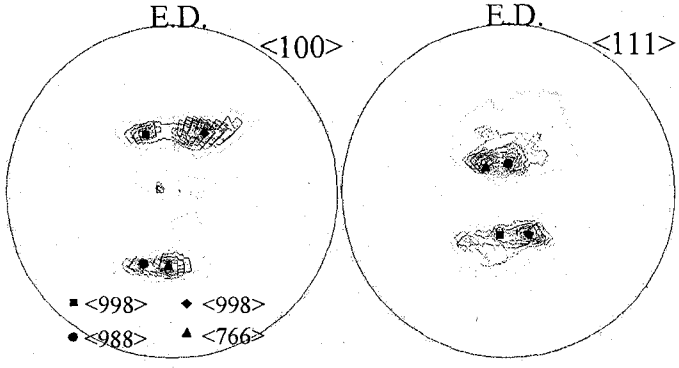

Figure 1.22 Pole figures of a largest size, Ø2.0/.1.33 mm, coarse grained pin which is obtained on a longitudinal cross-section just after the reduction.

In Fig. 1.22, the pole figures obtained from the largest size pin, which has a coarse grained structure and dimensions of Ø2.0/.1.33 mm, are given. As the pins approach the macroscale, their pole figures begin to show similarities with the pole figures of the fine grained smallest pins in Fig. 1.20. The pole figures have four diffractions which have <998>, <998>, <988> and <766> orientations parallel to the extrusion direction, and

have relatively similar intensities. It should be noted that the extrusion ratio for the two large pin cases is 2.25 which is higher than that of the smallest pin case (1.77).

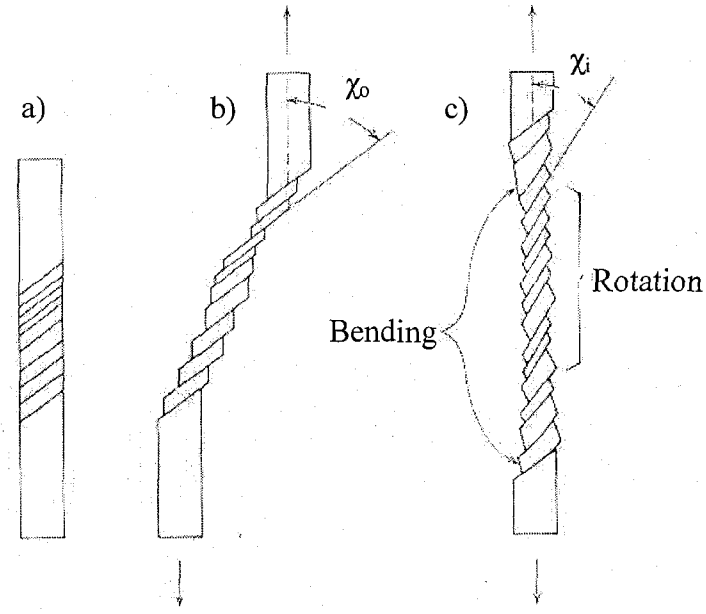

Figure 1.23 Schematic of the orientation of a single crystal slip plane a) prior to deformation, b) after deformation without grip constraint, and c) after deformation with grip constraint (note that $\chi_i < \chi_o$) [49].

Another finding of this part of the thesis was the curving tendency of the coarse grained pins for the smallest die set. The X-ray texture analyses can also provide information for this behavior. Hertzberg has shown the possible deformation of a single crystal under uniaxial tension; see Fig. 1.23 [46]. If the crystal is not constrained by the grips, the planes will slide without changing their relative orientation to the loading axis which resembles "the offsetting groups of playing cards on a table" [49], see Fig. 1.23b. However, due to the constraints imposed by the grips, the slip planes are forced to rotate with respect to the tensile axis which results in rotation and bending of the crystals, especially near the end grips, see Fig. 1.23c. When the specimen is released from the grips, the internal elastic stresses which arise from rotation and bending of the crystal will

also release and this will likely result in curving of the specimen physically near the grip sections. Thus, although the imposed forces by the grips are axisymmetric, the deformation of the crystal is not axisymmetric due to the rotation of the crystal. This can be the case for deformation of single crystals and also can be the case when there are only a few grains through the cross-section.

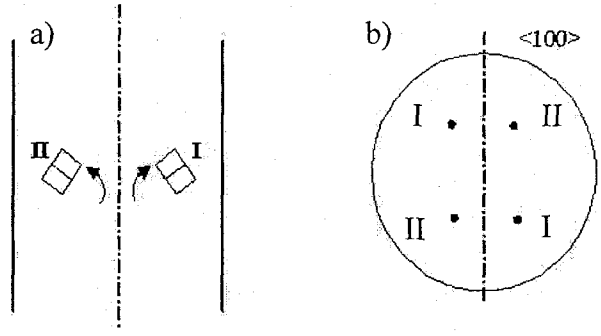

Figure 1.24 Schematic of the a) rotation of two grains during uniaxial deformation and b) corresponding <100> pole figure for these grains.

In uniaxial deformation of polycrystals such as deformation during extrusion, the rotation of the grains with respect to the mirror plane A should be symmetric and the pole figures should reflect this behavior. In Fig. 1.24a, a schematic of the rotation of grains during uniaxial deformation is given. All the rotations and orientations of the grains in the cross-section are reduced to two representative grains for simplicity and the grains were presented with their unit cubic lattice. Their rotation during deformation ended with a <111> orientation parallel to the loading axis and they have {110} planes parallel to the surface. During axisymmetric deformation, if some grains rotate clockwise (represented by grain I), some grains should rotate counter clockwise (represented by grain II) to maintain symmetry with respect to plane A. As a general result, their pole figures should

reflect this symmetry. In Fig. 1.22b, the <100> pole diffractions of grains I and II are given.

The pole figures obtained from curved regions of the coarse grained pins can be informative from this point of view. In Fig. 1.25, a pole figure which was obtained from an area on the curved region of the pin presented in Fig. 1.7 is shown. There is a very coarse grain in the center at this particular area and the two significantly strong diffractions probably belong to this particular grain. The grain has a <14 13 12> orientation parallel to the axis of symmetry and its plane that is parallel to the surface has a rotational relationship with a {110} plane. While performing the X-Ray texture analysis, the sample's symmetry axis on the curved region is taken into account. During microextrusion, this grain seems to slip and rotate according to the deformation constraints of the die and develop a final orientation which is close to the axisymmetric <111> orientation with a 3.6° rotational relationship. But, when this part of the pin comes out of the die, the elastic stresses due to the rotation of the grain are released which causes the pin to curve. This cause of curvature is similar to that described with respect to Fig. 1.23c since there is one large grain in the center of the cross-section. Alternatively, any significant rotational asymmetry or significant larger flow of material at one side during deformation can also cause curvature to occur. A significant absence of symmetry in the pole figures with respect to plane A can be the indication of deviation from axisymmetric deformation regardless of the cause of curvature. The other pole figures obtained from the curved region of the coarse grained pins also do not show textural symmetry.

The strong diffractions of the pole figures that are obtained from the straight part of this particular coarse grained pin (Fig. 1.19bc) have a <665> orientation parallel to the extrusion direction and the corresponding plane that is parallel to the surface, has a rotational relationship with a {221} plane.

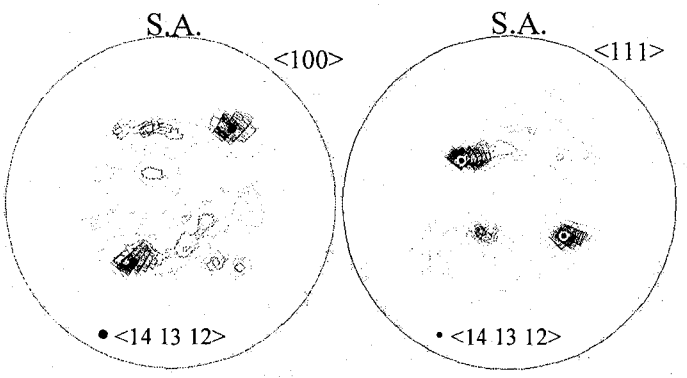

Figure 1.25 Pole figures obtained from the curved region of a coarse grained pin

The strong diffraction obtained from another coarse grained straight pin (Ø0.76/0.57 mm) on a longitudinal area just after the reduction (Fig. 1.26a) has a orientation of <433> parallel to the extrusion direction and has a plane that is parallel to the surface which has a rotational relationship with a {221} plane. In Fig. 1.26b, the pole figures obtained from a further area on the longitudinal cross-section from the same coarse grained straight pin is given. At this longitudinal cross-section, the texture of the pin shows a strong <544> orientation parallel to extrusion direction and the corresponding plane which is parallel to the surface has a rotational relationship with a {221} plane. In all these pole figures that are obtained from a straight longitudinal cross-section of the coarse grained pins, the diffractions are almost symmetric with respect to the mirror plane A, which is an indication of symmetric deformation with regard to this plane and explains why curvature does not occur at these locations. Because the X-Ray

texture analyses were performed from one side of the mirror plane B and due to the penetration of the shear deformation to the central regions, most of the pole figures obtained from the coarse grained pins do not have symmetry with respect to the plane B. Additionally, the textures of the straight coarse grained pin given in Figs. 1.26a and b, which are obtained from different axial locations show similarities which are an indication of consistent deformation along the axial distance in that particular pin. However, this is not the case for most of the coarse grained pins.

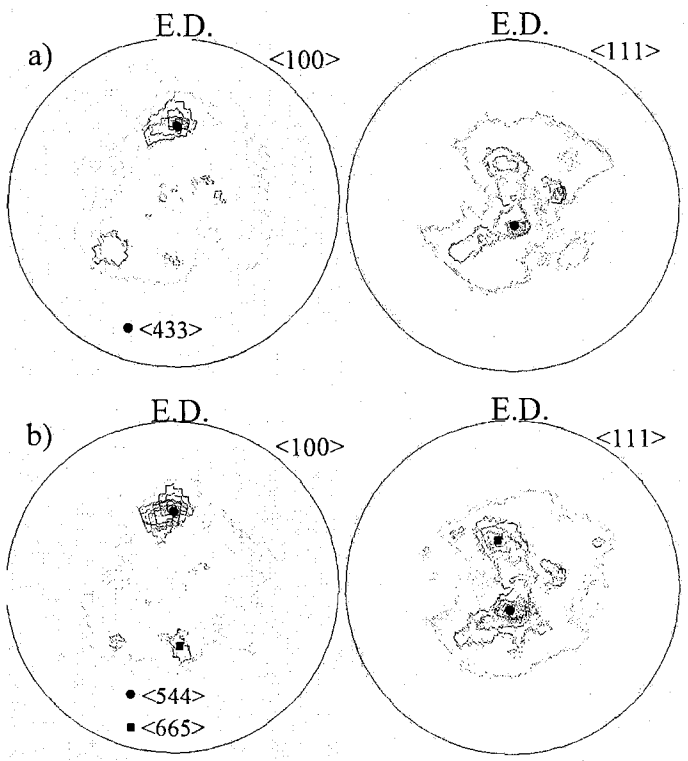

Figure 1.26 Pole figures obtained on the longitudinal cross-section of the coarse grained straight pin (not curved) a) from an area just after the reduction section b) from another area.

Conclusion of This Chapter

In this chapter, the dependence of deformation in microextrusion on specimen size and grain size was investigated. For the coarse grained pins, the hardness (i.e., deformation) distribution is affected by the specimen size, and as specimen size decreases

the coarse grained pins have higher hardness compared to fine grained pins at the central region. This indicates that changes occur in the deformation behavior of the miniaturized coarse grained pins. In addition, the hardness profile (i.e., the deformation distribution through the radial direction) for the coarse grained structure is affected by the surface grains which experience the most excessive shear deformation due to friction and deformation geometry during microextrusion. For the fine grained pins, the hardness distribution (i.e., deformation) distribution is independent from the specimen size.

Also using X-Ray Pole Figure Analyses, the asymmetric deformation in the workpiece which causes the curvature to occur during the microextrusion of the submillimeter size coarse grained pins is shown.

CHAPTER 2

MICROBENDING

Background

Sheet metal forming of parts with microscale dimensions is gaining importance due to the current trend towards miniaturization, especially in the electronics industry. With miniaturization, the process and product dimensions are scaled down but the grain size of the material remains the same. As a result, the number of grains in the deformed area of the workpiece decreases significantly. Due to the anisotropic nature of individual grains, the material becomes an inhomogeneous medium. Thus, increased scattering in the forming forces [4] and in the final bent geometry occurs [10, 50].

In addition, with miniaturization as the number of grains through the thickness is decreased, the influence of surface grains on the strength of the specimen increases. The surface grains are less constrained than inner grains, thus their flow strength is lower. With miniaturization, the share of the surface grains in the total volume of the specimen increases significantly. Thus, for a given grain size, generally as the specimen size (e.g., thickness) decreases, the strength of the specimen also decreases [1-4, 6-8, 50-53]. However in microbending, when there is only one grain through the thickness or the grain size exceeds the sheet thickness an increase in the bending force was observed with increasing grain size [4, 6].

In Fig. 2.1 the microbending results of Raulea et. al. is given [4]. In their microbending experiements the sheet thickness kept constant and the grain size was varied. The specimen thickness is 1mm and grain size varied from 0.015 mm^2 to 600 mm^2. The sheets were made from aluminum. When there are multiple grains through the thickness the maximum load and the force at yield point decreases with increasing grain size (left-hand size of Fig. 2.1). In the case of a single grain through the thickness (right-hand side of Fig 2.1), two effects were observed: a) the bending force increases with increasing grain size, and b) the reproducibility of the test decreases strongly with increasing grain size.

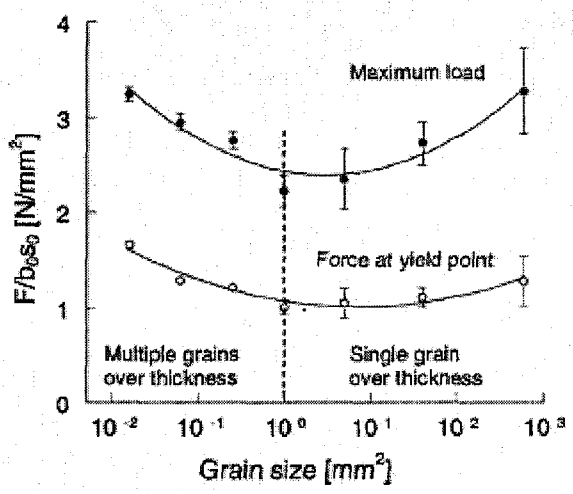

Figure 2.1 Variations of peak bending force and force at yield point for bending experiments (specimen thickness 1 mm) [4].

Bending is a widely used metal forming operation to create localized deformations in sheets to achieve the desired final part geometry [54]. Due to the stress and strain gradients in the cross-sectional area of bending, an inhomogeneous deformation occurs. During bending, the metal on the outside of the bend radius becomes stretched or elongated from tensile stress, while metal on the inside of the bend radius

experiences compressive stress. Maximum stresses and strains occur at the outside and inside surfaces and they gradually decrease from the surface to the neutral axis. The neutral axis is the line of zero stress and strain in a bend. When the metal is stressed above its elastic limit, it is plastically deformed. During bending, the plastic deformation first occurs at the surfaces and as the degree of bending is increased the plastic deformation increases and penetrates into the inner regions. Because of these inhomogeneties in the deformation, analyses of stress and strain distribution through the thickness are of utmost importance when evaluating bending and springback effects.

In bending, the elastic recovery of the material when the punch is retraced will cause the material to "springback". Predicting the springback amount is very important for the sheet metal industry to achieve the desired final part geometry; thus, the effect of miniaturization on springback has been investigated [7, 10, 50, 55]. Some researchers have found that coarse microstructures tend to springback less than fine microstructures [7, 50]. Diehl et al. claims this behavior occurs due to the influence of the increased share of the surface grains [50]. In addition, the scatter in the springback angle increases with miniaturization [7, 50].

Engel and Eckstein used an optical strain measurement technique to investigate the strain distribution in 0.5 mm thick microbent CuZn15 sheets. The distribution of the strain was consistent with the typical macrosize bending for the spring hard, fine-grained (10 □m) sample. However, for the annealed 70 □m grain sized material, a more scattered deformation distribution existed due to the effects of grain size and orientation [52].

In this chapter the influence of the specimen size and the grain size on the distribution of plastic deformation through the thickness after 3-point microbending operations is investigated via microhardness evaluations.

Experimental Procedure

To investigate the effect that specimen size has on deformation size effects, specimens which have thicknesses of 1.625mm, 0.5 mm and 0.25 mm were used. The microbending tooling used for each size was designed according to the theory of similarity. Thus, all dimensions of the tooling which contribute to the bending have the same ratio to the sheet thicknesses. The ratio of the punch and die radii to the thickness of sheets is 1.5t (i.e., R=1.5t) and the die gap has a 2t clearance from both sides of the punch. Thus, the total width of the gap L_d is 7t. A schematic of tooling is shown in Fig. 2.2 The dimensions of the specimens were designed according to the theory of similarity as well. To ensure a plane strain deformation, the width of the specimens were chosen as w=10t.

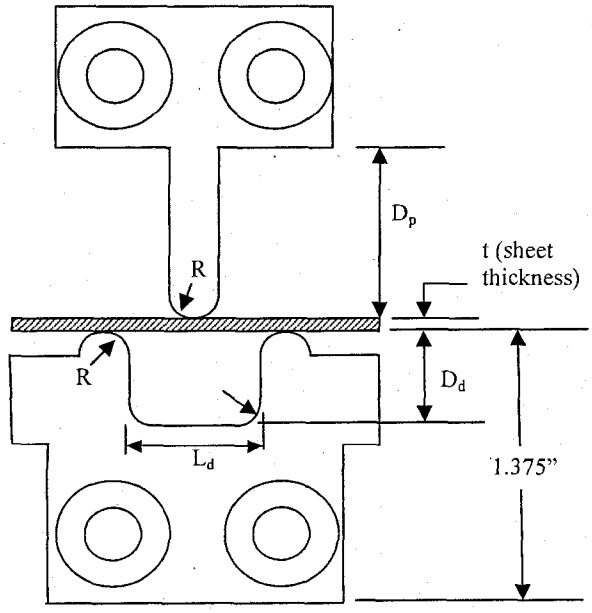

Figure 2.2 Schematic of microbending tooling.

The microbent sheets were fabricated from CuZn30 α-brass, which has a FCC structure. To investigate if a grain size effect on deformation exists, as received materials were heat treated at different temperatures to obtain the desired fine and coarse grain structures. The heat treatment temperatures and obtained grain sizes are given in Table 2.1 The heat treatments were conducted in a pure argon gas environment for one hour. The grain size measurements were performed on the sides of the sheets based on ASTM E112 standard [56]. For a given sheet thickness, coarser structures are obtained for higher treatment temperatures. However, since as-received conditions and the thickness of the sheets are not the same, different grain sizes were obtained for the same heat treatment temperatures for different specimen thicknesses.

Table 2.1 Heat treatment temperatures and the obtained grain sizes

0.25 mm		**0.5 mm**		**1.625 mm**	
Heat Treatment Temp. (°C)	Grain Size (μm)	Heat Treatment Temp. (°C)	Grain Size (μm)	Heat Treatment Temp. (°C)	Grain Size (μm)
500	20	550	22.5	515	19
650	130	700	205	665	175
800	190	800	285	715	280
				800	660

As shown in Table 2.1, a fine grained structure which has approximately a 20 μm grain size was obtained for each sheet thickness. This produces a different number of grains through the thickness, 12.5, 22.5 and 85.5 for the 0.25, 0.5 and 1.625 mm specimens respectively. The other structures are coarse structures, which have less than 10 grains through the thicknesses. Consistent grain sizes of approximately 190 μm and 280 μm exists for the different sheet thicknesses.

The microbending experiments were performed on a 4448N (1000 lb) SEM loading stage manufactured by Ernest F. Fullam Inc., NY with the corresponding tooling for the specimen size. The displacement of the punch was measured using a Linear Variable Differential Transducer (LVDT) while the force was measured using a load cell. The LVDT used is a Vishay Micro-Measurements Linear Displacement Sensor HS25 with a fully active 350-ohm strain gauge bridge to sense spindle displacement. The bending force was measured using a 111.2 N (25 Ib) Sensotec precision miniature load cell model 31 for the 0.25 and 0.5 mm cases and a 2224 N (500 Ib) load cell for the 1.625 mm thickness cases. Five tests were conducted for each thickness and heat treatment case and average plots were created. The stroke of the punch during the experiments was 7t.

Table 2.2 The initial hardness of the sheets prior to micobending

0.25 mm		**0.5 mm**		**1.625 mm**	
Grain Size (μm)	Hardness (HK)	Grain Size (μm)	Hardness (HK)	Grain Size (μm)	Hardness (HK)
20	83	22.5	79.5	19	94.5
130	77	205	77.5	175	73
190	71.5	285	77.5	280	76.5
				660	75

In order to investigate the effects of specimen size and grain size on deformation during microbending, microhardness evaluations were performed on the microbent sheets. First, the sheets were molded into epoxy and polished. Then, the microhardness measurements were obtained through the thickness of the microbent sheets at the bend area using a Knoop indenter on a Beuhler Microhardness Machine. Measurement were obtained with a 10 gram load and are spaced approximately, 50 μm apart for the 0.25 mm and 0.5 mm thick specimens and 75 μm apart for the 1.625 mm thick specimens. This

resulted in 7, 9 and 20 measurements through the thickness for the 0.25, 0.5, and 1.625 mm thick specimens respectively. As for the length along the sheet, the measurements were obtained every 0.11, 0.22, and 0.76 mm for the 0.25, 0.5, and 1.625 mm thick sheets respectively. Both halves of the 3-point bending specimens were measured and then averaged. Microhardness measurements of the undeformed material remote from the bending area were also obtained. Thus the change in the hardness due to bending could be determined. In Table 2.2, the average initial microhardness values of two sheets are given for each case (i.e. for each grain and specimen sizes).

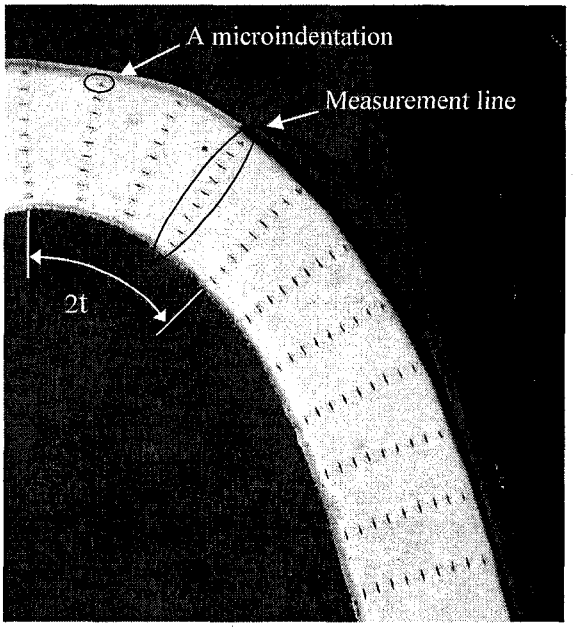

Figure 2.3 Microhardness measurements through the thickness on one arm of a 205 μm coarse grained 0.5 mm specimen

Results

During deformation, the metals strain hardens. As a result, their strength and hardness increase due to deformation (i.e., the higher the plastic deformation, the higher the hardness of the material after deformation). In forming operations such as bending where plastic strain gradients exit through the thickness of the workpiece, the

deformation distribution can be characterized by hardness evaluation through the cross section of the workpiece. In Fig. 2.3, half of a specimen after the microhardness evaluation is shown.

In Figs. 2.4, 2.5 and 2.6 the average contour plots of the increase in the hardness after microbending operations for half of the specimens are shown for all microbending cases. For each contour plot, the average initial hardness of the sheets was subtracted from the measured hardness values after deformation. Thus, the contour plots show the hardness increase of the sheets after microbending. To construct each contour plot two microbent sheets were measured and averaged. Also, because three point bending is a symmetrical process, the hardness values of the two halves of the specimens were averaged and data for only one half of the specimen is provided in the contour plots. Thus, each contour plot is the average of four halves of two sheet specimens. In the figures, the negative locations through the thickness of the sheets correspond to the compression side of the bend and positive locations correspond to the tension side while the zero location corresponds to the center of the specimen.

From Figs. 2.4a, 2.5a and 2.6a, it can be seen that the hardness contour plots of the fine grained sheets have a smooth and consistent layered pattern through the thickness and along the length of the specimens which is consistent with conventional macroscale bending. The hardness is lowest at the neutral axis in the center of the specimen. Considering the location along the specimen length, as the location along the length of the specimen increases the hardness values gradually decreases, which means maximum bending occurs at the punch tip location.

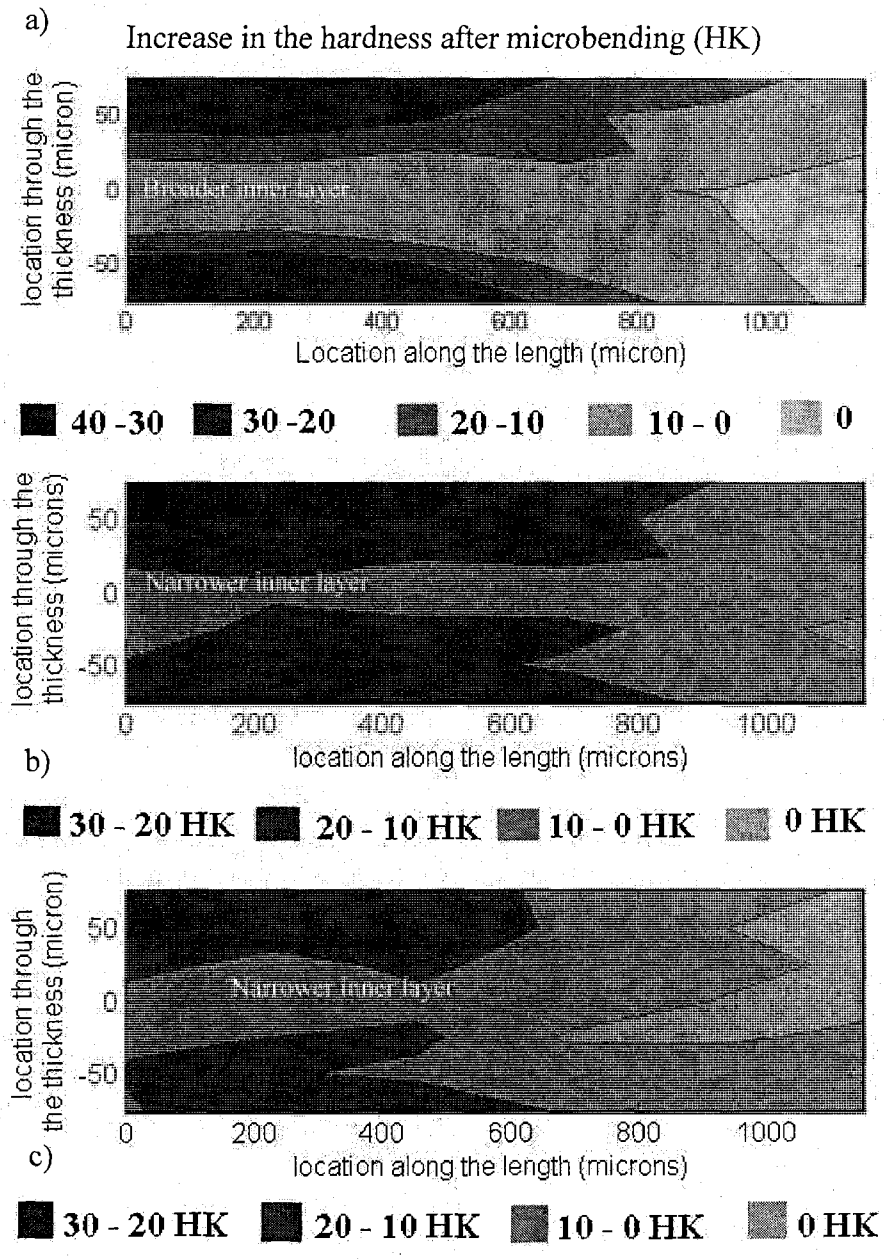

Figure 2.4 Average contour plots of increase in the hardness after microbending operations on one arm of the 0.5 mm thick a) 20 μm fine grained b) 130 μm coarse grained c) 190 μm coarse grained sheets.

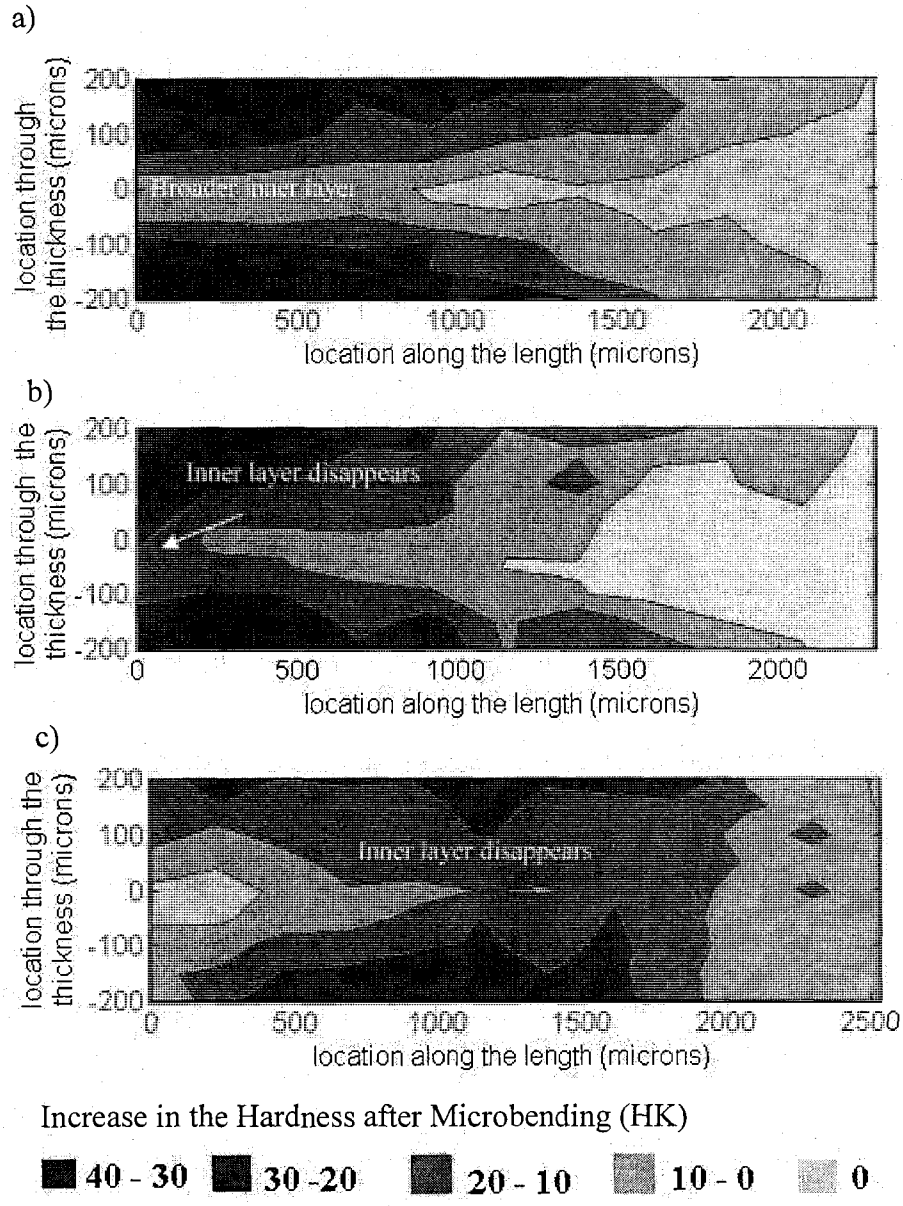

Figure 2.5 Average contour plots of increase in the hardness after microbending operations on one arm of the 0.5 mm thick a) 22.5 μm fine grained b) 205 μm coarse grained c) 285 μm coarse grained sheets.

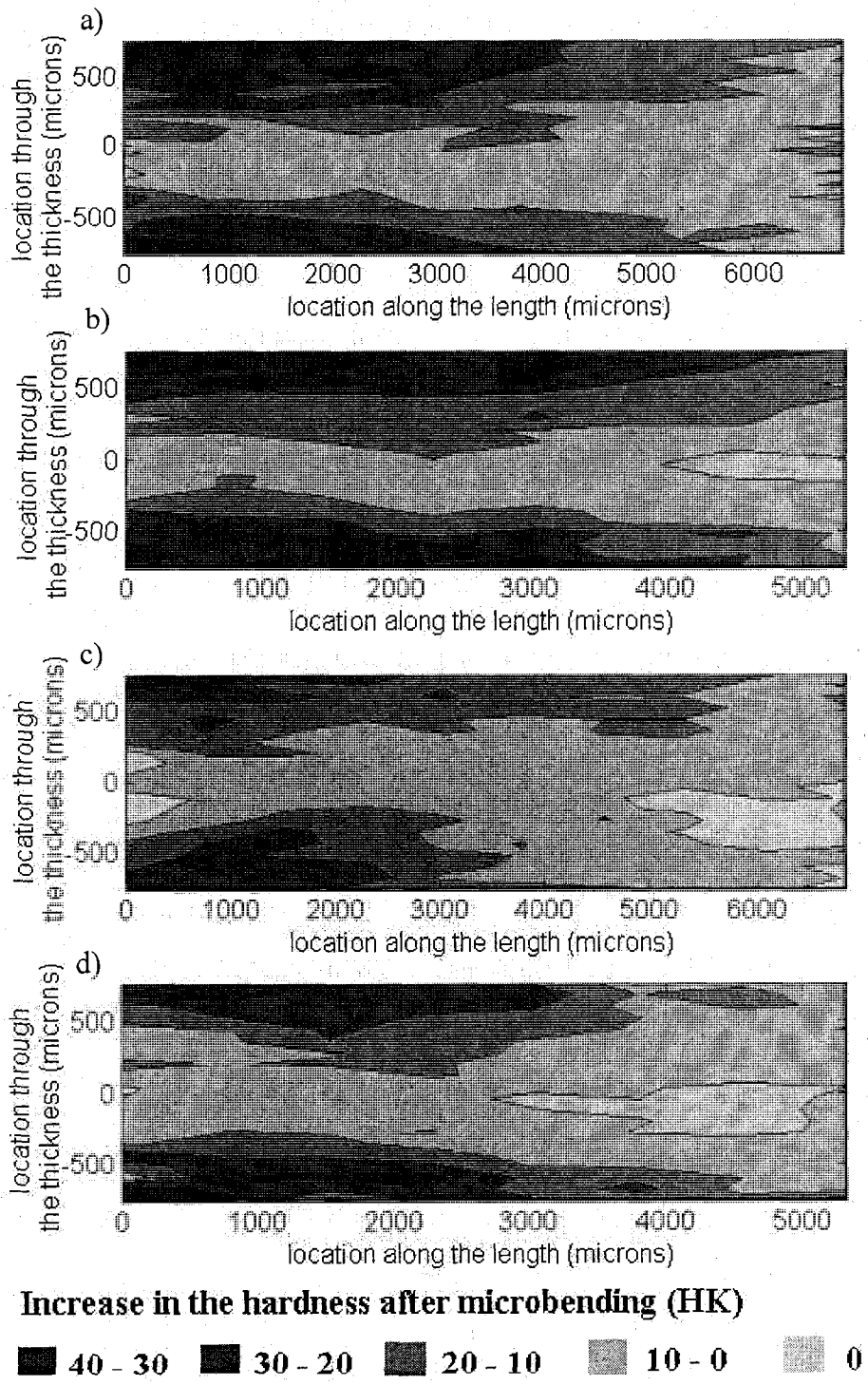

Figure 2.6 Average hardness contour plots on one arm of the 1.5 mm thick a) 19 μm fine grained b) 175 μm coarse grained c) 280 μm coarse grained d) 660 μm coarse grained sheets.

The contour plots of the coarse grained specimens are more scattered and less consistent through the thickness and along the length of the sheets and the layer structure is disturbed. Interestingly, in one of the 285 μm grained 0.5 mm specimens, the location along the length of the sheet where the highest hardness increase occurs is not at the zero location where the tip of the punch contacts the specimen. At this location penetration of deformation to the inner regions is observed. A possible cause of this is that the coarse grains at the area where the tip of the punch contacts the sheet specimen are not favorably oriented for the bending deformation. Figure 2.7 shows the microstructure of this microbent coarse grained specimen. This effect was so pronounced in this specimen that the behavior can be seen in the average contour plot of the 0.5 mm thick 285 μm grain size sheets, i.e. Fig 2.5 c).

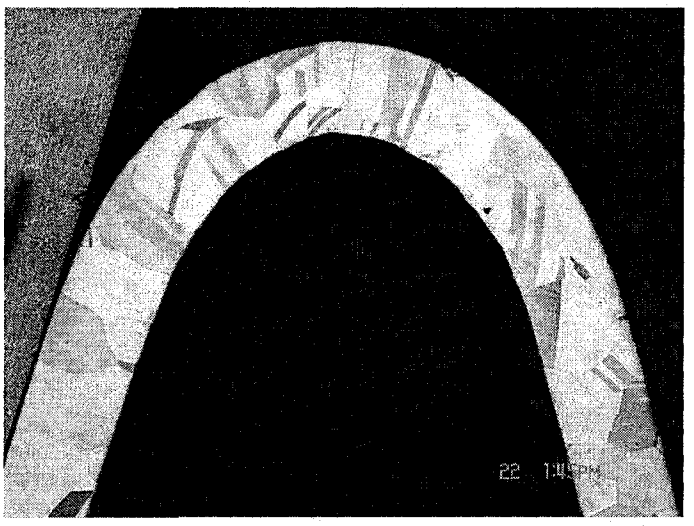

Figure 2.7 Microstructure of a 0.5 mm thick, 285 μm coarse grained microbent specimen

In addition, for the two smallest sizes, i.e., the 0.25 mm and 0.5 mm sheet specimens, at the bend area it seems that the lower hardness increase layer around the neutral axis is broader for the fine grained structure whereas this layer is narrower or non-existent for the coarse grained structures. Thus, some penetration of plastic deformation from the highly strained surface regions to the inner regions seems to occur. For the

largest size, 1.625 mm thick specimens, the inner layers of low hardness increase are similarly broader for the fine and the coarse grain structures. Note that the layered structure in Fig. 2.6 is less consistent compared to Figs. 2.4 and 2.5 as more data points through the cross-section were obtained.

To investigate the effect of grain size and the specimen size on deformation during microbending more thoroughly, the average hardness increase profile through the thickness of the specimens is plotted in Fig. 2.8 for the 1.625 mm, 0.5 mm and 0.25 mm specimens. Each plot is an average hardness increase distribution of two specimens in the bend area (i.e., the average hardness of the measurement lines (see Fig. 3) in a 4t region around where the punch tip contacts the specimen). In these plots the zero location again corresponds to the center of the thickness while the negative and positive values correspond to compression and tension sides respectively. The plots in Fig. 2.8 show the increase in the hardness of sheets through the thickness after microbending experiments.

In Fig. 2.8 a) the average hardness increase profiles through the thickness of 1.625 mm specimens at the bend area is given for all grain sizes. All the grain structures, i.e., the fine 19 μm grained and the coarse 170 μm, 280 μm and 660 μm grained structures, have similar hardness increase profiles through the thickness after microbending. High hardness increase values exist near the surface region (280 μm and 660 μm grained specimens have 10–5 HK lower hardness increase values at the surface region comparing to 19 μm and 170 μm specimens), which decrease sharply to the inner regions. Also, similar minimum hardness increase values near the neutral axis occur. The difference in the hardness between the surface regions and the neutral axis is 35-25 HK for all grain sizes. All of the different grained sheets underwent the same scaled microbending

processes and it seems that the hardness increase profile or deformation distribution through the thickness is not affected significantly by the grain size for the largest, 1.625 mm thick specimens.

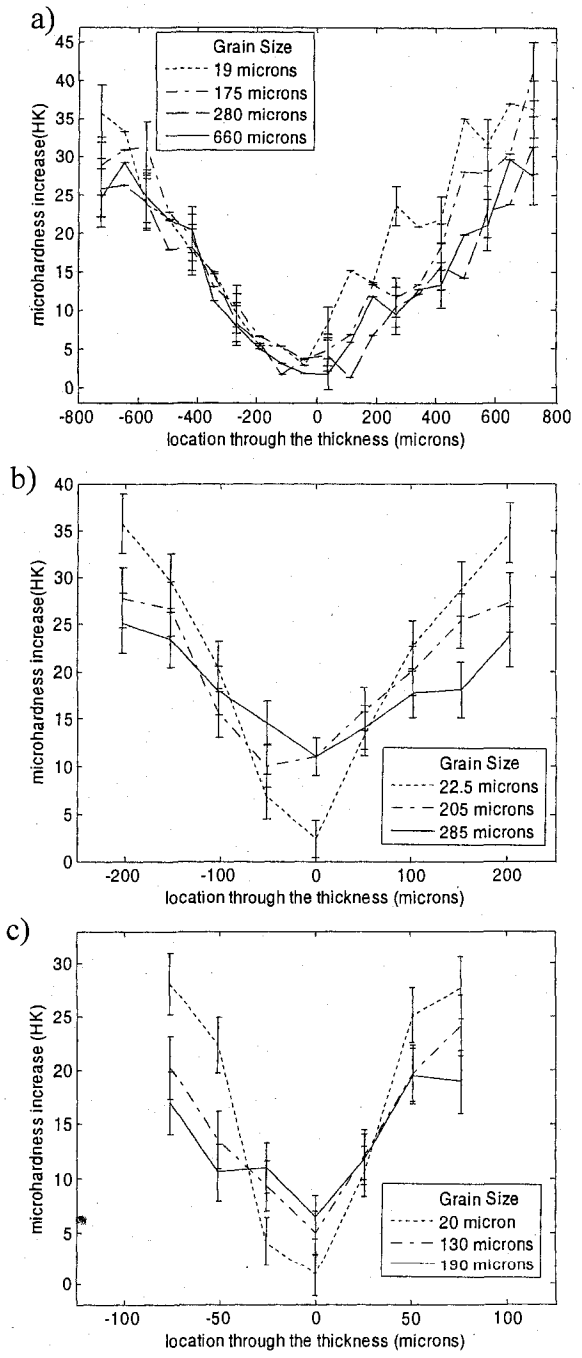

Figure 2.8 Average hardness profile at the bend area through the thickness of a) 1.625 mm b) 0.5 mm c) 0.25 mm sheets. Note: initial hardness values were subtracted from measured hardness values after bending.

In Fig. 2.8 b), the average hardness increase profiles through the thickness of 0.5 mm specimens at the bend area is given for all grain sizes. The hardness increase profile through the thickness of the coarse grained structures deviates from the fine grained one although they underwent the same scaled microbending process. The hardness increase profile of the 20 μm fine grain size structures is similar to the ones obtained for the largest size 1.625 mm specimens that are presented in Fig. 2.8 a). The increase in the hardness is highest, 35 HK near the surface region and decrease sharply to the inner regions. The increase in the hardness is minimum, almost zero, at the neutral axis.

The coarse grained, 200 μm and 280 μm grain size specimens also have higher hardness increase values at the surface region and minimum near the neutral axis. However, the distribution of the hardness through the thickness is quite different. They have relatively lower hardness increase values at the surface than fine grained specimens and these values decrease more gradually from the surface to the inner regions. As a result higher hardness increase values occur at the inner regions. The difference in the hardness increase values between the surface region and the neutral axis is about 33 HK for the 20 μm, fine grained sheets compared to 18 HK and 13 HK for the 200 μm and 280 μm coarse grained sheets, respectively.

In Fig. 2.8 c), the average hardness profiles through the thickness of the smallest size, 0.25 mm specimens at the bend area is given for all grain sizes. Similar to the 0.5 mm specimens, the hardness increase profile through the thickness of the coarse grained structures deviates from the fine grained ones although they underwent the same scaled microbending processes. Again, the hardness profile of the 20 μm fine grain size structures is similar to the ones obtained for the largest 1.625 mm specimens that are

presented in Fig. 2. 8a). The hardness increase values are high near the surface region and decrease sharply to the inner regions. The hardness increase values are minimum, almost zero at the neutral axis.

The distribution of the hardness through the thickness is again quite different for the coarse grained, 130 μm and 200 μm grain size specimens. The coarse grained specimens have relatively lower hardness increases at the surface than fine grained ones and the hardness decreases more gradually from surface to inner regions. As a result the coarse grained sheets have higher hardness increase values at the inner regions. The difference in the hardness between the surface region and the neutral axis is about 26 HK for the 20 μm, fine grained specimens compared to 19 HK for the 130 μm coarse grained specimens and 13 HK for the coarse 200 μm grained specimens.

In order to compare the deformation of the coarse and fine grained specimens for the different thicknesses, the locations through the thickness were normalized by dividing by half of the specimen's thickness. Then, the hardness increase profiles for the three different specimen sizes were plotted together for a given grain size, see Fig. 2.9 The first microindentations were taken 50μm away from the surface for all specimen sizes, thus in these plots the hardness curves do not start at the same normalized location at the surface region. Also to plot these curves, the 20 μm, 22.5 μm and 19 μm grain size structures for the 0.25mm, 0.5 mm and 1.625 mm specimens, respectively, are grouped as fine 20 μm grain size structures. Similarly, the 190 μm, 205 μm and the 175 μm grain size structures, for the 0.25mm, 0.5 mm and 1.625 mm specimens respectively, are grouped as coarse 190 μm grain size structures. Finally, the 285 μm grain size 0.5 mm specimens and 280 μm grain size 1.625 mm specimens are grouped as coarse 280 μm grain size structures.

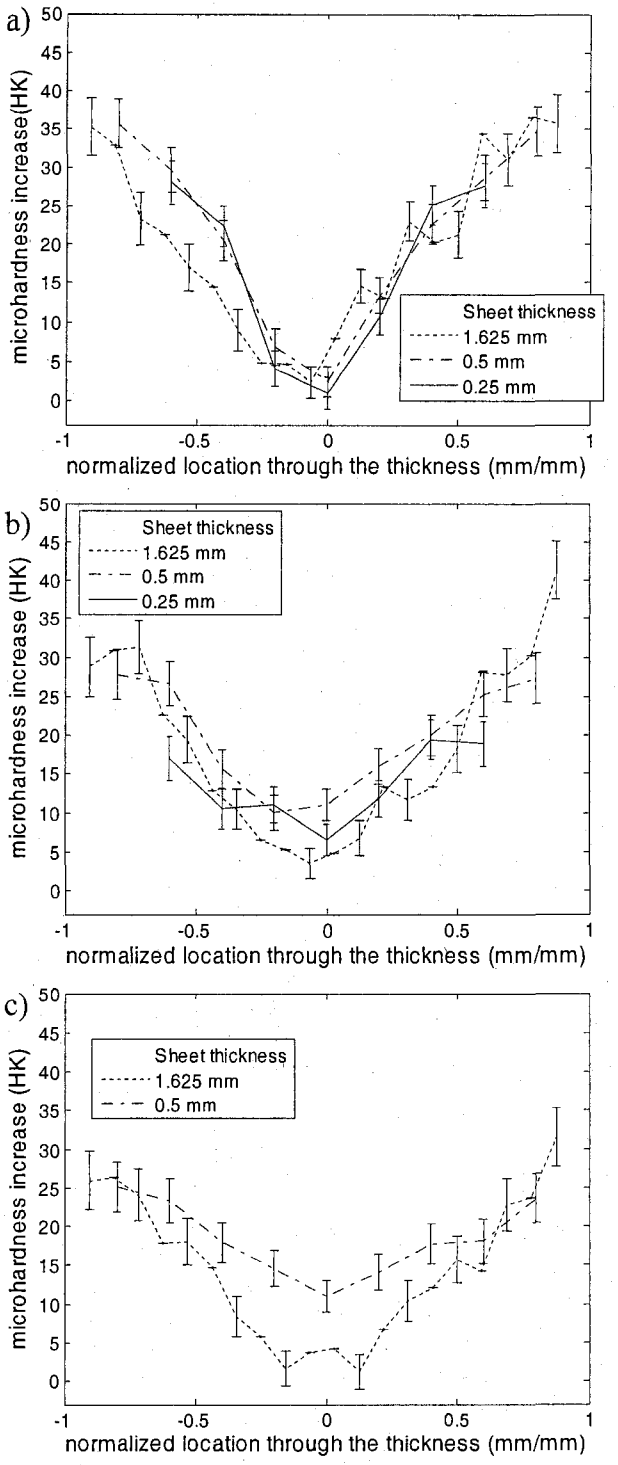

Figure 2.9 The average hardness distribution at the bend area through the thickness of a) 20 μm b) 190 μm c) 280 μm grained sheets. Note: initial hardness values were subtracted from measured hardness values after bending.

In Fig. 2.9a) the hardness increase profiles of the 20 μm fine grained sheets for the three different specimen sizes are plotted. The deformation distribution through the thickness is not affected significantly by miniaturization for the fine grained specimens. For all specimen sizes, the hardness increase profiles are quite similar in particular on the tension side of the neutral axis, i.e. positive normalized location values. Additionally, similar minimum hardness increase values at the neutral axis and higher values near the surface region were obtained. Note that the values for the 1.625 mm specimens deviate on the compression side, compared to the two smaller size, 0.5 and 0.25 mm thick specimens.

In Fig. 2.9b), the hardness increase profiles of the 190 μm coarse grained sheets for the three different specimen sizes are given. For the largest size, 1.625 mm specimens, the change in the hardness is steeper from the surface region to the inner region where as for the two smaller size specimens the hardness decreases more gradually. As a result the two miniaturized smaller size specimens have higher hardness near the neutral axis. Similarly in Fig. 2.9c) for the 280 μm coarse grained structures, the change in the hardness is steeper from the surface region to the inner region for the largest size 1.625 mm specimens where as for the smaller 0.5 mm thick specimens the hardness decreases more gradually. As a result, the 0.5 mm specimens have higher hardness near the neutral axis. This shows the penetration of the plastic deformation to the inner regions during microbending of the coarse grained sheets as a result of miniaturization.

Discussion

From these results it can be concluded that the deformation distribution through the thickness is affected by the grain size when the specimen dimensions are miniaturized. By scaling the process by the law of similarities, a strain of 22% should theoretically be achieved on the outer surfaces for all of our cases regardless of thickness (with zero strain at the neutral axis). As the specimen size decreases, this change in the strain occurs over a shorter distance; thus, the gradients imposed by the deformation geometry become steeper. During deformation, coarse grains in a steep strain gradient field tend to more evenly distribute the deformation. As a result, for the coarse grained structures, the penetration of plastic deformation from the surface regions to the inner region occurs during bending and more plastic deformation, i.e., higher hardness at the inner regions occurs when the dimensions are miniaturized. Also, less deformation (i.e., lower hardness increase) at the surface region occurs, as well. These effects are evident when comparing the smaller 0.25 mm and 0.5 mm coarse grained specimens to the fine grained one and to the 1.625 mm specimens (with both fine and coarse grains). For the fine grained sheet specimens, miniaturization of the sheet thickness does not seem to have a significant effect on the hardness distribution, i.e., plastic deformation distribution, as the hardness increase profile through the thickness for all sizes are quite similar; see Fig 2.9 a).

From these results and past microextrusion results, it is seen that when strain gradients become steep due to miniaturization, the distribution of the strain is affected by the grain size. This behavior can be related to the grain boundaries which are dislocation barriers. During microbending, the grain boundaries of fine structures inhibit the

dislocation motion and do not allow them to penetrate from highly strained surface regions to less strained inner regions. When there exists only a few grains in the strain gradient field, there are fewer grain boundaries and thus dislocations penetrate to the less strained inner regions. In addition, because there are less grain boundaries at the surface regions, less dislocation pile-ups occur and less geometrically necessary dislocations are generated at the grain boundaries due to compatibility of displacements between adjacent grains [25]. As a result, less strain hardening occurs at the highly strained surface region for the coarse structure, as well. For microextrusion, due to the friction that is generated between workpiece and die surface, the coarse grained pins have high hardness values at the surface and thus these values are comparable to the fine grained structure.

While performing the microbending experiments, the force and displacement curves were also recorded. In order to compare the curves of sheets with different thicknesses for a given grain size, the bending force and punch displacement values were normalized with respect to the sheet thickness. For the punch displacement, values were divided by the sheet thickness, since the punch displacement was a scalar of the sheet thickness (7t). Similarly, the bending force value was divided by the sheet thickness squared since bending force is a function of the sheet thickness squared [57]:

$$P = \frac{cwt^2\sigma_y}{L} \tag{2.1}$$

Where P is the maximum bending force, w is the width of the sheet, t is the sheet thickness, L is the die opening clearance, σ_y is the yield strength of the material and c is a constant that varies from 0.3 for a wiping die, 0.7 for a U-die to approximately 1.3 for a V-die.

In Fig. 2.10, normalized bending force versus displacement curves are given for 20 μm, 190 μm and 280 μm grained sheets. In Fig. 2.11, the normalized peak bending force versus specimen size curves for the three grain sizes are given. For the 20 μm fine grained sheets, the normalized peak force values increase slightly as specimen size decreases, see Fig. 2.10 a). There is also a slight increase in the peak force as the sheet thickness is miniaturized to 0. 5 mm from 1.625 mm for the 190 μm coarse grained sheets. Miniaturization from 1.625 to 0.5 mm increases the share of surface grains in the total volume significantly for the 190 μm grain size sheets and the peak force results seems to contradict the surface layer model [2,3] which states that the peak forces should decrease with a decrease in sheet thickness as the share of the surface grains increase. The penetration of shear which occurs due to the miniaturization can be the cause. As seen from hardness distribution through the thickness, Fig. 2.9 b) penetration of deformation occurs for the coarse 190 μm grained, 0.5 mm sheets. This, additional deformations can be responsible for the increase in the peak forces which appears with miniaturization. However, the peak force decreases for the smallest sized, 0. 25 mm thick, 190 μm coarse grained sheets. Also, for the 280 μm grained sheets the peak force of 0.5 mm sheets are lower than the 1.625 mm sheets. For these sizes (i.e., 190 μm grained 0.25 mm specimens and 280 μm grained 0.5 mm specimens), the sheet material consists of primarily surface grains and have relatively lower hardness values at the surface regions. This possibly is the reason for the lower peak force values of the smallest sized, 0. 25 mm thick, 190 μm coarse grained and 0.5 mm thick, 280 μm coarse grained sheets. It should also be noted that not all research has agrees with the surface layer model. Cao et al. [37] did not observe a decrease in the yield strength of cylindrical

CuZn30 tensile test specimens with miniaturization as predicted by the surface layer model.

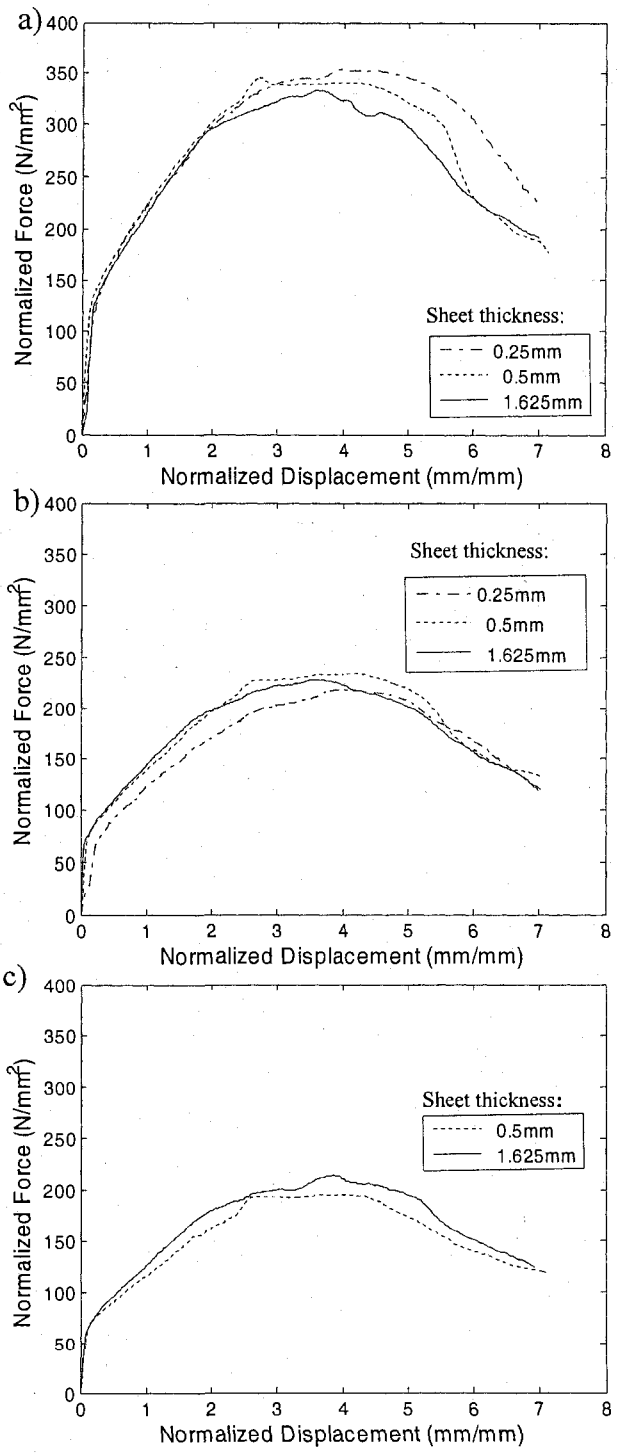

Figure 2.10 Normalized bending force versus displacement curves for a) 20 μm and b) 190 μm c) 280 μm grain sized sheets.

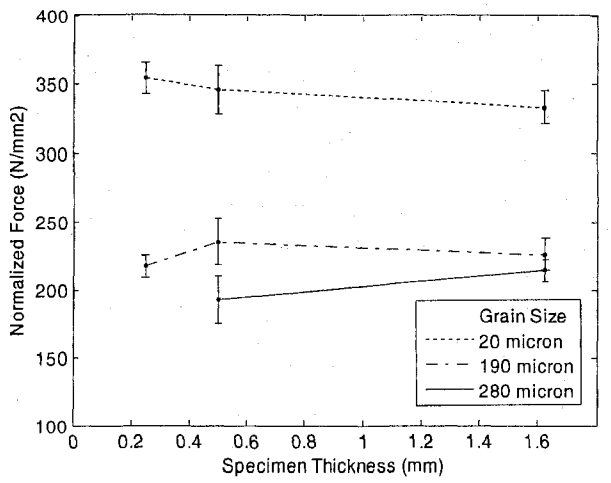

Figure 2.11 Normalized peak bending force versus specimen size curves for 20 μm, 190 μm and 280 μm grained sheets.

Estimating the springback amount is critical for the sheet metal forming industry. Springback is closely related to the deformation distribution through the cross section at the bend area. Although the springback angle has not been studied in this paper, understanding the influence of grain and specimen size on deformation distribution through the thickness of the microbent sheets is important to understand the springback behavior of miniaturized sheets. This is true as, the

Conclusion of This Chapter

In this chapter, the dependence of deformation in microbending on specimen size and grain size was investigated via microhardness evaluations. It was found that the deformation distribution, i.e., the hardness increase values through the thickness is affected by the grain size when the specimen size is miniaturized. For the largest size 1.625 mm thick specimens, the hardness increase profiles are similar for the fine and coarse grained sheets. However, for the miniaturized, 0.5 mm and 0.25 mm thick specimens, the hardness increase profiles of the coarse grained structures decrease more

gradually from the surface to inner regions. As a result after microbending, the increase in the hardness of the inner regions is higher for the coarse grained sheets. This is an indication of penetration of plastic deformation to the inner regions during microbending of the coarse grained structures. For the fine grain structure, miniaturization of the specimen size does not seem to have a significant effect on the hardness increase profiles, i.e., plastic deformation distribution through the thickness of the sheets.

CHAPTER 3

MICROTENSILE TESTS

Background

In the first two chapters, the deformation distribution, i.e., the hardness distribution through the diameter and the thickness of microextruded and microbent specimens, were investigated. In these forming processes, strain gradients are present through the specimens which become steeper with miniaturization. The microhardness evaluations revealed that with miniaturization the coarse grained structures have higher hardness in the central region compared to the fine grained ones due to penetration of deformation. In this chapter, for comparison, the microhardness evaluations were presented for microtensile tested specimens where no significant strain gradients are present during deformation.

Results

The microtensile test specimens were made of CuZn30. Microhardness measurements on two 32 μm and two 211 μm grain size tensile test specimens which fractured at approximately 30% strain were obtained (The structures are similar to the structures used in chapter 1). The tensile specimens had a diameter of 0.8 mm and were tested at room temperature, using a Sintech universal testing machine with a 2500 N capacity load cell at Northwestern University.

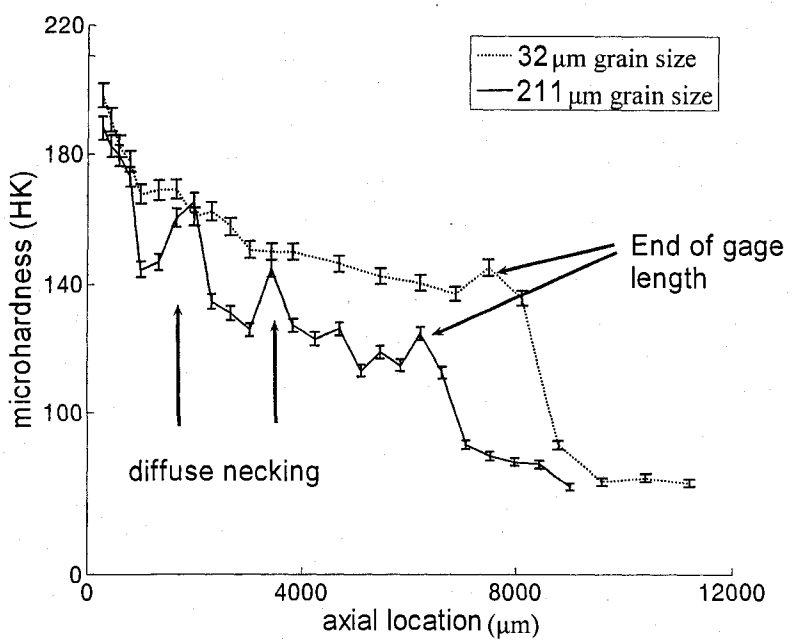

Figure 3.1 Hardness distributions along the gage length of the tensile specimens.

Fractured pieces of the specimens from the tests were molded and ground to their half cross section. The hardness values were relatively consistent at a given axial location; thus, they were averaged to obtain a single hardness value. See Fig. 3.1 for a plot of the hardness values versus axial location for the 32 μm and 211 μm grain size tensile test specimens. In this figure, the zero axial location corresponds to the fracture location of the tensile specimen. The hardness values for the 32 μm, fine-grained specimens have slightly higher hardness values than the 211 μm, coarse-grained specimen at the zero axial location where necking and the maximum hardness values for the specimens occur. The hardness values then decrease gradually through the gage length, decrease significantly to its minimum annealing hardness value at the end of the gage length and remain relatively constant through the grip section. As expected and consistent with the Hall-Petch relationship and the tensile data which is given in Fig. 3.2,

the 211 μm, coarse-grained tensile specimen has lower hardness values than the 32 μm grain size one.

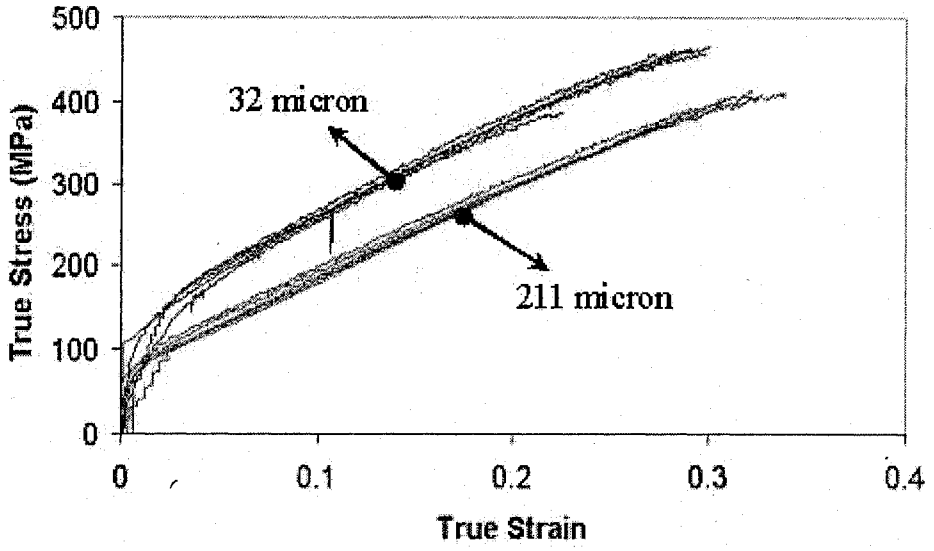

Figure 3.2 Tensile test curves of 32 μm and 211 μm grain size specimens.

Beside this expected result, one can also observe from the data in Fig. 3.1 that the hardness values of the coarse-grained specimen fluctuate through the gage length, while maintaining a decreasing trend, whereas hardness values for the fine-grained specimen do not experience such a fluctuating phenomenon. (See the diffuse necking locations labeled in Fig. 3.1) This is because the coarse-grained specimen has only a few grains through the cross-section. Thus, the deformation of individual grains is not as constrained by neighboring grains as in polycrystalline tensile deformation. At these diffuse necking axial locations, one of the grains or a few grains probably are oriented more favorably for tensile deformation and thus stretch or deform more than the grains in other cross-sectional locations through the gage length. The hardness values at these axial locations are higher due to the increased stretching. The half cross section photos of the tensile specimens in Fig. 3.3 support this explanation. The hardness values at the 1750 μm axial location (the 7th hardness measurement line) and the 3500 μm axial location (the 12th

hardness measurement line) were higher for the 211 μm grain size specimen (Fig. 3.1) and diffuse necking deformation can be observed at these locations (Fig. 3.3a). This type of anomalous stretching and fluctuating hardness values were not observed in fine-grained tensile specimens, which have a consistently decreasing hardness curve along the gage length (see Fig. 3.1) and a straight surface (see Fig. 3.3b).

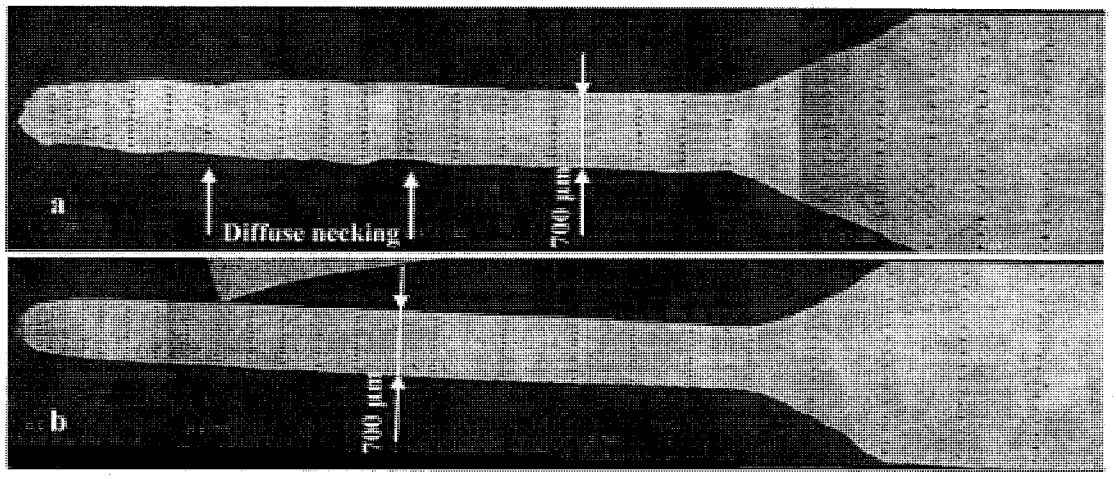

Figure 3.3 Half cross section of tensile specimen pieces a) 211 μm grain size b)32 μm grain size.

Conclusion of This Chapter

From the hardness evaluations performed on microtensile tested coarse and fine grained specimens, it is found that the coarse grained specimens have lower hardness than the fine grained specimens through the cross section when no significant strain gradient is present during deformation.

CHAPTER 4

INVESTIGATION OF STRAIN GRADIENT HARDENING

Background

It has been shown that the hardening of crystalline materials at the microscale is significantly affected by the gradients of the deformation. As previously mentioned, in his pioneering paper in 1970 on inhomogeneous deformation, Ashby introduced the distinction between the statistically stored dislocations, SSDs, and geometrically necessary dislocations, GNDs [26]. While the former are stored generally during homogeneous deformation, the latter are stored due to the plastic shear strain gradients during inhomogeneous deformation. The density of SSDs is associated with the amount of plastic strain whereas the density of GNDs is directly proportional to the gradients of plastic strain. The density of GND, ρ_{GND}, can be calculated according to plastic shear strain gradients, $\chi = d\gamma_{pl}/dy$. In the simplest one dimensional case for single slip with a Burgers vector b in the y-direction [26, 58]:

$$\rho_{GND} = \frac{1}{b} \left(\frac{d\gamma_{pl}}{dy} \right) = \frac{\chi}{b} \tag{4.1}$$

According to Ashby, the GNDs contribute to the strain hardening of materials and he proposed a Taylor-type relation to estimate their contribution on strain hardening:

$$\tau = cGb\sqrt{\rho_{SSD} + \rho_{GND}} \tag{4.2}$$

where G is the shear modulus and c is a numerical factor, typically on the order of c ≈ 0.2-0.4 and ρ_{SSD} is the density of statistically stored dislocations.

The contribution of GNDs has been used to explain the increased strain hardening of very small metallic specimens when they undergo inhomogeneous deformation, such as in the torsion of thin wires [21], bending of thin sheets [23] and in nanoindentation [22].

In Fig. 4.1. the dependence of bending strength on size is shown for microbending [23]. During bending, strain gradients are generated through the thickness. When the specimen thickness size is scaled down to the order of tens of microns, the strain gradients become steeper. As a result the density of GNDs and strength of the material increase significantly.

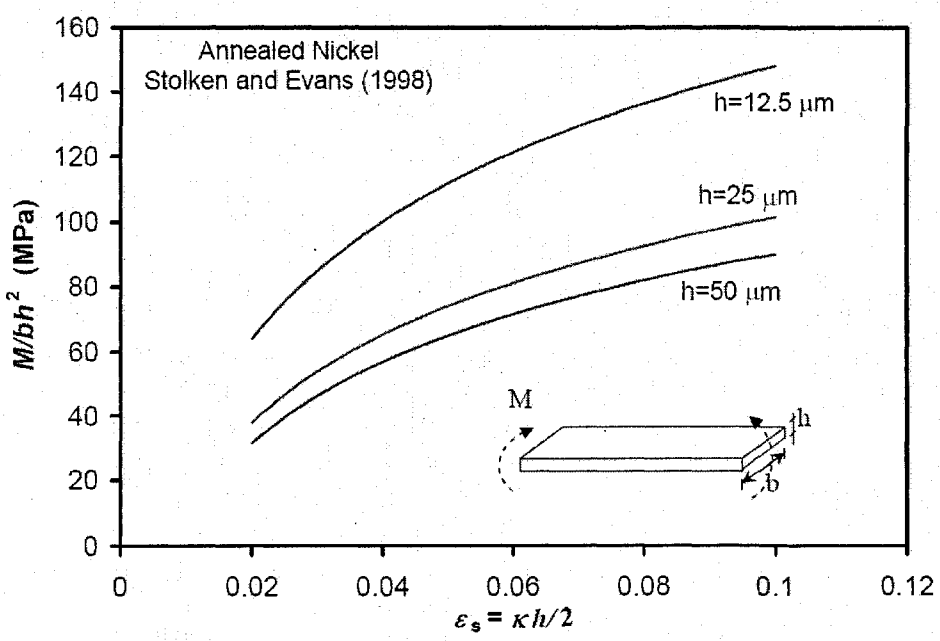

Figure 4.1 Dependence of strength on specimen size in microbending of thin Nickel films [23].

The strain gradient hardening becomes significant when the specimen feature size is on the order of tens of microns. The goal of this chapter is to predict the strain gradient hardening amount for the specimen sizes used in the thesis (which are on the order of 400

μm or more). To achieve this, an analytical model is established to determine strain gradient hardening of metals during axisymmetric forward microextrusion. First, a formulation is generated to estimate the strain distribution through the thickness during axissymmetric forward extrusion. By also using shear components of the formulation, a new model is established to estimate the GND density. In Fig. 4.2 the flow chart of the calculations of the predicted GND density is shown. Then, using a Taylor type equation as proposed by Ashby, the strain gradient hardening, SGH, during microextrusion is estimated. It is found that the GND density increases with a decrease in the initial and final specimen radii and an increase in the die angle, α. Also, it is shown that, for the smallest size, Ø0.76/0.57 mm pins, a 3.6 % increase in the strength at the axis of symmetry is predicted, while a 1.2% and 0.9% increase in the strength is predicted for Ø1.5/1.0 mm and Ø2.0/1.33 mm pins respectively at the axis of symmetry due to strain gradient hardening [59]. In Figure

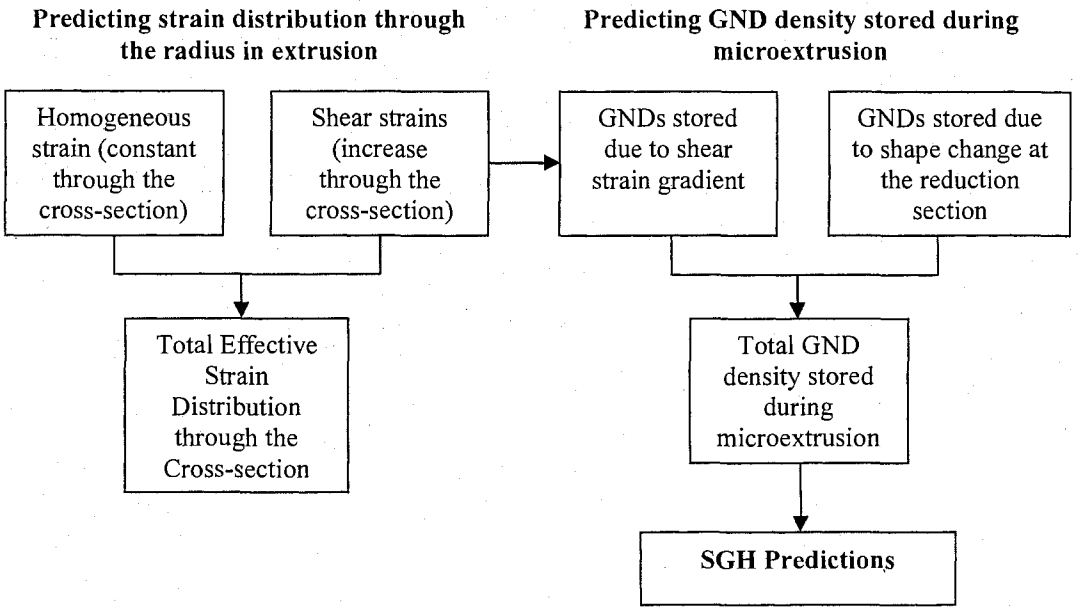

Figure 4.2 Flow chart of the calculation of predicted GND density that is stored during microextrusion

Analytical Model

Strain Distribution Through the Diameter of an Extruded Workpiece

In extrusion when a material enters the reduction section, the flow direction changes throughout the cross-section toward the apex of the die. See Fig. 4.3 for a schematic of this assumed material flow. Along a flow line, the angular position of the material does not change, but the radial distance from the axis of symmetry decreases in the reduction section [29].

The deformation that is experienced by the material during this assumed material flow can be separated into two distinct deformation modes:

1. Homogeneous deformation due to the area reduction
2. Shear deformation which occurs at the shear discontinuity planes, P_A and P_B

The total strain is the sum of these two deformation modes. For simplicity, the shear discontinuity is assumed to occur at the straight planes, P_A and P_B, rather than arced surfaces as proposed by Avitzur [29].

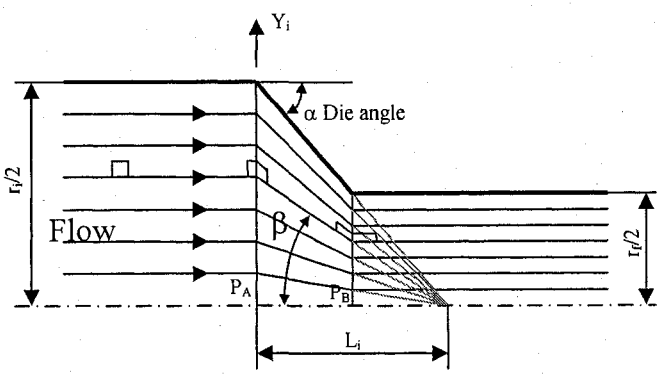

Figure 4.3 Assumed material flow during extrusion

The effective strain due to homogeneous deformation experienced between planes P_A and P_B due to the area reduction is:

$$\varepsilon_h = \ln \frac{r_i^2}{r_f^2} \tag{4.3}$$

where r_i and r_f are the initial and the final radii respectively. This strain value is simply the strain if the material experienced a reduction in the area.

The shear strain that is experienced by an infinitestimal rectangular element that is distorted by an angle β is:

$$\gamma = \tan\beta \tag{4.4}$$

In extrusion, the shear strain that is experienced by an infinitestimal element at shear discontinuity plane P_A that is a distance Y_i away from the axis of symmetry on P_A is:

$$\tan\beta = \frac{Y_i}{L_i} \tag{4.5}$$

where L_i is the distance from the shear discontinuity plane P_A to the apex of the die angle at the axis of symmetry. Also, from the process geometry:

$$\tan\alpha = \frac{r_i}{L_i} \tag{4.6}$$

where α is the die angle. Combining Eqs. (5) and (6) into Eq. (4) provides the shear strain that is experienced by an element at P_A as:

$$\gamma_1 = \frac{Y_i}{r_i}\tan\alpha \tag{4.7}$$

where α is the die angle. Similarly, the shear strain that is experienced by an element at discontinuity plane P_B is:

$$\gamma_2 = \frac{\sqrt{R}\,Y_i}{r_f}\tan\alpha \tag{4.8}$$

where R is the reduction ratio, $R=r_f^2/r_i^2$ and thus γ_B is equal to γ_A:

$$\gamma_2 = \frac{Y_i}{r_i} \tan\alpha \tag{4.9}$$

The total shear strain that is experienced by an infinitesimal element at the shear discontinuity planes A and B which is a distance Y_i away from the axis of symmetry on P_A is:

$$\gamma_T = \frac{2Y_i}{r_i} \tan\alpha \tag{4.10}$$

The effective strain due to shear can be calculated based on von Mises yield criterion as:

$$\varepsilon_s = \frac{\gamma}{\sqrt{3}} \tag{4.11}$$

So the effective strain that is experienced by an infinitestimal element due to shear is:

$$\varepsilon_s = \frac{2}{\sqrt{3}} \frac{Y_i}{r_i} \tan\alpha \tag{4.12}$$

Thus, during axisymmetric microextrusion, the total effective strain that is experienced by an element at a distance Y_i from the axis of symmetry on P_A is:

$$\varepsilon_T = 2(\ln\frac{r_i}{r_f} + \frac{1}{\sqrt{3}} \frac{Y_i}{r_i} \tan\alpha) \tag{4.13}$$

A similar equation can be written according to the final radius of the workpiece as well:

$$\varepsilon_T = 2(\ln\frac{r_i}{r_f} + \frac{1}{\sqrt{3}} \frac{Y_f}{r_f} \tan\alpha) \tag{4.14}$$

Similarly, the total effective strain according to angular position of the element can also be calculated as:

$$\varepsilon_T = 2(\ln\frac{r_i}{r_f} + \frac{1}{\sqrt{3}} \tan\beta) \tag{4.15}$$

which is consistent with the formula by Talbert and Avitzur [60].

In Fig. 4.4 the total strain distribution through the normalized diameter of the larger size Ø1.5/1.0 mm and Ø2.0/1.33 mm pins which have R=2.25 and submillimeter size Ø0.76/0.57 mm pins which have R=1.77 are shown. The die angle is 30°. The shear strain component is zero at the axis of symmetry and increases gradually with a maximum at the surface. The submillimeter size, Ø0.76/0.57 mm pins have a homogeneous strain of approximately 0.575 mm/mm and the total strain at the surface is 1.1. The larger size pins have a homogeneous strain of approximately 0.81 and the total strain at the surface is 1.477. Note that the effect of friction is excluded in these analyses.

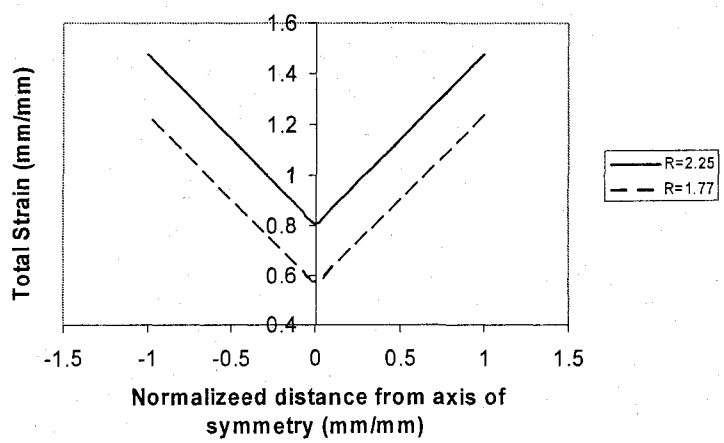

Figure 4.4 Predicted strain distribution through the normalized diameter of the larger size Ø1.5/1.0 mm and Ø2.0/1.33 mm pins which have an extrusion ratio R=2.25 and submillimeter size Ø0.76/0.57 mm pins which have R=1.77.

As it is mentioned before, during deformation, metals strain harden. As a result, their strength and hardness increase after deformation (i.e., the higher the plastic deformation, the higher the hardness of the material after deformation). In metal forming operations such as microextrusion where plastic strain gradients exit through the diameter of the workpiece, the deformation distribution can be characterized by a hardness evaluation through the cross section of the workpiece. However, it is acknowledged that characterizing the deformation via hardness evaluation is an indirect method and one can

not obtain the actual strain amounts. In addition, as the strain increases, the change in the hardness saturates. In Fig. 4.5, the correlation between the hardness of cold rolled CuZn30 brass and strain amount is shown (data obtained from [39]).

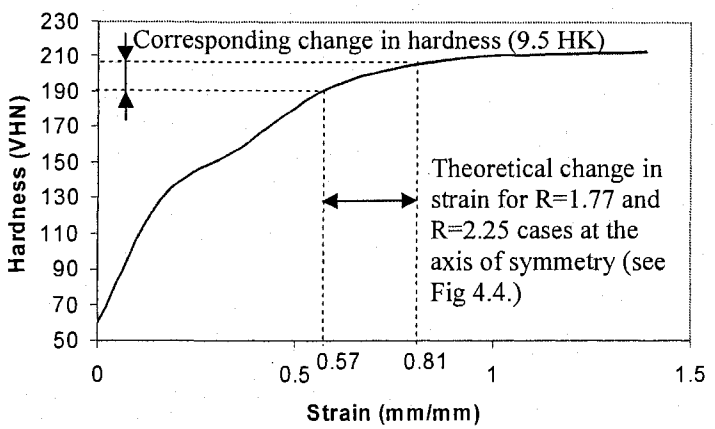

Figure 4.5 Correlation between the hardness of cold rolled CuZn30 and strain (data taken from [39])

In Chapter 1 the hardness distributions through the diameters of microextruded specimens were shown. To investigate the influence of the specimen size on hardness (i.e., deformation) distribution, three different die sets which have dimensions of Ø0.76/.57 mm, Ø1.5/1.0 mm and Ø2.0/1.33 mm before and after reduction respectively, were used. The microextruded pins were fabricated from CuZn30 α-brass which has a FCC structure. For the fine structure (32 μm), the deformation distribution was found to be independent of the specimen size. Thus to compare the deformation distribution to the hardness distribution through the diameter, the results of fine structure pins were used.

In Fig. 4.6, the measured hardness profiles of the microextruded pins for the two extrusion ratios are given. In order to plot the curves of specimens which have different sizes on the same graph, the radial distance was normalized by dividing the radial distance of the pins by the radius. For the extrusion ratio of 1.77, two pins which have

∅0.76/0.57 mm diameters before and after extrusion were measured. For the extrusion ratio of 2.25, pins which have ∅2.0/1.33 mm and ∅1.5/1.0 mm diameters before and after extrusion were measured. For each microextrusion case, two pins were measured and the hardness values were averaged. Each data point in Fig. 5 represents an average of approximately 20 hardness measurements for the extrusion ratio of 1.77 and approximately 40 hardness measurements for the extrusion ratio of 2.25. The error bars on the plots represent the range of measurement errors.

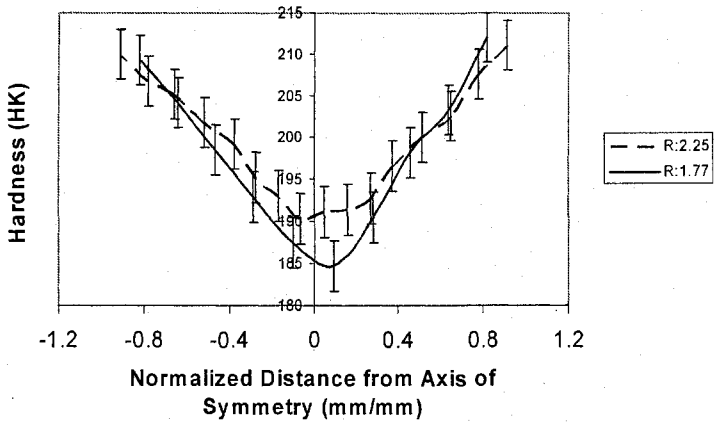

Figure 4.6 Measured average hardness values versus normalized radial distance for extrusion ratios of 2.25 and 1.177.

Consistent with the deformation distribution through the radial direction in extrusion as formulated in Eq. (4.13) and shown in Fig. 4.4, the pins have higher hardness (and higher strain) near the surface due to additional shear deformation and lower hardness (and lower strain) in the central region. Also consistent with Eq. (4.13) and Fig. 4.4, the pins which experience a lower extrusion ratio (1.77) have lower hardness than the pins which experience a higher extrusion ratio (2.25) at the central region. At the surface region, comparable hardness values exist. This occurs because at high strain values, the increase in the hardness for CuZn30 saturates (see Fig. 4.5). In addition to saturation of

hardness at high strain values, the pins which experience lower and higher extrusion ratios have comparable hardness values at the surface region (due to friction at the die workpiece interface).

Calculation of Density of GNDs During Microextrusion

The GNDs are stored due to the shear strain gradients at the shear discontinuity planes and due to the geometry of the reduction section. An approximation of the density of GNDs, stored due to the shear strain gradients at the shear discontinuity planes, A and B, can be calculated according to Eqs. (4.1), (4.7) and (4.8) as:

$$\rho_{GND_{SDP_A}} = \frac{\tan\alpha}{br_i} \tag{4.16}$$

$$\rho_{GND_{SDP_B}} = \frac{\tan\alpha}{br_f} \tag{4.17}$$

Thus, the total density of GNDs stored due to the shear strain gradients at the shear discontinuity planes, A and B is:

$$\rho_{GND_{SDP}} = \frac{\tan\alpha}{b}\left(\frac{1}{r_i} + \frac{1}{r_f}\right) \tag{4.18}$$

An approximation of the density of GNDs stored due to the strain gradients at the reduction section can be calculated as follows. For simplicity it is assumed that the shape change at the reduction section is accommodated by a number of dislocation loops, i.e., GNDs with burgers vectors perpendicular to the axis of symmetry, as shown schematically in Fig. 4.7. This is similar to the technique used by Nix and Gao who investigated strain gradient hardening during indentation [22]. If λ is the total length of the dislocation loops, then between r and r + dr:

$$d\lambda = 2\pi r \frac{dr}{b} \tag{4.19}$$

After integration, this provides:

$$\lambda = \int_{r_f}^{r_i} \frac{2\pi}{b} r dr = \frac{\pi}{b}(r_i^2 - r_f^2) \tag{4.20}$$

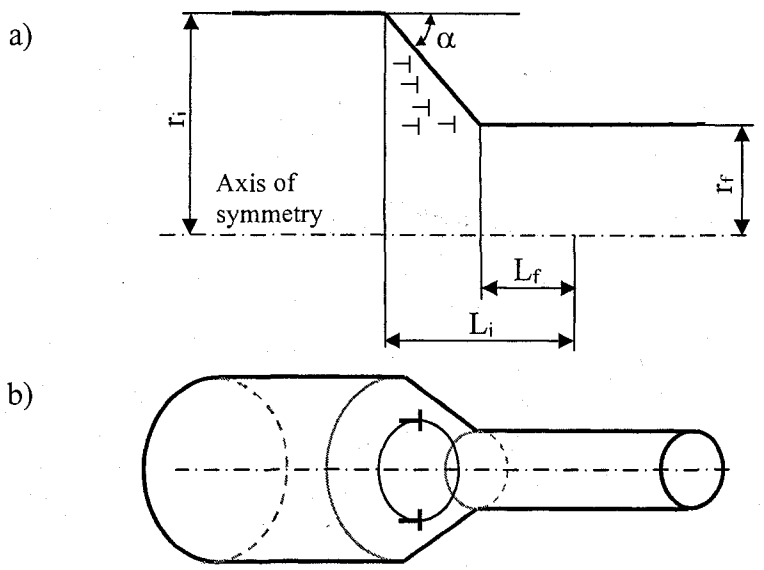

Figure 4.7 a) Geometrically Necessary Dislocations, GNDs, which are stored during deformation at the reduction section b) a GND loop at the reduction section.

The volume of the reduction section is:

$$V = \frac{\pi}{3\tan\alpha}(r_i^3 - r_f^3) \tag{4.21}$$

The density of GNDs that are stored at the reduction section can be calculated by dividing the GND length, λ, by the volume:

$$\rho_{GND_{RS}} = \frac{\lambda}{V} \tag{4.22}$$

$$\rho_{GND_{RS}} = \frac{\frac{\pi}{b}(r_i^2 - r_f^2)}{\frac{\pi}{3\tan\alpha}(r_i^3 - r_f^3)} \tag{4.23}$$

After simplification, the density of GNDs that are stored in the reduction section is:

$$\rho_{GND_{RS}} = \frac{3\tan\alpha}{b}\frac{(r_i + r_f)}{(r_i^2 + r_i r_f + r_f^2)} \tag{4.24}$$

Summing Eqs. (16), (17) and (24), the total density of GNDs stored during microextrusion is:

$$\rho_{GND_T} = \frac{\tan\alpha}{b}\left(\frac{1}{r_i} + \frac{3(r_i + r_f)}{(r_i^2 + r_i r_f + r_f^2)} + \frac{1}{r_f}\right) \tag{4.25}$$

Thus, the density of GND increases with a decrease in the initial and final radii of the specimen, r_i and r_f, and an increase in the die angle, α. Note that if α=0, the GND density would be zero.

Strain Gradient Hardening During Microextrusion

In Chapter 1, microextruded CuZn30 α-brass micropins, which have diameters on the order of a millimeter and submilimeter range, were investigated. Thus, the following calculations were performed to determine the SGH effect during axissymmetric forward microextrusion for CuZn30. Sevillano et al. [31] showed that the relation between the dislocation density and tensile strength of a cold rolled CuZn30 Brass is:

$$\sigma = 108 + 1.95Gb\rho^{1/2} \text{ (MPa)} \tag{4.26}$$

where G is the shear modulus. In this equation, the dislocation density, ρ, can be assumed to be the SSD density since no steep strain gradients exits in these macroscale specimens. But these can only be considered estimates for SSDs since the specimens were cold rolled. To include SGH, the formulation can be modified according to Eq. (4.2) as:

$$\sigma = 108 + 1.95Gb\,(\rho_{SSD}+\rho_{GND})^{1/2} \text{ (MPa)} \tag{4.27}$$

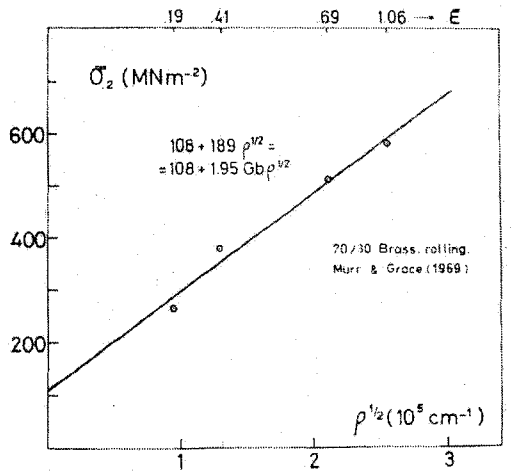

Figure 4.8 Correlation between yield strength of rolled CuZn30 and square root of dislocation density [31].

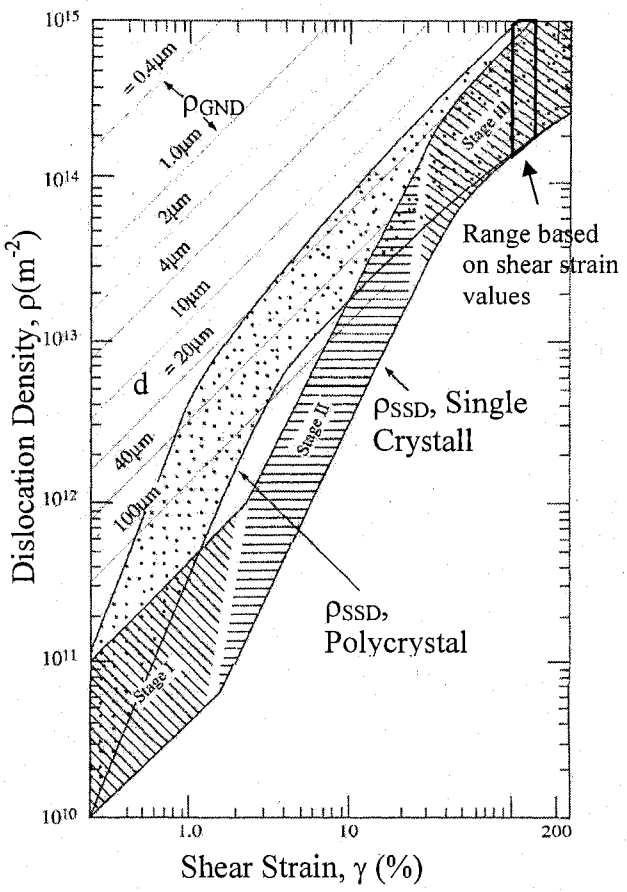

Figure 4.9 Variation of ρ_{SSD} from experimental data for single crystals (inferred from stress-strain curves for polycrystals) and ρ_{GND} (calculated) with respect to shear strain [21].

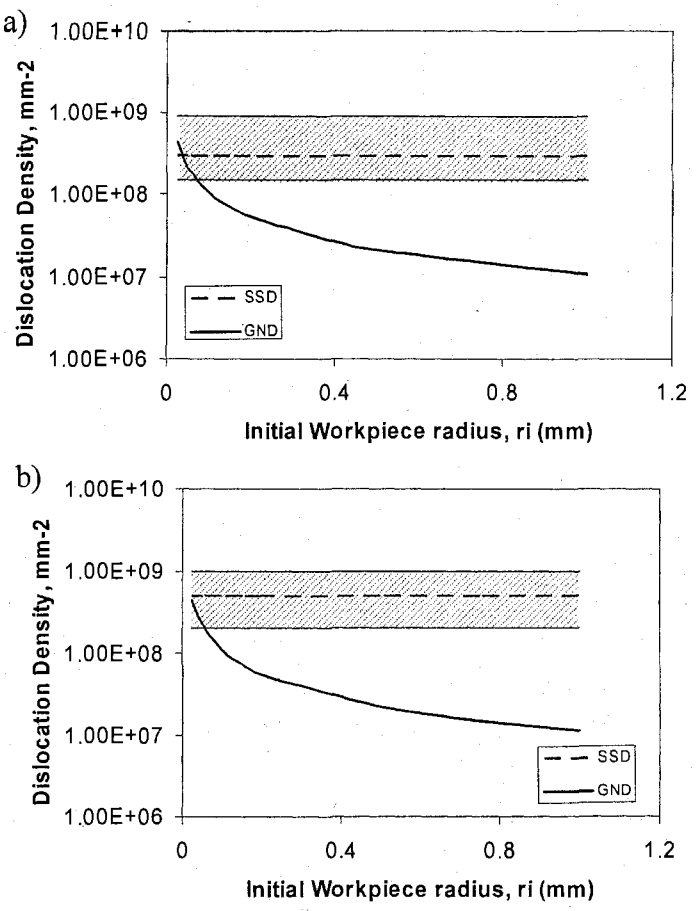

Figure 4.10 The densities of SSDs and GNDs versus initial radius of the workpieces (for a die angle of 30° and reduction ratios of a) R=1.77 (strain of 57 %) and b) R=2.25 (strain of 81%). Note that the SSD densities correspond to the deformation amount at the axis of symmetry. The range of SSDs densities of polycrystals, which are obtained from Fig. 4.9, are presented as a shaded band.

The calculations were performed for axisymmetric extrusion which have extrusion ratios of R=1.77 and R=2.25 that produce 57% and 81% strain respectively near the axis of symmetry in the workpiece based on Eq. (4.3). The corresponding shear strains according to Eq. (4.11) are 99% and 140%. In Fig. 4.8, the relationship between the strain amount and square root of dislocation density and the strength of rolled CuZn30 is given [31]. For this figure, the dislocation density was obtained using Transmission Electron Microscopy (TEM). The obtained SSD densities from Fig. 4.8 are consistent with the SSD densities calculated for polycrystals by Fleck et al. [21], see Fig.

4.9.

In Fig. 4.10, the densities of SSDs and GNDs are given with respect to the initial radius of the workpiece. The corresponding SSD densities were obtained from Fig. 4.8 for the deformation amounts near the axis of symmetry. The range of SSDs densities of polycrystals, which are obtained from Fig. 4.9, are presented as a shaded band. The GND densities were calculated using Eq. (4.25) for a die angle of α=30°(which is the die angle of the tooling used in our microextrusion experiments). Also, in Fig. 4.11, the percentage increase in the strength near the axis of symmetry due to SGH is shown with respect to the initial workpiece radius for the reduction ratios. These values were calculated using Eqs. (26) and (27).

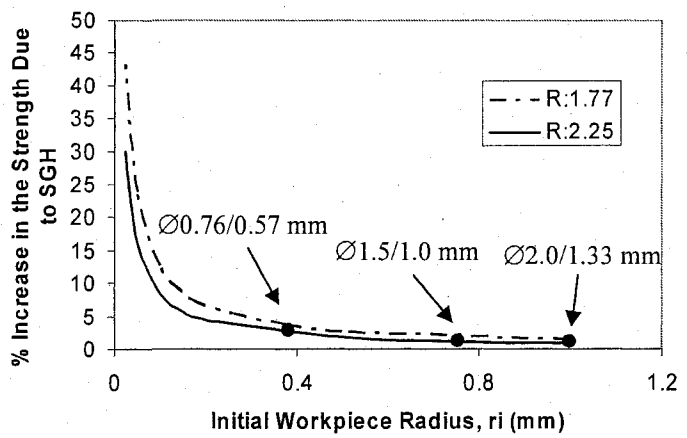

Figure 4.11 Percentage increase in the strength of the workpiece near the axis of symmetry due to SGH with respect to the specimen thickness for CuZn30 and α = 30°.

In Fig. 4.11 the percentage increase in the strength due to SGH for the microextruded specimens from Chapter I are indicated by black dots. A 3.6 %, 1.2% and 0.9% increase in the strength is calculated for the Ø0.76/0.57 mm, Ø1.5/1.0 mm and Ø2.0/1.33 mm pins respectively at the axis of symmetry due to SGH. In Table 4.1 the calculated strengths of pins with and without SGH (according to Eqs. (4.26) and (4.27))

and corresponding percentage increase in the strength due to SGH are given. Fig. 4.12 provides a flowchart for these calculations.

Table 4.1 The increase in strength and hardness at the axis of symmetry due to SGH for the pins from previous study

Initia /Final Pin diameters (mm)	*Exturision Ratio R*	*The Strain produced at the axis of symmetry (mm/mm)*	*Strength at the axis of symmetry without SGH (MPa)*	*Strength at the axis of symmetry with SGH (MPa)*	*Increase in the Strength due to SGH*	*Increase in Hardness due to SGH*
Ø0.76/0.57	1.77	0.575	461.6	478.1	3.6%	6.5 HK
Ø1.5/1.0	2.25	0.81	576.1	582.8	1.2%	2.3 HK
Ø2.0/1.33	2.25	0.81	576.1	581.2	0.9%	1.7 HK

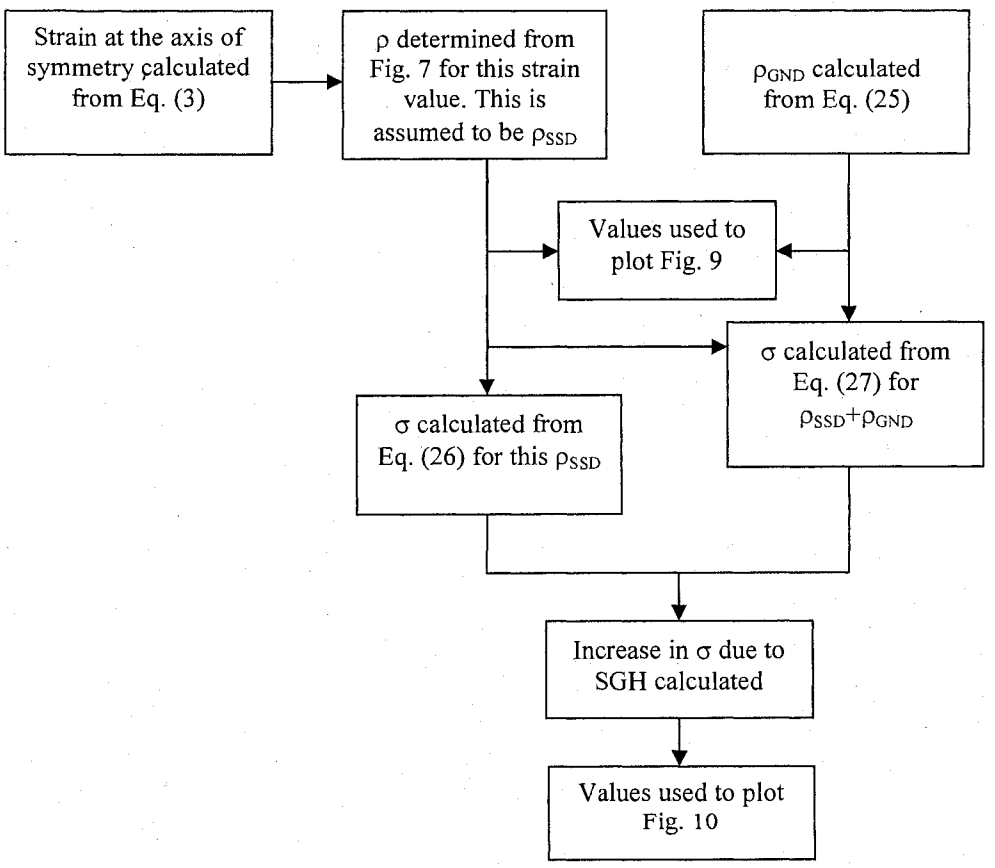

Figure 4.12 Flowchart of the strain gradient hardening calculations.

As shown in Figs. 4.10 and 4.11, as the workpiece radius decreases, the density of GNDs increases and the workpiece undergoes more SGH. This effect seems to increase significantly when the initial workpiece radius is less than approximately 200 μm. Also from Fig. 4.11, a decrease in the extrusion ratio will result in an increase in the SGH. This is because the ratio of the GND to SSD densities is relatively higher when the extrusion ratio is lower. In addition, the increase in the SGH hardening is higher at the axis of symmetry than at the outer regions. As is observed in Fig. 4.4, the strain (and thus the number of SSD obtained e.g. from Sevillano [31]) is a minimum at the axis of symmetry and increases near the surface of the sheet. Thus, the ratio of GND to SSD densities would decrease and the effect of the SGH would become less near the surface.

Also, as mentioned previously, the effect of friction is excluded from the calculation of the deformation distribution through the diameter. Due to friction, the strain amounts will increase and thus the strain gradients will be steeper at the surface region. However, provided that the workpiece diameter is large and number of grains through the cross section is large, the effect of friction will be limited at the surface region and the central region of the workpieces will be free from frictional effects.

The measured hardness values near the axis of symmetry is about 185 HK for the Ø0.76/0.57 mm pins which have R=1.77 and is about 190 HK for Ø1.5/1.0 mm and Ø2.0/1.33 mm pins which have R=2.25 (see Fig. 4.6). The percent increase values from Fig. 4.11 and Table 4.1 roughly indicate that about a 6.5 HK increase is possible for the Ø0.76/0.57 mm pins and about a 2 HK increase on average is possible for Ø1.5/1.0 mm and Ø2.0/1.33 mm pins. Thus, while the difference in the hardness for the R=1.77 and 2.25 cases is only approximately 5 HK, this difference would be larger (approximately

9.5 HK) if SGH did not occur (i.e., the 5HK value plus the 4.5 HK difference (6.5 HK minus 2 HK) from table 4.1). See Fig. 4.13 for a relationship between hardness and strength of CuZn30 showing a linear relationship despite the saturation for hardness versus strain in Fig. 4.5.

If consider the strain in the central region for the R=1.77 and R=2.25 cases (i.e., ε=0.57 and ε=0.81 respectively) and use these strain values in Fig.4.5, the approximate hardness change would be 9 VHN, see Fig 4.5. This is similar to the 9.5 HK difference for the case if SGH did not occur. Thus, the model appears to represent experimental data reasonably well. Note that Fig. 4.5 has units of Vickers Hardness while Fig. 4.6 has values of Knoop Hardness. Both the Knoop and Vickers are microhardness methods and they exhibit similar change in hardness values.

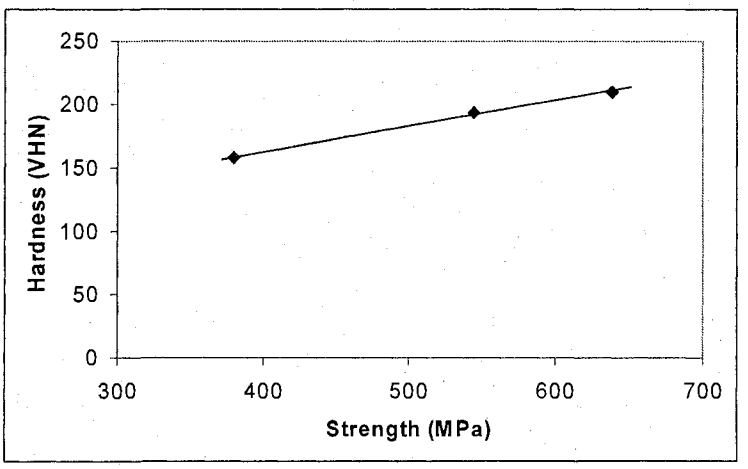

Figure 4.13 Correlation between the hardness of cold rolled CuZn30 and the yield strength at strains levels above ε=0.35 (data obtained from [14]).

Conclusion of This Chapter

In this chapter, a new formulation is presented to predict the strain distribution through the thickness of the workpiece during axissymmetric forward microextrusion. The formulation has a homogeneous strain and a shear strain component. The shear strain

is zero at the axis of symmetry and increases gradually, having its maximum value at the surface. By also using shear components of this formulation, a new model is established to estimate the GND density during microextrusion. It is found that the GND density increases with a decrease in the initial and final specimen thickness and an increase in the die angle. Also it is shown that, for the smallest size, Ø0.76/0.57 mm pins, a 3.6% increase in the strength at axis of symmetry is predicted, while a 1.2% and 0.9% increase in the strength is predicted for Ø1.5/1.0 mm and Ø2.0/1.33 mm pins respectively at the axis of symmetry due to strain gradient hardening. Thus, the predicted increases in the strength due to SGH are not significant for the pins that are used in Chapter 1. With respect to the assumptions in the analytical model, the increases would likely be less than 5-10% and still insignificant even if friction was included, the SSD density was higher, etc. Finally, the microhardness results from past research were compared with analytical model results and similar trends were observed.

CHAPTER 5

CONCLUSIONS

In this thesis, the deformation through the cross section for microextrusion and microbending were investigated to determine the affect of the grain size and specimen size. For both of these microforming processes, deformation gradients exit through the cross section. Microhardness evaluations were performed to characterize the deformation distribution through the diameter and thickness of microextruded and microbent specimens respectively. The results reveal that the deformation distribution through the cross sections of the specimens is affected by the grain size when specimen size is miniaturized.

For both processes, the deformation distribution through the cross sections of the fine grained specimens is not affected significantly by the specimen size (i.e. deformation distribution is independent from the specimen size) since the hardness profiles for the all specimen sizes are similar. However, as the specimen size is miniaturized, the deformation distribution of the coarse grained specimens deviates from the fine grained ones, and from the larger size specimens. In addition, as the specimen size decreases the coarse grained specimens have higher hardness increase values at the central region compared to fine grained specimens. This occurs due to the penetration of deformation from highly strained outer regions to the less strained inner regions (or expansion of the highly deformed regions).

In both forming processes, strain gradients are generated during deformation due to the deformation geometry. In microextrusion there is also a contribution of the friction, as well. As a result of miniaturization the strain gradients generated in the specimens during deformation become steeper. It seems that when the strain gradients imposed by the deformation geometry become steeper the deformation behavior of the coarse grains begins to deviate from the fine grain in a strain gradient field. Penetration of deformation occurs and as a result coarse grained specimens have higher deformation amounts (and thus higher hardness increase values) at the less strained central region compared to fine grain ones in microextrusion and microbending. For microbending, the specimens also experience a lower deformation at the highly strained surface region, and thus have lower hardness increase values at the surface compared to fine grained specimens. For microextrusion, because of the high friction generated between die workpiece interfaces, the coarse grained pins have comparable high hardness values at the surface region as well.

For microextrusion, the microstructure analyses, together with the X-Ray pole figure analyses show that inhomogeneous deformation patterns exist through the length of submillimeter size coarse grained pins. For microbending, the microhardness evaluations reveal that for the coarse grained specimens, inhomogeneous deformation patterns exist with miniaturization. Also, inhomogeneous deformation was observed for the coarse grained microtensile tested specimens that have only a few grains through the cross-section from the mirohardness and microstructure evaluations. Thus, in general it can be concluded that inhomogeneous deformation exists with miniaturization.

In addition, independent from the specimen size, the deformation distribution is

affected by the surface grains as well in microextrusion. Note that the surface grains experience extensive shear deformation due to friction and due to the deformation geometry.

Furthermore, a shape irregularity is observed in the microextrusion of the submilimeter size coarse grained pins. Curving occurs for approximately 80% of these coarse grained pins. The tendency of the submillimeter size coarse-grained pins to curve is related to the relatively large portion of the workpiece occupied by individual grains which promote more inhomogeneous deformation. This would imply that the individual size, location and orientation of the coarse grains would have a significant impact on the deformation characteristics of the workpiece. As a result of inhomogeneous (elastic and plastic) deformations, asymmetric residual stresses accumulate in the workpieces which causes subsequent extruded material to continue to flow in an asymmetric manner and thus curve. To avoid such shape irregularities, it is recommended that the number of the grains through the diameter of the workpiece should be more than 10.

Finally, a formulation is generated to estimate the strain distribution through the thickness during axis symmetric forward extrusion. By also using shear components of the formulation, a new model is established to estimate the GND density stored during microextrusion. It is found that the GND density increases with a decrease in the initial and final specimen radii and an increase in the die angle, α. Then, using a Taylor type equation as proposed by Ashby, the strain gradient hardening, SGH, that is experienced by the microextruded pins used in Chapter 1 is estimated. For the smallest size, Ø0.76/0.57 mm pins, a 3.6 % increase in the strength at the axis of symmetry is predicted, while a 1.2% and 0.9% increase in the strength is predicted for Ø1.5/1.0 mm

and Ø2.0/1.33 mm pins respectively at the axis of symmetry due to strain gradient hardening. Thus, the predicted increases in the strength due to SGH are not significant for the pins that are used in Chapter 1. Also, it is found that to avoid a significant amount of strain gradient hardening, the initial radius of the material should be roughly on the order of 200 μm or greater. The microhardness results from past research were compared with analytical model results and similar trends were observed.

CHAPTER 6

FUTURE WORK

Possible future works include;

1. Investigation of the behavior of a different metallic material such as aluminum in similar microforming operations. In this research, specimens made of CuZn30 were used and some deformation size effects were observed. In order to generalize these results (more confidently) similar experiments can be performed with a different material to check if similar deformation size effects exist. For example, Aluminum could be used which has a different stacking fault energy than CuZn30.
2. Design more comprehensive microbending experiments with smaller size specimens. In this research, the smallest size specimens used in the microbending experiments have a thickness of 0.25 mm. Further miniaturization in the specimen size could be useful. Also, microhardness evaluations are time consuming. A visual strain measurement technique can be incorporated into the bending experiments instead of performing hardness measurements after bending to further study deformation size effects.
3. Design and perform additional experiments to investigate the dependence of penetration of deformation behavior to the grain size such as, friction experiments with high loads. In this research, the deformation distribution through the cross sections of the microbent and microextruded specimen was investigated. During

both processes strain gradients exist during deformation and with miniaturization penetration of deformation (or expansion of deformed area) was observed. In order to investigate this behavior solely and in a more detailed way, additional experiments can be designed and performed.

4. Perform similar microhardness measurements or incorporation of visual strain measurement techniques on different microforming processes, such as microcompression tests, microforging or backwards can extrusion processes in order to assess deformation size effects in these processes.
5. Investigate strain gradient hardening through rolling experiments or micro plane strain extrusion experiments with foil sheet sizes. A small strain gradient amount is predicted for the microextruded specimens used in this research. The results show that to experience a significant amount of strain gradient hardening, the specimen thickness should be on the order of several hundred microns or less. In addition, designing and performing plane strain microextrusion or microrolling experiments can be easier than axis symmetric microextrusion.
6. Design and perform more comprehensive plane strain microextrusion experiments with different grains sizes, extrusion ratios and die angles. In this research, the effect of specimen size and grain size was investigated. The die angle and the extrusion ratio were kept constant. In order to construct an analytical model for microextrusion, the effect of these parameters (i.e., grain size, specimen size, extrusion ratio, die angle) on deformation can be investigated in a more detailed fashion.

LIST OF REFERENCES:

[1] Vollertsen, F., Hu, Z., Niehoff, H.,S., Theiler, C, "State of the art in micro forming and investigations in micro deep drawing", Journal of Materials Processing Technology, Vol. 151, No. 1-3, ., 2004, pp. 70-79.

[2] Geiger, M., Kleiner, M., Eckstein, R., Tiesler, N., and Engel, U.,"Microforming," CIRP Ann., 50(2), 2001, pp. 445-462.

[3] Engel, U., and Eckstein, R., "Microforming – from Basic Research to its Realization," J. Mater. Process. Technol., 125-126, 2002, pp. 35-44.

[4] Raulea, L.V., Goijaerts, A.M., Govaert, L.E., and Baaijens, F.P.T., "Size effects in the processing of thin metal sheets," J. Mater. Process. Technol., 115, 2001, pp. 44-48.-5

[5] Egerer, E., and Engel, U., 2004, "Process Characterization and Material Flow in Microforming at Elevated Temperatures", J. Man. Processes, 6, 1, pp.11-16. 2

[6] Kals, T.A., Eckstein, R., "Miniaturization in sheet metal working", Journal of Materials processing Technology, 103, 2000, pp. 95-101.

[7] Kocanda, A., Prejs, T., 2000, "The effect of miniaturization on the final geometry of the bent products", Metal Metal Forming 2000, Proc. Of the 8th International Conference on Metal Forming, Rotterdam, Balkema, pp.375-78.

[8] Justinger, H., Hirt, G., "Estimation of grain size and grain orientation influence in microforming processes by Taylor factor considerations", Journal of Materials Processing Technology, 2008, in press

[9] M. Geers, Technical University of Eindhoven, http://www.wtec.org/micromfg/report/03-Materials.pdf

[10] Cavaliere, P., Gabrielli, F., Fratini, L., "Bending of Very Thin Sheets: the Influence of Thickness on Material Characterisation and Elastic Springback", Proceedings of the 8th International Conference on Metal Forming, Krakow (Pl), 2000, pp. 405-410.

[11] Engel, U., Messner, A., Tiesler, N., "Cold Forging of Microparts-Effects of Miniaturization on Friction. Chenot, J.L. et al. (Eds.), Proceedings of the 1st ESAFORM Conf. on Materials Forming, Sophia Antipolis, France, 1998, pp: 77-80.

[12] Tiesler, N., Engel, U., Geiger, M., "Forming of Microparts-Effects of Miniaturization on Friction", Advanced Technology of Plasticity, Vol. II, Proceedings of the 6th ICTP, Sept.19-24, 1999, pp:889-894.

[13] Tiesler, N., Engel, U., "Microforming-Effects of Miniaturization", Metal Forming 2000, Proc. Of the 8th International Conference on Metal Forming, Rotterdam, Balkema, pp.355-360.

[14] Engel, U., "Tribology in Microforming", Wear, 260, 2006, pp:265-273.

[15] Krishnan, N., Cao, J. and Dohda K. "Study of the Size Effect on Friction Conditions in Micro-extrusion: Part 1 - Micro-Extrusion Experiments and Analysis", ASME J. Manufacturing Science and Engineering, Vol. 129, August, 2007, pp: 669-676.

[16] Richard M. Onyancha, Brad L. Kinsey, Neil Krishnan, and Jian Cao, "Development of an Accurate Process Model for Microscale Forward Extrusion, Transactions of the North American Manufacturing Research Institute of SME, Vol. 35, pp., 2007, 121-128.

[17] Richard M. Onyancha, Brad L. Kinsey, and Ulf Engel, "Analytical Process Models for Microbending: An Investigation of Process Model Assumptions", in preparation for the Journal of Manufacturing Science and Engineering, 2008

[18] Richard M. Onyancha and Brad L. Kinsey, "Experimental Investigation of Microbending Process", Transactions of the North American Manufacturing Research Institute of SME, Vol. 36, 2008, pp. 65-71.

[19] Richard M. Onyancha* and Brad L. Kinsey, "Investigation of Size Effects on Process Models for Plane Strain Microbending", International Manufacturing Science and Engineering Conference, Ypsilanti, Michigan, Oct. 8-11, 2006.

[20] Engel, U., Egerer, E., "Basic Research on Cold and Warm Forging of Microparts", Key Engieering Materials, Vols. 233-236, 2003, pp. 449-456.

[21] Fleck, N.A., Muller, G. M., Ashby, M.F. and Hutchinson, W., "Strain Gradient Plasticity: Theory and Experiment", Acta Metall. Mater., Vol. 42, No:2, 1994, pp.475-487.

[22] Nix, W.D., Gao,H., "Indentation Size effects in Crystalline Materials: A Law For Strain Gradient Plasticity", J. Mech. Phys. Solids., 46, 3, 1998, pp. 411-425.

[23] Stolken, J.S., Evans, A.G., "A Microbend Test Method for Measuring the Plasticity Length Scale", Acta Mater., Vol.14, No. 14, 1998, pp.5109-5115.

Proceedings of IMECE 2005, Nov. 5-11, Orlando, FL

[37] Cao, J., Krishnan, N., Wang, Z., Lu, H., Liu, W.K., and Swanson, A., 2004, "Microforming –Experimental investigation of the extrusion process for micropins and its numerical simulation using RKEM," ASME J. Manuf. Sci. Engng., 126, pp. 642-652.

[38] Cullity, B.D. and Stock, S.R., 2001, "Elements of X-Ray Diffraction", Prentice Hall, Upper Saddle River, NJ, pp. 402-409.

[39] Murr, L.E. and Grace, F.I., Trans. AIME, 1969, 245, pp. 2225

[40] Mori, L., Krishnan, N., Cao, J. and Espinosa, H.D., 2006, "Study of the Size Effects and Friction Conditions in Micro-extrusion: Part II - Size effect in dynamic friction for brass-steel pairs", submitted to ASMEJ. Manufacturing Science and Technology.

[41] Barret, C., S, and Massalski, T., B., *Structure of Metals*, McGraw-Hill Book Company, New York, 1966, pp. 544

[42] Wenk, H., R., 1985, Preferred Orientations in Deformaed Metals and Rocks: An Introduction to Modern Texture Analysis, Academic Press, Inc., New York, pp. 56.

[43] Kocks, U.F., Tome, C.N., and Wenk, H.-R., 2000, *Texture and Anisotropy*, Cambridge University Press, New York, pp. 227.

[44] Schoenfeld, S., E., and Asaro, R., J., 1996, "Through thickness texture gradients in rolled polycrystalline Alloys", *Int. J. Mech. Sci.*, 38, 6, pp.661-683

[45] Asbeck, H. and Mecking, H., 1978, "Influence of friction and geometry of deformation on texture inhomogeneities during rolling of Cu single crystals as an example", *Mater. Sci. Eng.*, 34, pp.111-119.

[46] Truszkowski, W., Krol, J., and Major, B., "Inhomogeneity of Rolling Texture in fcc Metals", Metallurgical Transactions A, 11A, 1980, pp.749-758.

[47] Choi, C., Kwon, J., Oh, K., H., and Lee, D., N., "Analysis of Deformation Texture Inhomogeneity abd Stability Condition of Shear Components in f.c.c. Metals", Acta Mater, 45, 12, 1997, pp.5119-5128.

[48] Lee, D., N., Chung, Y., H., and Shin, M., C., "Preferred Orientation in Extruded Aluminum Alloy Rod", Scripta Metallurgica, 17, 1983, pp.339-342.

[49] Hertzberg, R., W., 1989, *Deformation and Fracture Mechanics of Engineering Materials*, John Wiley & Sons, New York, pp. 86.

[50] Diehl, A., Engel, U., Geiger, M., "Investigation of the Spring-back behaviour in metal foil forming", Proceedings of the 24th IDDRG-Conference, Besancon, Frankreich, 2005.

[51] Fulop,T., Brekelmans, W.A.M., Geers, M.G.D., "Size effects from grain statistics in ultra-thin metal sheets", Journal of Materials Processing Technology, 174, 2006, pp. 233-238.

[52] Eckstein, R., Engel, U., "Behavior of the grain structure in micro sheet metal working", Metal Forming 2000, Pietrzyk et al. (eds), 2000 Balkerna, Rotterdam, pp. 453-459.

[53] Eckstein, R., Geiger, M., Engel, U., "Specific Characteristic of Micro Sheet Metal Working" Proceedings of SheMet, Sept.27-28, 1999, pp. 529-536.

[54] ASM Hanbook, "Metalworking: Sheet Forming", Vol. 14B, 2006, pp. 295.

[55] Gau, J. T., Principe, C., Yu, M., "Springback behavior of brass in micro sheet forming", Journal of Materials Processing Technology, 191, 2007, pp. 7-10

[56] ASTM Standards E 112-96, Section 3, "Metals Test Methods and Analytical Procedures" Vol. 03.01, 2008, pp. 290-315.

[57] Kalpakjian S. and Schmid S.R., Manufacturing Engineering and Technology, Pearson Prentice Hall, New Jersey, 2006, pp.445.

[58] H. Mughrabi, "On the Current Understanding of Strain Gradient Plasticity", Mat. Sci. and Eng. A, Vol. 387-389, 2004, pp.209-213

[59] Parasız, S.A., Kinsey, B. L., "Analytical Model to Predict Geometrically Necessary Dislocation Density During Plane Strain Microextrusion" Proceedings of ICOMM 2008, Sept. 9-11, Pittsburgh, PA, USA.

[60] Talbert, S. H., Avitzur, B., "elementary Mechanics of Plastic Flow in Metal Forming", John Wiley and Sons: New York, 2001, pp. 357.

APPENDICES

APPENDIX A

X-Ray Pole Figure Analyses:

The determination of the preferred orientation of the grains in a polycrystalline material is referred to as texture analysis. Pole figures are one common way to obtain and present the preferred orientation of materials. A pole figure provides diffraction intensity of a given reflection (i.e., of a given plane) at a large number of different angular orientations of the specimen. A contour map of the intensity is then plotted as a function of angular orientation of the specimen. Pole figures give the probability of finding a given crystal plane-normal with respect to specimen orientation. Thus, in order to determine reflected diffraction poles with respect to the specimen coordinate system, the specimen should be placed in the X-Ray machine so that its coordinate system with respect to machine is known.

In the pole figure analyses performed in this research, the microextruded specimens were placed on the X-Ray machine such that the extrusion direction coincidences with zero Phi angle value. In Fig. A1, the Phi angle values are indicated around the circle in the pole figure.

In order to determine the preferred orientation that is developed after extrusion (that is parallel to extrusion direction), the angle between the diffracted poles and the extrusion direction is measured from different pole figures which are obtained from the same specimen (e.g. (111) and (100) pole figures for FCC).

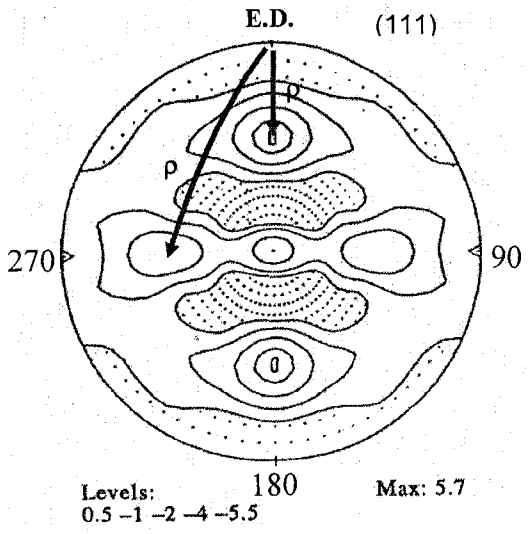

Figure A1 Determination of preferred orientation from a pole figure

APPENDIX B

MatLab code for theMicrobending hardness contour plots:

An example for the 0.25 mm thick specimen case, Fig. 2.4:

```
aR=load('np_250_500_03_R.txt');

aL=load('np_250_500_03_L.txt');

bR=load('np_250_500_05_R.txt');

bL=load('np_250_500_05_L.txt');

cR=load('np_250_650_01_R.txt');

cL=load('np_250_650_01_L.txt');

dR=load('np_250_650_06_R.txt');

dL=load('np_250_650_06_L.txt');

eR=load('np_250_800_01_R.txt');

eL=load('np_250_800_01_L.txt');

fR=load('np_250_800_04_R.txt');

fL=load('np_250_800_04_L.txt');
```

```
% np_250_500_03
np_250_500_03=(aR+aL)/2;
for i=1:length(np_250_500_03)
   ave_250_500_03(i)=mean(np_250_500_03(i,:));
end
x=-75:25:75;
level=[0 84 94 104 114];
figure(1);
contourf(np_250_500_03, level);
title('Contour Plot of np 0.25 mm 20 micron #03');
%
% np_250_500_05
np_250_500_05=(bR+bL)/2;
for i=1:length(np_250_500_05)
   ave_250_500_05(i)=mean(np_250_500_05(i,:));
end
xc=[0:230:1150];
yc=[-75:25:75];
level=[0 82.5 92.5 102.5 112.5];
figure(2);
contourf(xc,yc,np_250_500_05, level);
```

```
title('Contour Plot of np 0.25 mm 20 micron #05');
%
% Average plots of np_250_500 specimens
np_250_500_ave=(np_250_500_03+np_250_500_05)/2;
for i=1:length(np_250_500_ave)
   ave_250_500(i)=mean(np_250_500_ave(i,:));
end
for i=1:length(np_250_500_ave)
   ave_2_250_500(i)=mean(np_250_500_ave(i,1:2));
end
for i=1:length(np_250_500_ave)
   ave_3_250_500(i)=mean(np_250_500_ave(i,1:3));
end
for i=1:length(np_250_500_ave)
   ave_4_250_500(i)=mean(np_250_500_ave(i,1:4));
end
for i=1:length(np_250_500_ave)
   ave_5_250_500(i)=mean(np_250_500_ave(i,1:5));
end

level=[20 83 93 103 113];
```

```
figure(6);
contourf(xc,yc,np_250_500_ave, level);
title('Contour Plot of 2 np 0.25 mm 20 micron specimens #03 & #05');
%%%
```

```
figure(8);
contourf(np_250_650_06, level);
title('Contour Plot of np 0.25 mm 129 micron #06');
% Average plots of np_250_650 specimens
np_250_650_ave=(np_250_650_01+np_250_650_06)/2;
for i=1:length(np_250_650_ave)
   ave_250_650(i)=mean(np_250_650_ave(i,:));
end
for i=1:length(np_250_650_ave)
   ave_2_250_650(i)=mean(np_250_650_ave(i,1:2));
end
for i=1:length(np_250_650_ave)
   ave_3_250_650(i)=mean(np_250_650_ave(i,1:3));
end
for i=1:length(np_250_650_ave)
   ave_4_250_650(i)=mean(np_250_650_ave(i,1:4));
end
for i=1:length(np_250_650_ave)
   ave_5_250_650(i)=mean(np_250_650_ave(i,1:5));
end
level=[0 76.5 86.5 96.5 106.5];
```

```
figure(12);
contourf(xc,yc,np_250_650_ave, level);
title('Average Contour Plot of 2 np 0.25 mm 129 micron specimens #01 & #06');
%%%
```

```
figure(15);
contourf(np_250_800_04, level);
title('Contour Plot of np # 04 specimen, size:0.25 mm, Grain Size: 192 micron');
np_250_800_ave=(np_250_800_01+np_250_800_04)/2;
for i=1:length(np_250_800_ave)
   ave_250_800(i)=mean(np_250_800_ave(i,:));
end
for i=1:length(np_250_800_ave)
   ave_2_250_800(i)=mean(np_250_800_ave(i,1:2));
end
for i=1:length(np_250_800_ave)
   ave_3_250_800(i)=mean(np_250_800_ave(i,1:3));
end
for i=1:length(np_250_800_ave)
   ave_4_250_800(i)=mean(np_250_800_ave(i,1:4));
end
for i=1:length(np_250_800_ave)
   ave_5_250_800(i)=mean(np_250_800_ave(i,1:5));
end
level=[15 71.5 81.5 91.5];
figure(19);
```

```
contourf(xc,yc,np_250_800_ave, level);

title('Average Contour Plot of 2 NP specimens, size:0.25 mm, Grain Size: 192 micron');

%%%
```

```
  ave_500_550_02(i)=mean(np_500_550_02(i,:));
end
x=-203.2:50.8:203.2;
np_500_550_05=(bR+bL)/2-81;
for i=1:9
  ave_500_550_05(i)=mean(np_500_550_05(i,:));
end
% Average plots of np_500_550 specimens
np_500_550_ave=(np_500_550_02+np_500_550_05)/2;
for i=1:9
  ave_500_550(i)=mean(np_500_550_ave(i,:));
end
for i=1:9
  ave_3_500_550(i)=mean(np_500_550_ave(i,1:3));
end
for i=1:9
  ave_5_500_550(i)=mean(np_500_550_ave(i,1:5));
end
for i=1:9
  ave_6_500_550(i)=mean(np_500_550_ave(i,1:6));
end
```

```
for i=1:9
   ave_9_500_550(i)=mean(np_500_550_ave(i,1:9));
end
%%%
```

```
for i=1:9
  ave_3_500_700(i)=mean(np_500_700_ave(i,1:3));
end
for i=1:9
  ave_5_500_700(i)=mean(np_500_700_ave(i,1:5));
end
for i=1:9
  ave_6_500_700(i)=mean(np_500_700_ave(i,1:6));
end
for i=1:9
  ave_9_500_700(i)=mean(np_500_700_ave(i,1:9));
end
%%%
```

```
for i=1:9
   ave_500_800_05(i)=mean(np_500_800_05(i,:));
end


np_500_800_ave=(np_500_800_01+np_500_800_05)/2;
for i=1:9
   ave_500_800(i)=mean(np_500_800_ave(i,:));
end
for i=1:9
   ave_3_500_800(i)=mean(np_500_800_ave(i,5:7));
end
for i=1:9
   ave_5_500_800(i)=mean(np_500_800_ave(i,4:8));
end
for i=1:9
   ave_6_500_800(i)=mean(np_500_800_ave(i,3:8));
end
for i=1:9
   ave_9_500_800(i)=mean(np_500_800_ave(i,1:9));
end
%%%
```

```
figure(1)
plot(x,ave_5_500_550,'w:');
hold on;
plot(x,ave_5_500_550,'k:');
plot(x,ave_5_500_700,'k-.');
plot(x,ave_5_500_800,'k-');
legend('Grain Size ','22.5 microns ', '205 microns', '285 microns')
title('highly strained 5 lines i.e. 0.5 0.8 mm length on the half arm ');
xlabel('location through the thickness (microns)')
ylabel('microhardness increase(HK)')
error=[3.2 2.9 2.6 2.3 2 2.3 2.6 2.9 3.2];
errorbar(x,ave_5_500_550,error,'.');
errorbar(x,ave_5_500_700,error,'.');
errorbar(x,ave_5_500_800,error,'.');
```

MatLab Code for the Microbending average hardness increase curves for same grain size, Figure 2.9:

```
aR=load('np_250_500_03_R.txt');
aL=load('np_250_500_03_L.txt');
bR=load('np_250_500_05_R.txt');
bL=load('np_250_500_05_L.txt');
cR=load('np_250_650_01_R.txt');
```

```
cL=load('np_250_650_01_L.txt');
dR=load('np_250_650_06_R.txt');
dL=load('np_250_650_06_L.txt');
eR=load('np_250_800_01_R.txt');
eL=load('np_250_800_01_L.txt');
fR=load('np_250_800_04_R.txt');
fL=load('np_250_800_04_L.txt');
%%%
```

```
a3R=load('np_1500_515_02_R.txt');
a3L=load('np_1500_515_02_L.txt');
b3R=load('np_1500_515_01_R.txt');
b3L=load('np_1500_515_01_L.txt');
c3R=load('np_1500_715_02_R.txt');
c3L=load('np_1500_715_02_L.txt');
d3R=load('np_1500_715_05_R.txt');
d3L=load('np_1500_715_05_L.txt');
e3R=load('np_1500_800_04_R.txt');
e3L=load('np_1500_800_04_L.txt');
f3R=load('np_1500_800_06_R.txt');
f3L=load('np_1500_800_06_L.txt');
g3R=load('np_1500_665_04_R.txt');
g3L=load('np_1500_665_04_L.txt');
h3R=load('np_1500_665_05_R.txt');
h3L=load('np_1500_665_05_L.txt');
%%%
```

```
end
% np_250_500_05
%
np_250_500_05=(bR+bL)/2-84;
for i=1:length(np_250_500_05)
   ave_250_500_05(i)=mean(np_250_500_05(i,:));
end
%
% np_250_500 specimens
np_250_500_ave=(np_250_500_03+np_250_500_05)/2;
for i=1:length(np_250_500_ave)
   ave_250_500(i)=mean(np_250_500_ave(i,:));
end
for i=1:length(np_250_500_ave)
   ave_3_250_500(i)=mean(np_250_500_ave(i,1:3));
end
for i=1:length(np_250_500_ave)
   ave_4_250_500(i)=mean(np_250_500_ave(i,1:4));
end
%%%
```

```
np_250_650_01=(cR+cL)/2-78;

for i=1:length(np_250_650_01)

   ave_250_650_01(i)=mean(np_250_650_01(i,:));

end

%

% np_250_650_06

%

np_250_650_06=(dR+dL)/2-76;

for i=1:length(np_250_650_06)

   ave_250_650_06(i)=mean(np_250_650_06(i,:));

end

level=[0 80 90 100];

%

% Average plots of np_250_650 specimens

%

np_250_650_ave=(np_250_650_01+np_250_650_06)/2;

for i=1:length(np_250_650_ave)

   ave_250_650(i)=mean(np_250_650_ave(i,:));

end


for i=1:length(np_250_650_ave)
```

```
   ave_3_250_650(i)=mean(np_250_650_ave(i,1:3));
end
for i=1:length(np_250_650_ave)
   ave_4_250_650(i)=mean(np_250_650_ave(i,1:4));
end
%%%
```

```
np_250_800_ave=(np_250_800_01+np_250_800_04)/2;


for i=1:length(np_250_800_ave)
   ave_250_800(i)=mean(np_250_800_ave(i,:));
end
for i=1:length(np_250_800_ave)
   ave_3_250_800(i)=mean(np_250_800_ave(i,1:3));
end
for i=1:length(np_250_800_ave)
   ave_4_250_800(i)=mean(np_250_800_ave(i,1:4));
end
%%%
```

```
%
np_500_550_05=(b2R+b2L)/2-81;
for i=1:9
   ave_500_550_05(i)=mean(np_500_550_05(i,:));
end
% Average plots of np_500_550 specimens
%
np_500_550_ave=(np_500_550_02+np_500_550_05)/2;
for i=1:9
   ave_500_550(i)=mean(np_500_550_ave(i,:));
end
for i=1:9
   ave_5_500_550(i)=mean(np_500_550_ave(i,1:5));
end
%%%
```

```
%
% np_500_700_06
%
np_500_700_06=(d2R+d2L)/2-78.5;
for i=1:9
   ave_500_700_06(i)=mean(np_500_700_06(i,:));
end
% Average plots of np_500_700 specimens
%
np_500_700_ave=(np_500_700_01+np_500_700_06)/2;
for i=1:9
   ave_500_700(i)=mean(np_500_700_ave(i,:));
end
for i=1:9
  ave_5_500_700(i)=mean(np_500_700_ave(i,1:5));
end
%%%
```

```
   ave_500_800_01(i)=mean(np_500_800_01(i,:));
end
% np_500_800_05
np_500_800_05=(f2R+f2L)/2-79;
for i=1:9
   ave_500_800_05(i)=mean(np_500_800_05(i,:));
end
%
% Average plots of np_500_800 specimens
np_500_800_ave=(np_500_800_01+np_500_800_05)/2;
for i=1:9
   ave_500_800(i)=mean(np_500_800_ave(i,:));
end
for i=1:9
   ave_5_500_800(i)=mean(np_500_800_ave(i,4:8));
end
%%%
```

```
   ave_1500_515_02(i)=mean(np_1500_515_02(i,:));
end

% np_1500_515_01
%
np_1500_515_01=(b3R+b3L)/2-97;
for i=1:20
   ave_1500_515_01(i)=mean(np_1500_515_01(i,:));
end
% Average plots of np_500_550 specimens
%
np_1500_515_ave=(np_1500_515_02+np_1500_515_01)/2;
for i=1:20
   ave_1500_515(i)=mean(np_1500_515_ave(i,:));
end

for i=1:20
   ave_4_1500_515(i)=mean(np_1500_515_ave(i,1:4));
end

for i=1:20
```

```
   ave_5_1500_515(i)=mean(np_1500_515_ave(i,1:5));
end

%%%
```

```
np_1500_665_ave=(np_1500_665_04+np_1500_665_05)/2;
for i=1:20
   ave_1500_665(i)=mean(np_1500_665_ave(i,:));
end
for i=1:20
  ave_4_1500_665(i)=mean(np_1500_665_ave(i,1:4));
end
for i=1:20
  ave_5_1500_665(i)=mean(np_1500_665_ave(i,1:5));
end
%%%
```

```
end
% Average plots of np_1500_715 specimens
np_1500_715_ave=(np_1500_715_02+np_1500_715_05)/2;
for i=1:20
   ave_1500_715(i)=mean(np_1500_715_ave(i,:));
end
for i=1:20
  ave_4_1500_715(i)=mean(np_1500_715_ave(i,1:4));
end
for i=1:20
  ave_5_1500_715(i)=mean(np_1500_715_ave(i,1:5));
end
%%%
```

```
  ave_1500_800_06(i)=mean(np_1500_800_06(i,:));
end
%
% Average plots of np_1500_800 specimens
np_1500_800_ave=(np_1500_800_04+np_1500_800_06)/2;
for i=1:20
  ave_1500_800(i)=mean(np_1500_800_ave(i,:));
end
for i=1:20
  ave_4_1500_800(i)=mean(np_1500_800_ave(i,1:4));
end
for i=1:20
  ave_5_1500_800(i)=mean(np_1500_800_ave(i,1:5));
end
%%%
```

```
plot(x3,ave_5_1500_515,'k:');
plot(x2,ave_5_500_550,'k-.');
plot(x1,ave_3_250_500,'k-');
legend('Sheet thickness ','1.625 mm ', '0.5 mm ', '0.25 mm ')
title('highly strained regions,  20 micron ');
xlabel('normalized location through the thickness (mm/mm)')
ylabel('microhardness increase(HK)')
error_ave_4_1500_515=[3.8 0 3.4 0 3 0 2.6 0 0 2 0 2.2 0 2.6 0 3 0 3.4 0 3.8];
error_ave_5_500_550=[3.2 2.9 2.6 2.3 2 2.3 2.6 2.9 3.2];
error_ave_3_250_500=[2.9 2.6 2.3 2 2.3 2.6 2.9];
errorbar(x3,ave_4_1500_515,error_ave_4_1500_515,'.');
errorbar(x2,ave_5_500_550,error_ave_5_500_550,'.');
errorbar(x1,ave_3_250_500,error_ave_3_250_500,'.');
figure(3);
plot(x3,ave_5_1500_665,'w:');
hold on;
plot(x3,ave_5_1500_665,'k:');
plot(x2,ave_5_500_700,'k-.');
plot(x1,ave_3_250_800,'k-');
title('highly strained region, 200 micron ');
legend('Sheet thickness ','1.625 mm ', '0.5 mm ', '0.25 mm ')
```

```
xlabel('normalized location through the thickness (mm/mm)')
ylabel('microhardness increase (HK)')
error_ave_4_1500_515=[3.8 0 3.4 0 3 0 2.6 0 0 2 0 2.2 0 2.6 0 3 0 3.4 0 3.8];
error_ave_5_500_550=[3.2 2.9 2.6 2.3 2 2.3 2.6 2.9 3.2];
error_ave_3_250_500=[2.9 2.6 2.3 2 2.3 2.6 2.9];
errorbar(x3,ave_4_1500_665,error_ave_4_1500_515,'.');
errorbar(x2,ave_5_500_700,error_ave_5_500_550,'.');
errorbar(x1,ave_3_250_800,error_ave_3_250_500,'.');
figure(5);
plot(x3,ave_5_1500_715,'w:');
hold on;
plot(x3,ave_5_1500_715,'k:');
plot(x2,ave_5_500_800,'k-.');
title('highly strained region, 300 micron ');
legend('Sheet thickness ','1.625 mm ', '0.5 mm ')
xlabel('normalized location through the thickness (mm/mm)')
ylabel('microhardness increase (HK)')
error_ave_4_1500_515=[3.8 0 3.4 0 3 0 2.6 0 2.2 0 0 2.2 0 2.6 0 3 0 3.4 0 3.8];
error_ave_5_500_550=[3.2 2.9 2.6 2.3 2 2.3 2.6 2.9 3.2];
errorbar(x3,ave_4_1500_715,error_ave_4_1500_515,'.');
errorbar(x2,ave_5_500_800,error_ave_5_500_550,'.');
```

MatLab Code for the Normalized peak bending force versus specimen size curves for 20 μm, 190 μm and 280 μm grained sheets, Figure 2.11:

```
a=load('f_20_190_280.txt');
figure(1);
plot(a(:,1),a(:,2),'-w');
hold on
plot(a(:,1),a(:,2),':k')
plot(a(:,1),a(:,3),'k-.');
plot(a(2:3,1),a(2:3,4),'-k');
legend('Grain Size ','20 micron ', '190 micron ', '280 micron ')
xlabel('Specimen Thickness (mm)')
ylabel('Normalized Force (N/mm2)')
error_20=[11.6 17.6 12];
error_190=[8 17.45 11.7];
error_280=[17.5 8];
errorbar(a(:,1),a(:,2),error_20,'.');
errorbar(a(:,1),a(:,3),error_190,'.');
errorbar(a(2:3,1),a(2:3,4),error_280,'.');
axis([0 1.8 100 400])
```